

**Timing, internal flow characteristics, and emplacement mechanisms of the intrusive sheet network on the southern margin of Mount Hillers, Henry Mountains, southern Utah.**

by

Erik Thornton

April, 2015

Director of Thesis: (Eric Horsman)

Major Department: (Geological Sciences)

The exceptional 3-d exposures of the mid-Tertiary intrusive sheet network on the southern margin of Mount Hillers, Henry Mountains, southern Utah, have undergone no syn- or post-emplacement deformation. The sills and dikes, which formed above the underlying Mount Hillers laccolith, therefore provide an ideal opportunity to study purely magmatic processes in a shallow crustal intrusive sheet network. For this study, field work and laboratory analysis were employed to constrain the timing, emplacement mechanisms, and internal flow characteristics of these sills and dikes. Detailed geologic mapping of cross-cutting relationships, in addition to qualitative textural analysis in the field, indicate that younger, relatively fine-grained dikes cross-cut older, relatively coarse-grained sills. Crystal size distribution, thin section petrography, and major and trace element geochemistry all suggest two distinct batches of magma (one coarse- and one fine-grained) were involved in the construction of the sill/dike complex. Field fabrics and anisotropy of magnetic susceptibility fabrics suggest complex internal flow of the intrusive sheets throughout the growth of the central intrusive igneous body. Field observations indicate that intruding magma exploited radial fractures and bedding planes in the sedimentary host rock. In addition, rigidity contrasts in the host rock were likely an important control on the stratigraphic level of sill emplacement and on intrusive sheet thickness. The proposed construction model for the intrusive sheet network consists of an initial phase of dike-fed sill

emplacement in subhorizontal strata. During subsequent growth of the underlying main laccolithic body, which included uplift and rotation of the overburden, continued sill emplacement was followed by radial dike intrusion. This work provides insight into the growth and evolution of shallow crustal magmatic systems, such as those that underlie active volcanoes.



**TIMING, INTERNAL FLOW CHARACTERISTICS, AND EMPLACEMENT  
MECHANISMS OF THE INTRUSIVE SHEET NETWORK ON THE SOUTHERN  
MARGIN OF MOUNT HILLERS, HENRY MOUNTAINS, SOUTHERN UTAH**

A Thesis

Presented To the Faculty of the Department of Geological Sciences

East Carolina University

In Partial Fulfillment of the Requirements for the Degree

Master of Science in Geological Sciences

by

Erik Thornton

© Erik Thornton, 2015

**TIMING, INTERNAL FLOW CHARACTERISTICS, AND EMPLACEMENT  
MECHANISMS OF THE INTRUSIVE SHEET NETWORK ON THE SOUTHERN  
MARGIN OF MOUNT HILLERS, HENRY MOUNTAINS, SOUTHERN UTAH**

by

Erik Thornton

APPROVED BY:

DIRECTOR OF  
THESIS: \_\_\_\_\_

Eric Horsman, PhD

COMMITTEE MEMBER: \_\_\_\_\_

Richard Mauger, PhD

COMMITTEE MEMBER: \_\_\_\_\_

Adriana Heimann, PhD

COMMITTEE MEMBER: \_\_\_\_\_

Sven Morgan, PhD

CHAIR OF THE DEPARTMENT  
OF GEOLOGICAL SCIENCES: \_\_\_\_\_

Stephen Culver, PhD

DEAN OF THE  
GRADUATE SCHOOL: \_\_\_\_\_

Paul J. Gemperline, PhD

## **Acknowledgements**

I would like to thank my thesis advisor, Dr. Eric Horsman, for his help in the field and throughout the data analysis and writing process. His patience and knowledge helped in more ways than can be expressed here. I would also like to thank my committee members, Dr. Richard Mauger, Dr. Adriana Heimann, and Dr. Sven Morgan, for their review of my thesis and the other help they have provided throughout the completion of this research.

I would like to thank Mitch Ward, Nick DeSimone and Robert Broda for their help in the field. Our legendary adventures in Utah will not soon be forgotten.

I would like to thank the faculty of the Department of Geological Sciences at East Carolina University for their help and support throughout my undergraduate and graduate studies.

A special thanks to Elizabeth Maurer, for her support over the last few years. I love you.

Funding provided by the National Science Foundation, the southeastern section of the Geological Society of America, and Sigma Xi was much appreciated.

## Table of Contents

<b>Acknowledgements</b> .....	iv
<b>List of Tables</b> .....	vii
<b>List of Figures</b> .....	viii
<b>List of Plates</b> .....	xiv
<b>List of Abbreviations</b> .....	xv
<b>Introduction</b> .....	1
<b>Background</b> .....	4
<b>General Geology of the Area</b> .....	4
<b>The Laccolith/Stock Debate of the Henry Mountains</b> .....	8
<b>Recent Work in the Henry Mountains</b> .....	11
<b>Magma Flow Patterns in Sheet Intrusions</b> .....	16
<b>Recent Work with Magma Propagation</b> .....	17
<i>Magma Ascent</i> .....	18
<i>Magma Emplacement</i> .....	19
<i>Dike/Sill Transition</i> .....	21
<b>Methods</b> .....	24
<b>Field Work</b> .....	24
<b>Crystal Size Distribution</b> .....	26
<b>Thin Section Petrography</b> .....	28
<b>Geochemistry</b> .....	28
<b>Anisotropy of Magnetic Susceptibility</b> .....	29
<b>Results</b> .....	32
<b>A Note on Textural Terms</b> .....	32
<b>Field Work</b> .....	32
<b>Crystal Size Distribution</b> .....	45
<b>Thin Section Petrography</b> .....	49
<b>Geochemistry</b> .....	56
<b>Anisotropy of Magnetic Susceptibility</b> .....	62

<b>Discussion</b> .....	66
<b>Field Work</b> .....	66
<b>Crystal Size Distribution</b> .....	69
<b>Thin Section Petrography</b> .....	70
<b>Geochemistry</b> .....	72
<b>Anisotropy of Magnetic Susceptibility</b> .....	73
<b>Proposed Mount Hillers Construction Model</b> .....	76
<b>Conclusions</b> .....	79
<b>References Cited</b> .....	81
<b>Appendix A</b> Measurements of Sill Thickness .....	87
<b>Appendix B</b> Crystal Size Distribution Data .....	88
<b>Appendix C</b> Geochemistry Data .....	91
<b>Appendix D</b> Anisotropy of Magnetic Susceptibility Data .....	96

## List of Tables

1. Measure of Sill Thickness.....	87
2. CSD data for hornblende phenocrysts .....	88
3. CSD data for plagioclase phenocrysts .....	89
4. Whole-rock major element geochemistry data, dikes .....	91
5. Whole-rock major element geochemistry data, sills.....	91
6. Whole-rock trace element geochemistry data, dikes .....	92
7. Whole-rock trace element geochemistry data, sills .....	94
8. AMS data, dikes.....	96
9. AMS data, sills.....	99

## List of Figures

- Figure 1.** Aerial photograph compilation of the study area. Insets show: (A) Henry Mountains location in southern Utah; (B) Geologic map of the Henry Mountains, with field area outlined in red box; (C) Generalized cross section through Mount Hillers, marked on inset (B) by A – A'. Intrusive sheet network schematically represented by thin black lines on the southwest flank of the large central intrusion (insets modified from Horsman et al., 2010). ..... 3
- Figure 2.** Stratigraphic section of the Colorado Plateau in the Henry Mountains region. Cretaceous Dakota sandstone through Cedar Mesa member of the Permian Cutler Formation exposed on the southern flank of Mount Hillers (from Jackson and Pollard, 1988). ..... 5
- Figure 3.** Field photographs of igneous rocks of Mount Hillers. (A) Porphyry with two distinct plagioclase phenocryst sizes. For the purposes of this study, rocks with small phenocrysts (left) are referred to as "fine-grained," and those with large phenocrysts (right) are referred to as "coarse-grained." (B) Porphyry with large black amphibolite xenolith (center). Smaller amphibolite xenoliths are circled in red. .... 7
- Figure 4.** Cross section of an idealized laccolith, with domed overburden (from Gilbert, 1877). 8
- Figure 5.** Sketch of continued laccolith growth and the effect of marginal magma crystallization. Note that once the margins crystallize, lateral growth ceases, and remaining magma inflates, uplifting overburden. This model assumes that magma injection is continuous (modified from Pollard and Johnson, 1973, after Paige, 1913). ..... 10
- Figure 6.** (A) Cross section through the southern flank of Mount Hillers, illustrating the double-hinged deformation of overlying strata (from Jackson and Pollard, 1988). (B) Sketch of folding style associated with stock intrusion suggested by Hunt et al. (1953), not observed in the field (from Jackson and Pollard, 1988). The upper image illustrates the initial stock injection into undeformed strata; the lower image shows the buckled strata that would result from a radially expanding stock. .... 11
- Figure 7.** Schematic diagram illustrating competing pluton assembly hypotheses. (A) Pluton constructed from a single pulse in a large magma chamber. (B) Two plutons with identical geometries as (A), but showing different assemblies from small, incrementally intruded pulses of magma (modified from Horsman et al., 2010). ..... 12
- Figure 8.** Evidence for intrusion assembly from multiple pulses. (A, B) Bulbous lateral terminations of the Maiden Creek sill as described by Horsman et al. (2005). (C) Sharp internal

contact (dashed white line) in the Black Mesa bysmalith, marked by abrupt textural difference (Saint Blanquat et al., 2006). .....	14
<b>Figure 9.</b> Exploitation of preexisting fractures in sedimentary strata by dark gray basaltic dike (from Le Corvec et al., 2013).....	18
<b>Figure 10.</b> Cross section of Trachyte Mesa laccolith, eastern flank of Mount Hillers, Henry Mountains, illustrating flat roof and sharply bent overburden at intrusion margin (from Morgan et al., 2008). Vertical Exaggeration is 2.5x.....	20
<b>Figure 11.</b> Diagram showing density versus depth through the crust. The solid black line represents bulk crustal density. Granitic magma densities are represented to the left in light grey, while gabbroic magma densities are to the right in dark grey. Note that granitic and intermediate magmas should never reach a point of neutral buoyancy in the crust (from Vigneresse and Clemens, 2000). .....	21
<b>Figure 12.</b> Experimental work showing dyed water (magma analogue) injected into layers of gelatin (host rock analogue). Layers of lower rigidity allowed vertical ascent, and lateral emplacement began at the lower contact of more rigid overburden (from Kavanagh et al., 2006). .....	23
<b>Figure 13.</b> A plot of susceptibility vs. temperature for 12 samples from the intrusive sheet network on the southern flank of Mount Hillers. The susceptibilities of all samples is dominated by magnetite (Curie $T \approx 570$ °C), as shown by the drop in susceptibility at 550-600 °C.....	31
<b>Figure 14.</b> Geologic map of the southern margin of Mount Hillers. Station locations and stations where oriented samples were collected are noted. Cross section transects A-A', B-B', and C-C' are also marked. ....	33
<b>Figure 15.</b> Geologic map of the southern margin of Mount Hillers with bedding measurements. ....	34
<b>Figure 16.</b> Picture of Jurassic Salt Wash outcrop, facing north. Bedding gradually steepens from east to west (right to left). ....	35
<b>Figure 17.</b> Cross sections (transects from Figure 13) of the southern margin of Mount Hillers with no vertical exaggeration. Note the double hinged geometry of the sedimentary strata. A-A' transect located in the SW region. B-B' transect located in the S-SE region. C-C' transect located in the E region. Faulted contacts included based on Jackson and Pollard (1990).....	36

**Figure 18.** Pictures of intrusion geometries. (A) Bedding-concordant sill, with 10+ meter segments separated by areas with no igneous outcrop. Mount Holmes (left) and Mount Ellsworth (right) in the background. (B) Dike pseudo-swarm displaying discontinuous outcrop pattern common in the field area. Mount Hillers sister peak in the background. .... 39

**Figure 19.** Pictures illustrating the relative ages of dikes and sills. Relevant features are marked or outlined. (A) Light-colored, coarse-grained sill terminating against a dark-colored, fine-grained dike, outcrop scale. Field book for scale. (B) Fine-grained dike (left) cross-cutting a coarse-grained sill (right), with a sheared contact. Pencil for scale. (C) Large, fine-grained dike subvertically cross-cutting a coarse-grained sill. (D) Cross-cutting contact between a fine-grained dike (right) and a coarse-grained sill (left). Pencil for scale. (E & F) Fine-grained dike float with coarse-grained igneous inclusions. Pencils for scale..... 40

**Figure 20.** Equal angle lower hemisphere stereographic projections of long axis orientations of elongate hornblende phenocrysts from sills (A, B, C) and dikes (D, E, F) in the three regions (SW, S-SE, E) of the study area. Grey dots represent measured field fabric orientations, colored squares represent fabrics rotated around the strike of bedding to paleo-horizontal, and colored lines represent the general orientation of regional dikes. .... 41

**Figure 21.** Photograph of stepped intrusive margin, individual step edges outlined in red. Possible flow directions indicated by arrow. Pen for scale. .... 42

**Figure 22.** Photographs of possible feeder dikes on Mount Hillers. Features outlined and labeled. (A) Sill intruding the contact between Entrada and Summerville (now eroded) formations in the Gold Creek region. Feeder dike shown capping the sedimentary exposure. (B) Feeder dike and sill intruding the Navajo formation sandstone in the southwest region of the study area. Inset shows the location of these intrusions within the Navajo outcrop. .... 43

**Figure 23.** Fluidized breccia of maroon Chinle formation shale and porphyry fragments, outlined in red. Pencil for scale..... 44

**Figure 24.** Photograph from the southeastern region, looking north. Dark grey sills (Td, outlined in red) of varying thickness observed in a relatively small area. West sill (left) is ~3-5 meters thick, and intrudes rigid, competent Navajo sandstone (J-Tr n). East sill (right) is ~10 meters thick, and intrudes the contact between competent Entrada sandstone (Je) and overlying incompetent Summerville shale (Js, now eroded away)..... 45

**Figure 25.** Pictures of CSD samples at different stages of processing. (A) Fine- (left), medium- (middle), and coarse-grained (right) samples are slabbed and scanned. (B) ImageJ is used to prepare the image for analysis, which includes removing the background from the scanner hood

and any weathered segment of the slab, and deleting any xenoliths which would disrupt hornblende CSD results. (C) Threshold is adjusted to produce a binary image, with black polygons representing the crystals of interest (in this case, plagioclase phenocrysts). ..... 46

**Figure 26.** Crystal size distributions for hornblende phenocrysts in fine-, medium-, and coarse-grained samples..... 46

**Figure 27.** Crystal size distributions for plagioclase phenocrysts in fine-, medium-, and coarse-grained samples..... 47

**Figure 28.** Characteristic length vs. intercept of plagioclase crystals in all analyzed samples... 48

**Figure 29.** Photomicrographs taken in plane-polarized light, showing textural variation between cross-cutting intrusive sheets. All images captured at 2x magnification. (A) CC3a is a sill, cross-cut by (B) CC3b; (C) CC7b is a sill, cross-cut by (D) CC7a; (E) CC81b is a sill, cross-cut by (F) CC81a; (G) CC160b is a sill, cross-cut by (H) CC160a. All sills (left) have notably larger plagioclase phenocrysts than dikes (right). ..... 51

**Figure 30.** Photomicrographs taken in plane-polarized light, comparing CIB texture (A, CC94) and fine- to medium-grained dike texture (B, C, D). B, C, and D are CC3b, CC81a, and CC160a, respectively. .... 52

**Figure 31.** Photomicrographs taken in plane-polarized light, comparing CC57a (A, sill) and CC57b (B, dike), from intrusive sheets in the eastern region of the field area..... 52

**Figure 32.** Photomicrographs taken in plane-polarized light, showing select features and alteration in phenocrysts. (A) Plagioclase phenocryst with extensive fracturing and associated alteration. (B) Plagioclase phenocrysts with alteration halos of sericite(?) surrounding the cores. These halos mirror the zoning orientations. (C, D) Hornblende phenocrysts extensively altered to pseudomorphic chlorite, calcite and magnetite..... 54

**Figure 33.** Photomicrographs taken in cross-polarized light, presenting select features in the four lowest exposed sedimentary units on Mount Hillers. (A) Moenkopi formation, quartz grains in a chlorite groundmass, with magnetite crystals. (B) White Rim sandstone, now metamorphosed to quartzite. Preserved bedding (parallel to top and bottom of photo) is defined by subparallel zones of relatively fine-grained quartz. (C) Organ Rock Tongue, metamorphosed to hornfels, quartz grains in a chlorite groundmass. Veinlet of actinolite and chlorite observed on the right. (D) Photomicrograph stitch of Cedar Mesa sandstone (left) contacting porphyry sill (right). Cedar Mesa is metamorphosed to quartzite. Quartz grain inclusions are observed within the igneous porphyry..... 55

<b>Figure 34.</b> Total alkalis (Na <sub>2</sub> O + K <sub>2</sub> O) versus silica (SiO <sub>2</sub> ) diagram (Le Bas et al., 1986) for samples from twelve intrusive sheets on the southern flank of Mount Hillers.....	56
<b>Figure 35.</b> Select major and trace element abundances which show statistically significant variation with respect to grain size, mapped at their sampling locations. (A) K <sub>2</sub> O abundances in weight %. (B) Rb abundances in ppm. (C) Zr abundances in ppm. (D) Nd abundances in ppm. ....	57
<b>Figure 36.</b> Select trace element variations (ppm) versus SiO <sub>2</sub> (wt. %) diagrams for fine-, medium-, and coarse-grained samples. (A) Zr vs. SiO <sub>2</sub> . (B) Th vs. SiO <sub>2</sub> . (C) La vs. SiO <sub>2</sub> . (D) Nd vs. SiO <sub>2</sub> .....	60
<b>Figure 37.</b> Chondrite-normalized (McDonough and Sun, 1995) REE patterns for fine-, medium-, and coarse-grained intrusion samples. (A) Fine-grained REE patterns. (B) Medium-grained REE patterns. (C) Coarse-grained REE patterns. (D) Normalized average grain size REE patterns for fine-, medium-, and coarse-grained samples. ....	61
<b>Figure 38.</b> Chondrite-normalized (McDonough and Sun, 1995) REE patterns for dikes and sills. (A) Dike REE patterns. (B) Sill REE patterns. (C) Normalized dike and sill average REE patterns.....	61
<b>Figure 39.</b> Equal angle lower hemisphere stereographic projections of magnetic lineations of sills (A, B, C) and dikes (D, E, F) in the three regions (SW, S-SE, E) of the study area. Grey dots represent measured AMS lineation orientations, colored squares represent lineations rotated around the strike of bedding to paleo-horizontal, and colored lines represent the general orientation of regional sills and dikes. ....	62
<b>Figure 40.</b> Equal angle lower hemisphere stereographic projections of measured and rotated magnetic foliations of sills (A, B) and dikes (C) in the three regions (SW, S-SE, E) of the study area. Grey dots represent measured AMS lineation orientations, colored squares represent lineations rotated around the strike of bedding to paleo-horizontal, and colored lines represent the general orientation of regional sills and dikes. ....	63
<b>Figure 41.</b> Plots of AMS scalar parameters based on grain-size (A, B, C) and intrusion type (D, E, F). (A, D) Shape parameter vs. bulk susceptibility. (B, E) Shape parameter vs. degree of anisotropy. (C, F) Degree of anisotropy vs. bulk susceptibility. ....	65
<b>Figure 42.</b> Schematic diagrams of general finger geometries observed in intrusive sheets. (A) Map view of a subsurface sill, outlined in red. Finger-like protrusions line the margins of a	

central continuous body. (B) Block diagram of the fingered margin of a sill (red) between sedimentary host rock (black). Strata and sill have been tilted to subvertical to mirror attitudes on the southern margin of Mount Hillers. (C) Block diagram of strata and sill, now eroded to resemble observations from the southern margin of Mount Hillers. .... 67

**Figure 43.** Schematic construction model for the intrusive sheet network on the southern margin of Mount Hillers. (A) Sills, fed by subvertical dikes, intrude the Phanerozoic sedimentary strata. The incipient CIB intrudes near the base of the Permian Cutler formation, growing over a large lateral extent. (B) The CIB begins doming the overburden as vertical growth begins. Sills continue to intrude the host rock, and radial dikes cut through both overlying sediments and sills. (C) As growth of the CIB continues, overburden is sharply bent and rotated. Late sills intrude the bent overburden, and late radial dikes remain unrotated as growth of the CIB concludes..... 78

## **List of Plates**

**Plate 1.** Geologic Map of the southern margin of Mount Hillers

**Plate 2.** Radial cross sections from the southern margin of Mount Hillers

## List of Abbreviations

CIB	Central igneous body .....	2
Ar	Argon .....	11
U	Uranium .....	11
Pb	Lead.....	11
CSD	Crystal size distribution .....	26
ICP-MS	Inductively coupled plasma mass spectrometry .....	28
AMS	Anisotropy of magnetic susceptibility .....	29
Q	Quaternary.....	36
T	Tertiary .....	36
K	Cretaceous.....	36
J	Jurassic .....	36
Tr	Triassic .....	36
P	Permian .....	36
FeTi	Iron-titanium .....	49
Ep	Epidote .....	51
Hbl	Hornblende.....	51
Mag	Magnetite .....	51
Plag	Plagioclase .....	51
Cal	Calcite.....	54
Chl	Chlorite .....	54
Ser	Sericite .....	54
Act	Actinolite.....	55
Qtz	Quartz.....	55

K	Potassium .....	56
Na	Sodium .....	56
O	Oxygen .....	56
Si	Silicon .....	56
Ce	Cerium .....	57
Dy	Dysprosium .....	57
Hf	Hafnium .....	57
La	Lanthanum .....	57
Lu	Lutetium .....	57
Nd	Neodymium.....	57
Pr	Praseodymium .....	57
Rb	Rubidium.....	57
Sm	Samarium .....	57
Th	Thorium .....	57
Zr	Zirconium.....	57
REE	Rare earth element .....	60
Eu	Europium.....	60
Tm	Thulium.....	60
Gd	Gadolinium .....	61
Tb	Terbium.....	61
Ho	Holmium .....	61
Er	Erbium.....	61
Yb	Ytterbium .....	61

## **Introduction**

Dikes and sills are the primary conduits through which magma moves in the shallow parts of the crust (Muirhead et al., 2012). These intrusions can feed batholiths which are major components in the assembly of continental crust (Hawkesworth et al., 2010). Interconnected networks of dikes and sills also comprise the roots and internal plumbing of volcanic systems (Bachmann et al., 2007). Therefore, understanding how these intrusive sheets form is vital to our overall understanding of continental crust construction and volcanic hazards.

The study of shallow crustal igneous intrusions and the magmatic processes involved in their construction is often complicated. Modern shallow igneous systems must be studied indirectly, using geophysical methods, analysis of eruptive products, etc. Even when erosion has exposed the internal dikes and sills of ancient volcanic systems, syn- and post-emplacement deformation can alter or altogether destroy evidence of magmatic processes (Barbey, 2009). These complications can be avoided by studying ancient intrusions with no tectonic overprint.

One such area is located on the southern margin of Mount Hillers (Figure 1), of the Henry Mountains in southern Utah, where an intricate complex of dikes and sills is exposed in tilted Phanerozoic sedimentary strata. These mid-Tertiary (~25 Ma) intrusions (Paquette et al., 2010) were emplaced into the upper 2-4 kilometers of the crust (Jackson and Pollard, 1988) during a time of tectonic inactivity on this part of the Colorado Plateau (Allmendinger et al., 1987; Horsman et al., 2010). Mount Hillers itself is a large laccolithic body (Figure 1C), which likely directly fed some of the intrusive sheets. The igneous rocks are diorite in composition, and rapid cooling produced porphyritic texture that preserves fabrics produced by magma flow.

These characteristics, along with exceptional 3-d exposure, make this field area ideally suited to study magma transport through the upper few kilometers of the crust.

For this study, a detailed study of the intrusive sheet complex was conducted. Field work included thorough mapping of intrusive sheet geometries and cross-cutting relationships, textural analysis, field fabric measurement, oriented sample collection, and sill thickness measurements. Lab work included crystal size distribution analysis, thin section petrography, whole-rock major and trace element geochemistry, and fabric quantification through anisotropy of magnetic susceptibility. These methods were used to test three main hypotheses: 1) *Pulsed construction* - Three or more distinct magma pulses are preserved in the construction of the dike/sill network, with sills generally representing older pulses and dikes younger pulses; 2) *Magmatic flow characteristics* - Separate magma flows resulting from these pulses generally flowed outward from the central igneous body (CIB); and 3) *Host rock mechanical heterogeneity* - The intrusive sheets exploited preexisting planes of weakness as areas to intrude, and host rock mechanical heterogeneity was a major factor in the transition from dike to sill.

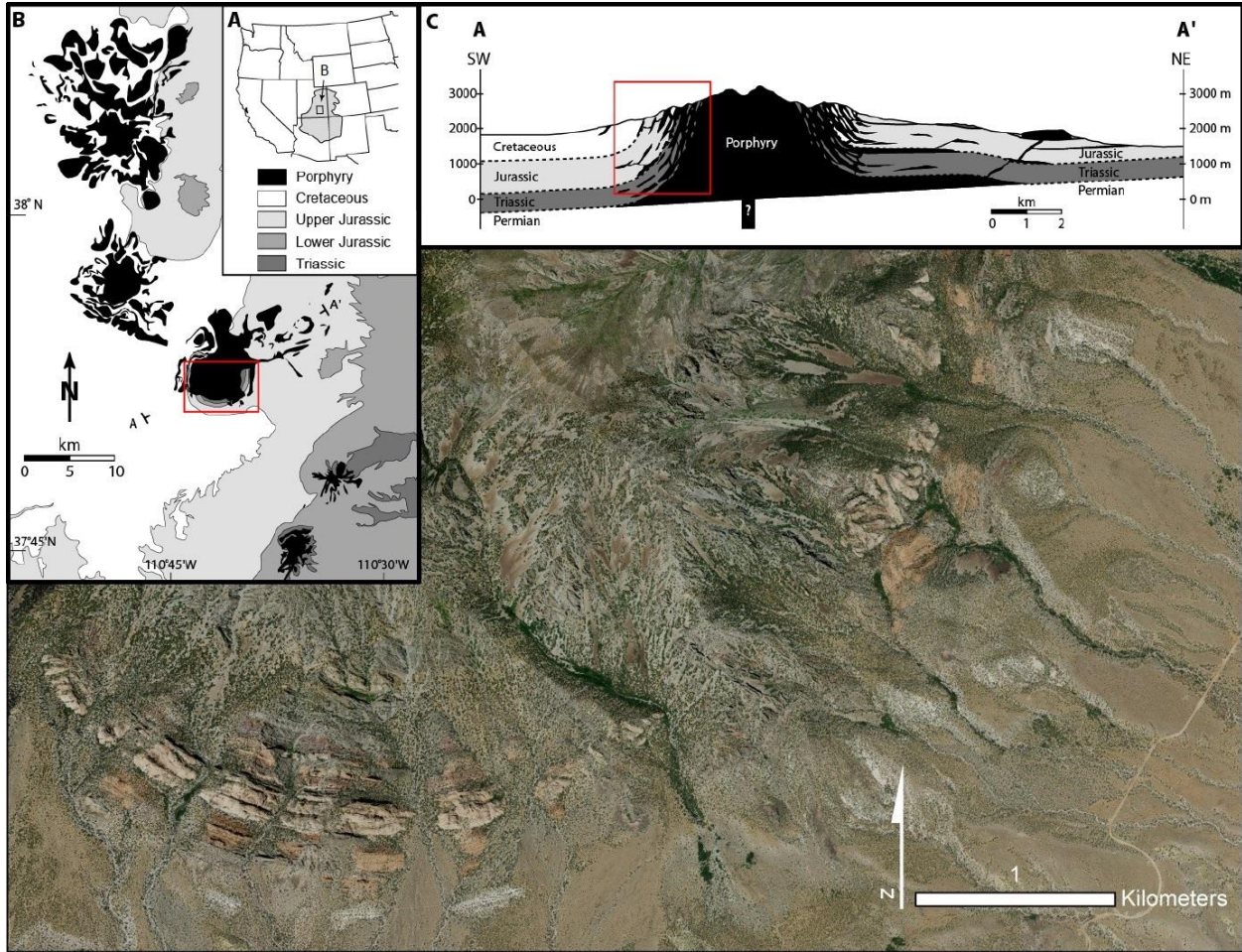


Figure 1. Aerial photograph compilation of the study area. Insets show: (A) Henry Mountains location in southern Utah; (B) Geologic map of the Henry Mountains, with field area outlined in red box; (C) Generalized cross section through Mount Hillers, marked on inset (B) by A – A'. Intrusive sheet network schematically represented by thin black lines on the southwest flank of the large central intrusion (insets modified from Horsman et al., 2010).

## **Background**

### **General Geology of the Area**

The Colorado Plateau (Figure 1A) is a large physiographic province located in the southwestern United States, and has been relatively stable during the Phanerozoic. Sediment deposition over the past 600 million years is recorded in the stratigraphy of the region; it is within these sedimentary rocks that the igneous rocks of the Henry Mountains reside. Regional stratigraphy is subhorizontal, with a general dip of  $\sim 2^\circ$  to the west (Jackson and Pollard, 1988). The oldest exposed unit in the Henry Mountains region is the Permian Cutler Formation, while the youngest unit is the Cretaceous Mesa Verde Formation (Figure 2). According to Doelling (1975), there was no more than 3.7 km of overburden when magma intruded to form the Henry Mountains intrusions.

Cratonic crust of substantial thickness (45-50 km) underlies the Colorado Plateau (Thompson and Zoback, 1979). This thick crust may account for the lack of regional deformation on this part of the Colorado Plateau despite the complex Phanerozoic tectonic history throughout the rest of the western North American Cordillera. Surrounding areas have experienced some regional deformation, however. Large-scale folds such as Waterpocket Fold and the San Rafael Swell (west and north of the Henry Mountains, respectively) formed due to uplift and regional shortening during the Laramide Orogeny around 72-50 Ma (Bump, 2004). This deformation predates the intrusive activity of the Henry Mountains (32-23 Ma, Nelson et al., 1992), and no evidence for syn- or post-emplacement deformation exists in the Henry Mountains. Therefore, structures and fabrics found in the rocks can be attributed to purely magmatic processes.

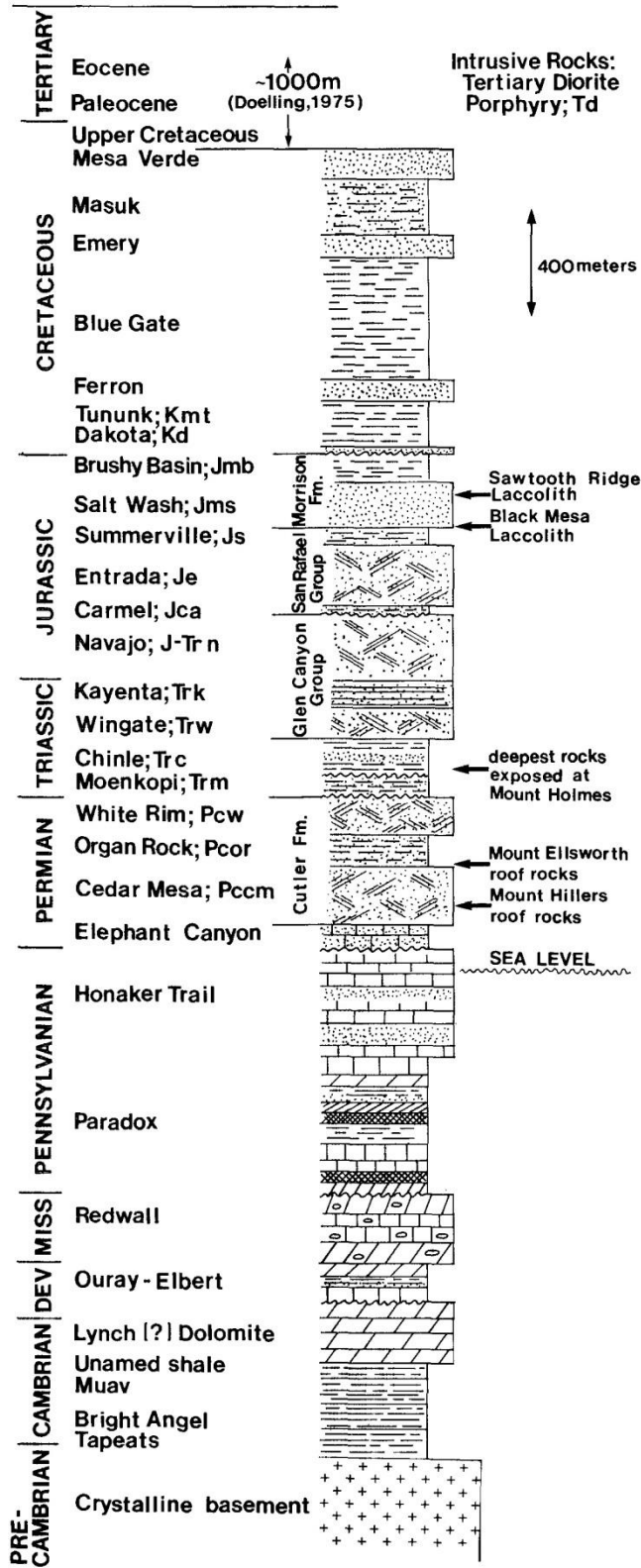


Figure 2. Stratigraphic section of the Colorado Plateau in the Henry Mountains region. Cretaceous Dakota sandstone through Cedar Mesa member of the Permian Cutler Formation exposed on the southern flank of Mount Hillers (from Jackson and Pollard, 1988).

Intense mid-Tertiary magmatism occurred in the regions surrounding the Colorado Plateau. The San Juan and Reno-Marysvale volcanic fields lie adjacent to the Colorado Plateau and are concurrent with less voluminous magmatic activity on the Colorado Plateau that formed the Abajo, La Sal, and Henry Mountains. The extensive nature of this magmatism suggests an east-west magmatic belt existed in the late Oligocene (Nelson and Davidson, 1993).

The Henry Mountains consist of five igneous intrusive centers arranged in a general NNW-SSE trend (Figure 1B). From north to south, these centers are Mount Ellen, Mount Pennell, Mount Hillers, Mount Holmes, and Mount Ellsworth. Each intrusive center is cored by a central laccolithic igneous body. Less voluminous satellite intrusions (dikes, sills, small laccoliths) flank the intrusive cores of each mountain (Gilbert, 1877; Hunt et al., 1953; Jackson and Pollard, 1988). There are two distinct rock compositions in the Henry Mountains: A fairly homogenous plagioclase-hornblende porphyry found in all five intrusive centers and a syenite porphyry, restricted to parts of Mount Pennell.

Mount Hillers is cored by a central laccolithic body with a radius of 6-7 km (Jackson and Pollard, 1988), and is surrounded to the north and east by a series of satellite intrusions and to the south by a complex of crosscutting dikes and sills. Total volume of magma associated with Mount Hillers has been estimated most recently at  $\sim 34 \text{ km}^3$  (Jackson and Pollard, 1988). Exposed igneous rock has a bulk andesite/trachyandesite composition. Texturally, the rock is a plagioclase-hornblende porphyry. Textural variations are defined by plagioclase phenocryst size (Figure 3A), and amphibolite xenoliths (Figure 3B) represent pieces of the Proterozoic basement rock underlying the Phanerozoic sedimentary strata (Figure 2). Deformation of the host strata is extensive; sedimentary beds have been upturned and tilted to near vertical along the southern

margin by the growth of the CIB. Maximum upward deflection of strata around Mount Hillers is 2.5-3.0 km.

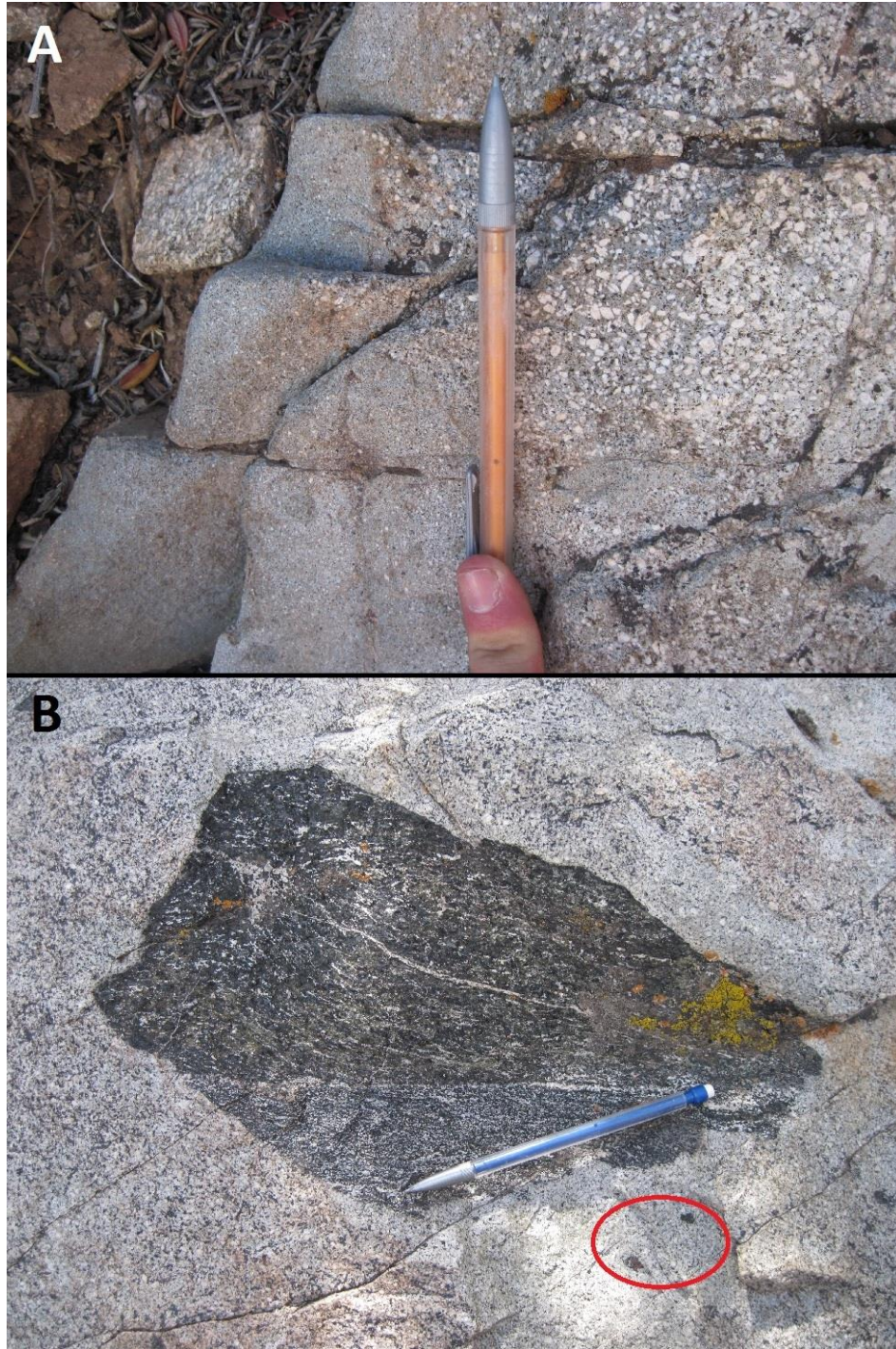


Figure 3. Field photographs of igneous rocks of Mount Hillers. (A) Porphyry with two distinct plagioclase phenocryst sizes. For the purposes of this study, rocks with small phenocrysts (left) are referred to as "fine-grained," and those with large phenocrysts (right) are referred to as "coarse-grained." (B) Porphyry with large black amphibolite xenolith (center). Smaller amphibolite xenoliths are circled in red.

## The Laccolith/Stock Debate of the Henry Mountains

Prior to publication of Gilbert's (1877) report on the Henry Mountains, it was believed that intruding magma in the shallow crust could not deform host rock. Gilbert, however, observed displacement and deformation of strata adjacent to the intrusions and described it in detail. He concluded that the igneous rocks were not volcanic but intrusive, that sedimentary units were bent upward above intrusions, and intruding magma made space for itself by uplifting the overburden. Gilbert (1877) published these observations, named the related intrusion a laccolite (now laccolith), and described such an intrusion as having a circular map geometry and a cross sectional geometry "such as the half of an oblate spheroid" (Figure 4).

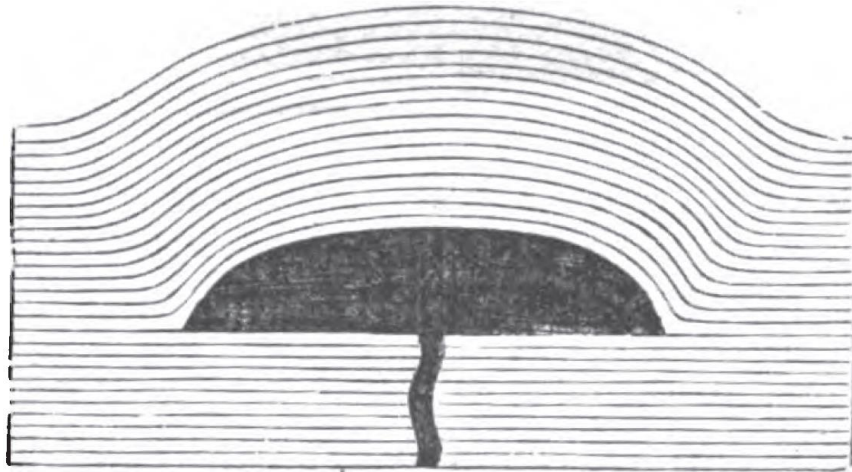


Figure 4. Cross section of an idealized laccolith, with domed overburden (from Gilbert, 1877).

Hunt et al. (1953) produced the first geologic map of the area, and made numerous observations related to the rocks and structures of each of the five Henry Mountains intrusive centers. These authors hypothesized that instead of largely concordant laccoliths, each Henry Mountains intrusive center is cored by a discordant cylindrical stock within an area of structurally complex host rock, intrusive sheets, and intrusions of irregular geometry termed the

“shattered zone.” According to Hunt et al. (1953), these stocks first ascended vertically and then expanded radially, deforming the host rock and leading to the development of the shattered zone. Following stock intrusion, tongue-shaped sills and laccoliths were fed by and intruded radially outward from the central stock.

Johnson and Pollard (1973) and Pollard and Johnson (1973) focused on growth mechanics of sills and their transition into laccoliths. They observed characteristic thicknesses and lengths for various satellite sills and laccoliths in the Henry Mountains, noting that sills were consistently thinner and had smaller areal extents than laccoliths. The data suggest that magma must propagate over a sufficient area ( $>1 \text{ km}^2$  in the Henry Mountains) to achieve sufficient leverage to lift the overburden (Johnson and Pollard, 1973). Crystallization of magma along the intrusion periphery (Figure 5) may also act as a catalyst for upward inflation (Pollard and Johnson, 1973, as suggested by Paige, 1913), as the overlying strata would prove less resistant to deformation than the newly formed marginal igneous rock. The relevant conclusion drawn from these studies is that once magma intrudes over a lateral distance of about three times the thickness of overlying strata, significant vertical intrusion growth may begin. The dimensions of the central intrusion of Mount Hillers (~12-14 km, Jackson and Pollard, 1988) and thickness of overburden ( $\leq 3.7 \text{ km}$ , Doelling, 1975) are consistent with a central intrusive laccolith for Mount Hillers. It is important to note that these authors (Johnson and Pollard, 1973; Pollard and Johnson, 1973) assumed a continuous injection of magma for their calculations and interpretations.

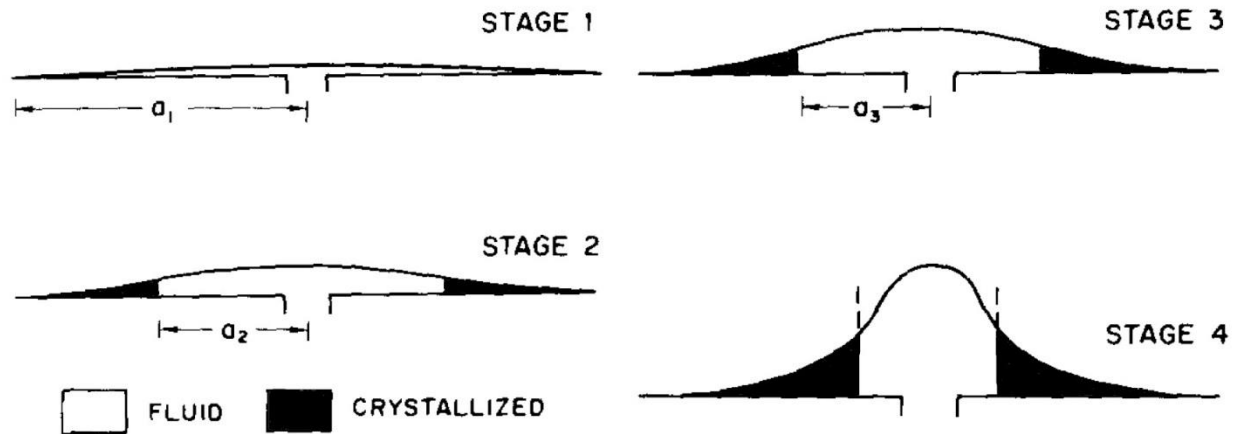


Figure 5. Sketch of continued laccolith growth and the effect of marginal magma crystallization. Note that once the margins crystallize, lateral growth ceases, and remaining magma inflates, uplifting overburden. This model assumes that magma injection is continuous (modified from Pollard and Johnson, 1973, after Paige, 1913).

Jackson and Pollard (1988) developed a growth history model for Mount Hillers based on field observations and geophysical data. Their observations are most consistent with a central laccolithic intrusive body for the igneous cores of the Henry Mountains. In the Jackson and Pollard (1988) cross sections, the sedimentary strata are bent into a double-hinged shape (Figure 6A), which supports a generally laccolithic geometry for the CIB. If a central stock had radially expanded as suggested by Hunt et al. (1953), buckle folds (Figure 6B) should be observable in the sedimentary units surrounding the intrusive centers. Paleomagnetic data taken from overlying sheet intrusions indicate that these sills and small laccoliths were emplaced subhorizontally and later rotated  $\sim 80\text{-}90^\circ$  (Jackson and Pollard, 1988), which supports the hypothesis of central laccolith doming. Finally, aeromagnetic data are consistent with a floored laccolith beneath each mountain, although modeled magnetic profiles based on both laccolith and stock geometries are consistent with the measured magnetic profile.

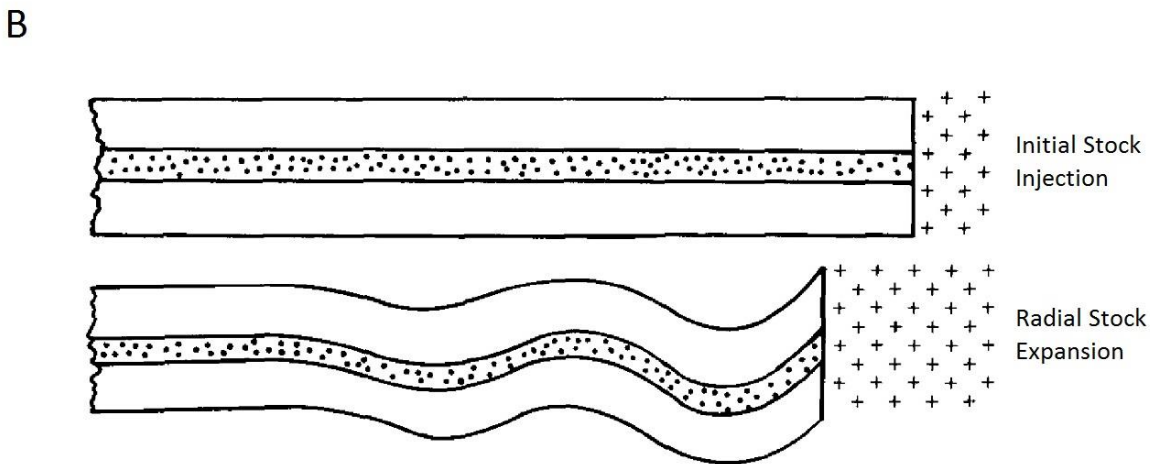
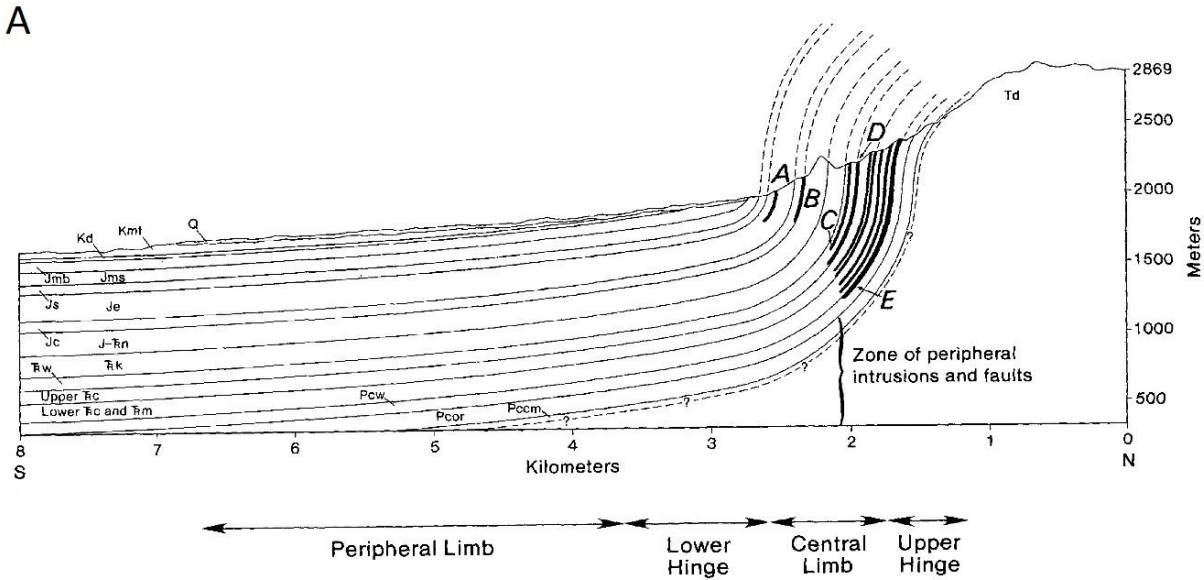


Figure 6. (A) Cross section through the southern flank of Mount Hillers, illustrating the double-hinged deformation of overlying strata (from Jackson and Pollard, 1988). (B) Sketch of folding style associated with stock intrusion suggested by Hunt et al. (1953), not observed in the field (from Jackson and Pollard, 1988). The upper image illustrates the initial stock injection into undeformed strata; the lower image shows the buckled strata that would result from a radially expanding stock.

## Recent Work in the Henry Mountains

$^{40}\text{Ar}/^{39}\text{Ar}$  and fission track dates provide Oligocene to early Miocene ages of 32-23 Ma for igneous rocks of the Henry Mountains (Nelson et al., 1992). Paquette et al. (2010) used U-Pb zircon dating of 10 samples from Mount Hillers obtain a refined age of  $24.75 \pm 0.50$  Ma for this intrusive center. Nelson and Davidson (1993) suggested basaltic magma underplated and melted

the lower crust of the Colorado Plateau. These melts underwent assimilation and fractional crystallization during mid-crustal storage and evolved into the igneous rocks observed in the Henry Mountains.

Recent work involving magmatism in the shallow crust has focused on several fundamental issues. One important issue is the frequency of magma injection during assembly of shallow intrusions. The traditional ‘big tank’ hypothesis, where intrusive bodies of all sizes form from a single large magma chamber (Figure 7A), has been extensively studied in the past (e.g. Bateman, 1992). More recent research, however, provides evidence for an alternate hypothesis: Plutons (from batholiths to individual sills) can incrementally form from multiple, sequentially emplaced pulses of magma (Figure 7B, Coleman et al., 2004; Saint Blanquat et al., 2011). Some of this work has focused on intrusions in the Henry Mountains, and a brief review of these studies follows.

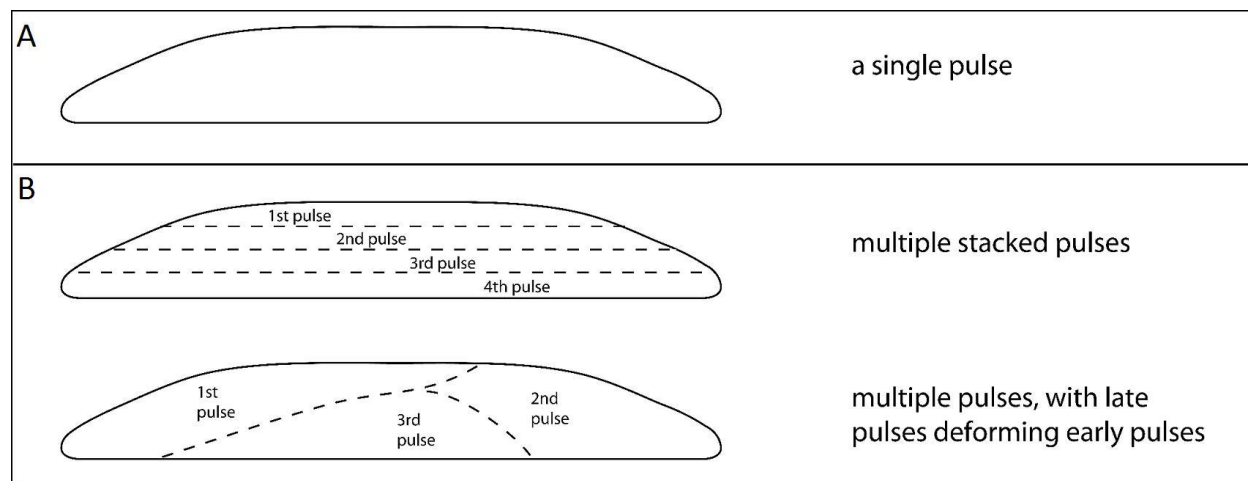


Figure 7. Schematic diagram illustrating competing pluton assembly hypotheses. (A) Pluton constructed from a single pulse in a large magma chamber. (B) Two plutons with identical geometries as (A), but showing different assemblies from small, incrementally intruded pulses of magma (modified from Horsman et al., 2010).

The Maiden Creek sill is a sheet intrusion located on the eastern flank of Mount Hillers. Horsman et al. (2005) observed two continuous bulbous terminations (Figure 8A, 8B), local

igneous-igneous contact rocks showing solid-state deformation, and intercalated sedimentary blocks that spatially correspond with the igneous-igneous contacts. These observations suggest this sheet intrusion was constructed by two successive pulses of magma. Multiple finger-like lobes splay out from the center of the intrusion. Horsman et al. (2005) suggest that magma propagation may initiate at the tips of these fingers, which supports previous hypotheses about how magma moves through the shallow crust (Pollard et al., 1975). Finally, magmatic fabric analysis suggests that magma flowed from a feeder positioned between the intrusion and the central igneous dome of Mount Hillers, and an outward flow from the center of the Maiden Creek sill to the fingered lobes is inferred based on general alignment of fabric lineations with the long axes of the lobes (Horsman et al., 2005).

Saint Blanquat et al. (2006) determined that the Black Mesa bysmalith, a cylindrical satellite intrusion on Mount Hillers' eastern flank, was emplaced by sequential magma pulses ascending from below. These pulses progressively accreted to the underside of the previous magma sheet, and the emplacement took no more than 100 years. Evidence for multiple pulses includes observable internal contacts. No solid-state deformation accompanied these inferred pulses, but marked differences in phenocryst size (Figure 8C) made identification of these magmatic layers possible. The differing magmatic fabric patterns at different levels of the intrusion further strengthen the hypothesis for progressive pulsed intrusion.

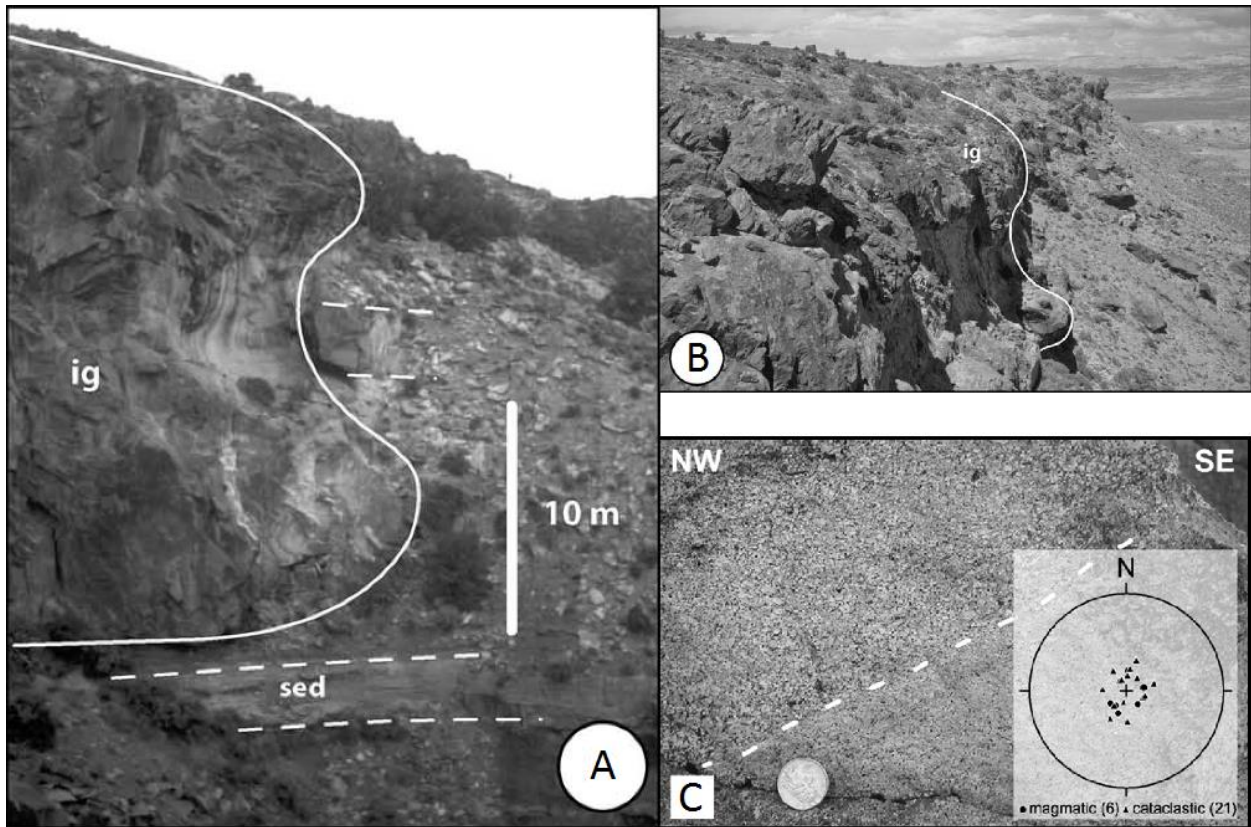


Figure 8. Evidence for intrusion assembly from multiple pulses. (A, B) Bulbous lateral terminations of the Maiden Creek sill as described by Horsman et al. (2005). (C) Sharp internal contact (dashed white line) in the Black Mesa bysmalith, marked by abrupt textural difference (Saint Blanquat et al., 2006).

A third satellite intrusion flanking Mount Hillers to the east, the Trachyte Mesa laccolith, was studied by Morgan et al. (2008). Successively emplaced magma pulses, likely from a lateral, Mount Hillers-based feeder, are evidenced by multiple bulbous terminations and sheared internal contacts, both subhorizontal and sub-parallel to the upper and lower contacts of the intrusion. Magnetic lineations are consistent with a general magmatic flow direction from SW to NE, and diverging flow from a centralized channel out toward the intrusion margins. Each magmatic pulse intruded as a distinct sheet and stacked above the previous sheet, and the overlying sedimentary rock was deformed, uplifted, and bent above the intrusive margins.

Horsman et al. (2010) compiled the results and interpretations from the Maiden Creek, Black Mesa, and Trachyte Mesa intrusions and developed a model for the pulsed construction of an idealized upper-crustal pluton:

- Sill - During early assembly of an intrusion, a single pulse of magma emplaces as a single sheet, propagating along the tips of fingered lobes. Subsequent infusions of magma from the feeder are likely to travel relatively similar emplacement routes, to create a stack of individual sheets that form a single intrusion.
- Laccolith - Continued pulses of magma lead to increased emplacement of sheets that terminate near the margins of the preceding sheets. The increasing intrusion height from sheet stacking has a similar effect to the single pulse, central localized inflation suggested by Johnson and Pollard (1973) and Pollard and Johnson (1973): the overburden is deformed, uplifted, and bent at the margins.
- Bysmalith - If pulsed assembly continues for a long enough time, thickness increases until overburden is faulted along the steep perimeter of the intrusion.

Saint Blanquat et al. (2011) establish a direct correlation between intrusion size and associated construction time: the more voluminous the intrusion, the longer the assembly time. Pulsed assembly is common in intrusions of various sizes, from single sheets (forming within several years) to entire intrusive suites (forming over millions of years). Within these different intrusions, there are multiple orders of pulsed assembly, the volumes of which depend on the size of the intrusion. It is important to note that the term “pulse” is typically reserved for an injection of magma into single pluton. This study focuses on a network of numerous, cross-cutting sills and dikes, each presumably consisting of a single sheet. Therefore, “pulse” used herein is not

referring to the magma pulses in the classical sense. Instead, for the purposes of this study, pulses refer to separate batches of magma with distinct relative ages and crystallization histories.

### **Magma Flow Patterns in Sheet Intrusions**

Knight and Walker (1988) studied magma flow in sheeted dikes of the Koolau complex, Oahu. Observed macroscopic surface lineations in the rocks (defined by parallel, millimeter-high wrinkles) were assumed as parallel with magma flow direction. The authors found excellent agreement in the alignment of long axes of magnetic fabrics with these surface lineations; therefore, the long axes of magnetic fabrics were inferred to be generally parallel to magma flow direction. Many subsequent studies (e.g. Cadman et al., 1992; Ernst and Baragar, 1992; Raposo and Ernesto, 1995; Varga et al., 1998; Ferré et al., 2001) have made interpretations about magma flow based on the assumption that long axes of magnetic fabrics align parallel to magma flow. In his review of magnetic fabrics in igneous rocks, Cañón-Tapia (2004) concludes that the findings of Knight and Walker (1988) are far from conclusive. Complications in fabric interpretations may arise from many factors, including, but not limited to, post-emplacement stresses (Park et al., 1988), hydrothermal alteration (Rochette et al., 1991), and inverse fabrics (long axes perpendicular to the intrusion plane) caused by single domain magnetite (Rochette et al., 1991; Rochette et al., 1992). If the aforementioned complications can be limited (such as with rocks lacking a tectonic overprint and magnetic mineralogy dominated by multi-domain magnetite), basic interpretations about magma flow can be made using the long axes of magnetic fabrics.

## **Recent Work with Magma Propagation**

The controls on magma movement through the shallow crust have been the subject of much study (e.g. Petford et al., 2000). Magma is transported from depth through magma ascent mechanisms. Upon reaching the shallow crust, vertical ascent may cease and give way to lateral magma emplacement. These stages of magma propagation are governed by a variety of factors and processes, discussed below.

In the shallow crust, rocks behave and deform in a brittle fashion; regional stresses cause strain in the form of fractures and faults. This behavior has implications for the movement of magma through these rocks. The surface of the earth is a free surface with no shear stress, forcing one principal stress direction to be perpendicular to it (Fossen, 2010). This results in surface-perpendicular and surface-parallel stresses and fractures. Assuming host rocks are horizontal sedimentary beds, these fractures are bedding perpendicular and parallel, respectively. Magma propagation is affected by these preexisting planes of weakness (Corvec et al., 2013), and may exploit these (Figure 9) and other (e.g. bedding planes) features. Pressurized magma may also pierce solid host rock (Kavanagh et al., 2006), allowing for magma transport in the absence of preexisting features; other related space-making processes include stoping and brecciation of magma-adjacent wall rock (Glazner and Bartley, 2006).

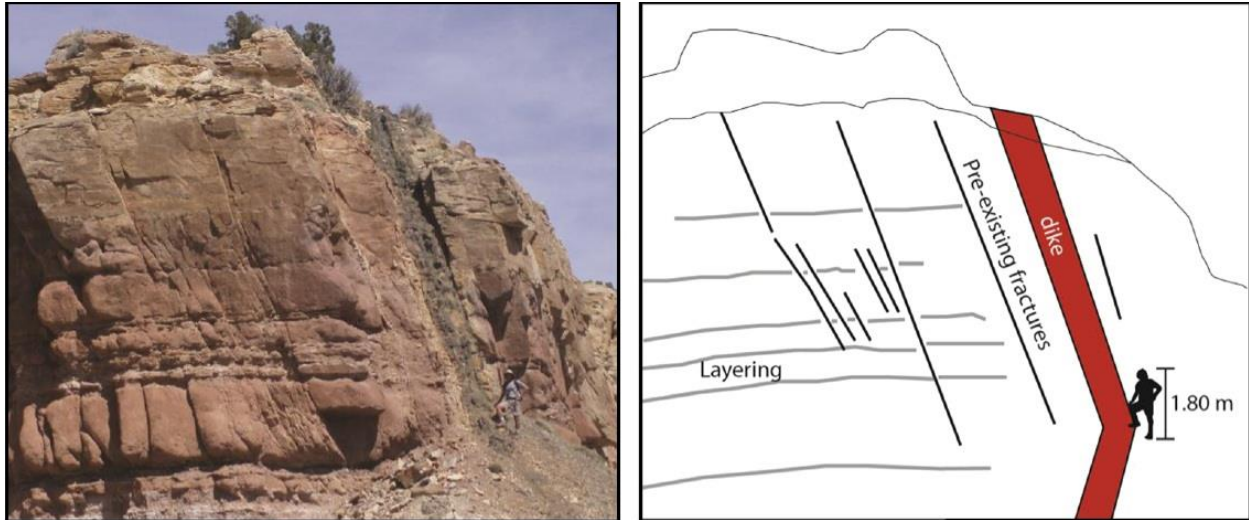


Figure 9. Exploitation of preexisting fractures in sedimentary strata by dark gray basaltic dike (from Le Corvec et al., 2013).

### ***Magma Ascent***

Viscosity, density, temperature, and stress variation all play a role in driving magma ascent. Vigneresse and Clemens (2000) report that viscosity differences of  $10^4 - 10^{20}$  Pascal seconds (Pa s) allow liquid magma to freely flow relative to solid host rock. Density contrasts also play a part in magma ascent. Because magma is hot liquid rock, it is less dense ( $\sim 0.3-0.4$  g/cm<sup>3</sup>) than surrounding host rock. This provides buoyancy and a small pressure gradient which drives magma toward areas of equal density and pressure (upward). Temperature differences ( $\sim 500^\circ\text{C}$  for felsic magmas, more for intermediate and mafic magmas) and the resulting thermal expansion aid in the density disparity between magma and host rock.

While viscosity, density, and temperature are all important in magma ascent, Vigneresse and Clemens (2000) show that stress is the most crucial property. The lithostatic load of host rock is seven times greater than the buoyancy-related stress of magma. Differential stress disparity is even greater: differential stress in extensional settings is 55 times greater than

buoyancy-related stress and 257 times greater in contractional settings. These stress differences lead to strain partitioning in the less viscous magma. As a result, magma is driven upward.

According to Petford et al. (1993), ascent velocity is affected by magma viscosity and dike width, as defined by the following equation:

$$V_{av} = \frac{g\Delta\rho w^2}{12\mu_m}$$

Where  $V_{av}$  is average velocity,  $g$  is gravitational acceleration,  $\Delta\rho$  is the density contrast between magma and host rock,  $w$  is the width of the dike, and  $\mu_m$  is the viscosity of magma. Several generalities can be made from this equation: The larger the density contrast between magma and host rock, the higher the ascent velocity; the wider the dike, the higher the ascent velocity; the higher the viscosity of the magma, the lower the ascent velocity. Calculations by Petford et al. (1993) show that granitic magma of high viscosity can ascend through continental crust at 30 km/month (~1 cm/s). This velocity should be even faster in less viscous intermediate magmas of the Henry Mountains, and provides constraints on total construction time of the intrusive sheet network on Mount Hillers' southern flank.

### ***Magma Emplacement***

Widespread observations show that magma intrudes along bedding planes and other bedding concordant features. Doming is another process involved in the emplacement of magma in the shallow crust. Johnson and Pollard (1973) and Pollard and Johnson (1973), reviewed earlier, suggested that a sill may evolve into a domed laccolith once lateral spreading reaches a certain radius relative to emplacement depth and leverage on the overburden is attained. While the findings of some recent studies are consistent with this mechanism of laccolith growth (e.g.

Cruden and McCaffrey, 2001; Cruden and Bungler, 2010), other studies suggest that this process is more complex and other factors may be important. Typical intrusion geometry (Figure 10) of laccoliths around the world have shown that the intrusions often have relatively flat roofs (Morgan et al., 2008; Rocchi et al., 2010). The bent overburden is often observed as steep, stair-like deformation (e.g. Morgan et al., 2008). Lateral growth stops once vertical growth begins (Horsman et al., 2010). These observations contradict the notion that laccolith growth is primarily controlled by a length-thickness ratio. While magma-overburden leverage probably factors into laccolithic doming, other elements are certainly at play. These may include wallrock lithology, where more rigid overburden may stunt sill evolution, and magma emplacement rate, where faster emplacement of pressurized magma may aid in sill to laccolith transition (Horsman et al., 2010).

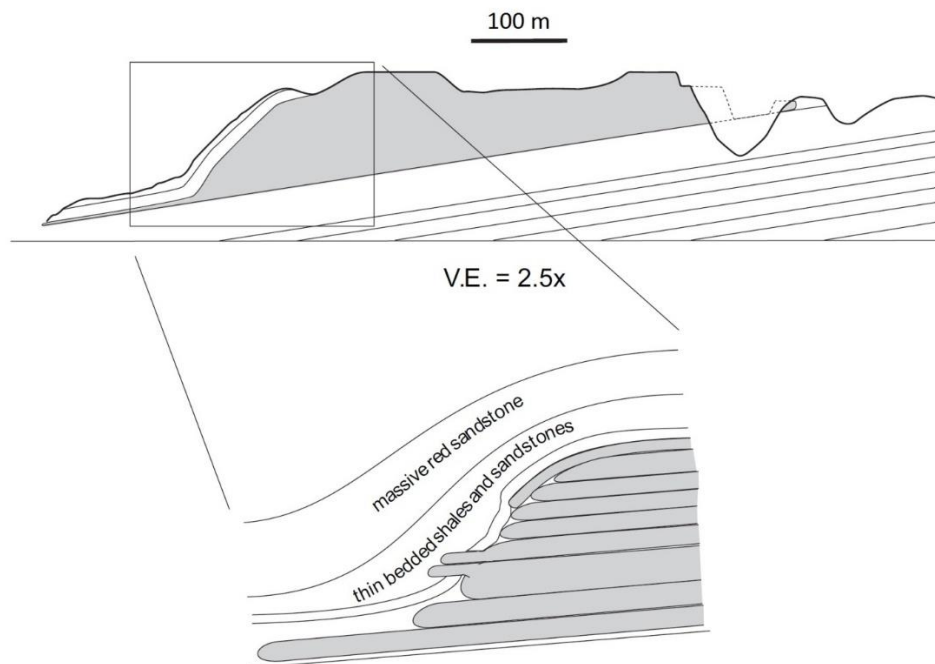


Figure 10. Cross section of Trachyte Mesa laccolith, eastern flank of Mount Hillers, Henry Mountains, illustrating flat roof and sharply bent overburden at intrusion margin (from Morgan et al., 2008). Vertical Exaggeration is 2.5x.

## *Dike/Sill Transition*

Field observations demonstrate that sills are often directly fed by dikes. The transition from vertical to lateral magma movement is likely governed by several factors, including buoyancy, stress fields, rheology, and host rock heterogeneity (Menand et al., 2011). Neutral buoyancy is the theoretical point in the crust when the density of ascending magma equals the density of the host rock. If neutral buoyancy controls the dike/sill transition, ascent is halted, and lateral emplacement commences. Vigneresse and Clemens (2000) make the argument that while this may indeed be a mechanism for transitioning mafic and some intermediate magmas, granitic magmas do not reach neutral buoyancy in the shallow crust (Figure 11). Only in very specific circumstances involving vesicular volcanic host rocks or unusually porous sandstones can granitic magmas theoretically reach neutral buoyancy. Also, the abundant mafic dikes exposed at Earth's surface show that even relatively high-density magmas can ascend past neutral buoyancy levels. The switch from dike ascent to sill emplacement must be explained some other way.

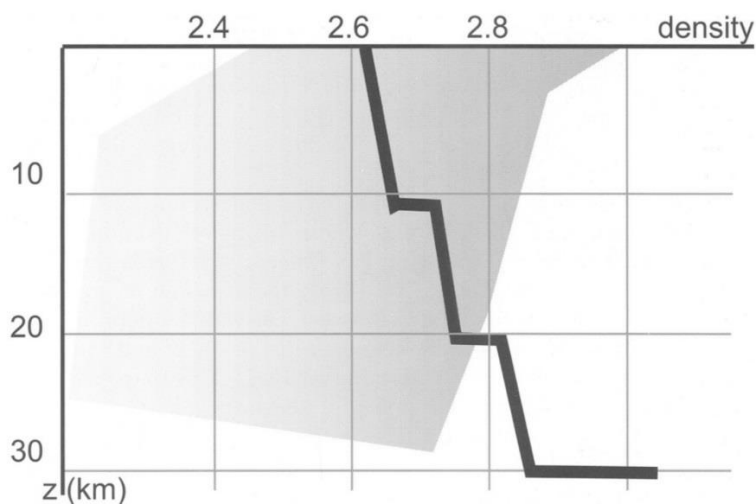


Figure 11. Diagram showing density versus depth through the crust. The solid black line represents bulk crustal density. Granitic magma densities are represented to the left in light grey, while gabbroic magma densities are to the right in dark grey. Note that granitic and intermediate magmas should never reach a point of neutral buoyancy in the crust (from Vigneresse and Clemens, 2000).

Stress fields aid in certain types of magma movement. Dike ascent dominates in extensional stress regimes (Petford et al., 1994), as vertical extension fractures readily form in these tectonic environments. In a contractional stress regime, dike ascent is limited since  $\sigma_1$  works to close the fractures that dikes utilize. If a change in the stress field (from extensional to contractional) occurred during magma ascent, arrest of dike ascent may take place and lateral sill emplacement may begin (Menand et al., 2011). However, the lack of regional deformation during the emplacement of the Henry Mountains intrusions suggests this mechanism was probably not a controlling factor in the dike/sill transitions of the study area.

Rheology contrast between the brittle and ductile crust may arrest dike ascent and promote sill emplacement (Parsons et al., 1992). Rheologically ductile zones magnify the local increase in horizontal least principal stress caused by vertical diking because within these zones, there is a partial relaxation of pre-existing deviatoric stress. Substantial diking may lead to significant modification in the stress conditions where the least principal stress locally rotates to vertical, promoting sill formation. Rheological behavior limits this mechanism to the brittle/ductile transition zone, so intrusions in the brittle, shallow crust are likely unaffected by this control.

Experimental work done by Kavanagh et al. (2006) suggests mechanical heterogeneity in the host rock may play an important role in the dike/sill transitions. In these experiments, dyed water and gelatin were used as magma and host rock analogues, respectively. Using stacked layers of gelatin of varying densities and rigidities, the authors injected the dyed water into the bottom of the experimental setup (Figure 12). Dikes ascended through less rigid layers, and upon encountering the lower contact of the stronger and more rigid upper layer, cessation of dike ascent led to horizontal sill emplacement. Results from this study suggest that mechanical

heterogeneity within the host rock, such as bedding in sedimentary strata, provides zones where dikes transition to sills more easily.

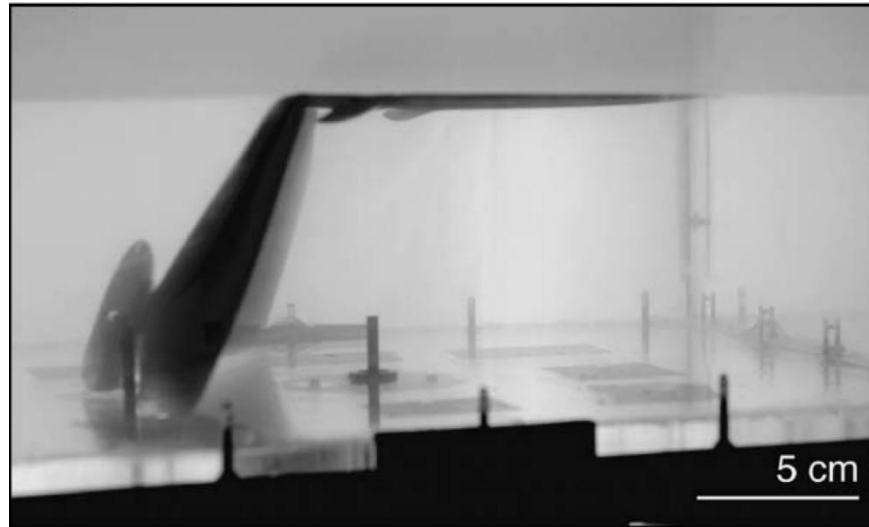


Figure 12. Experimental work showing dyed water (magma analogue) injected into layers of gelatin (host rock analogue). Layers of lower rigidity allowed vertical ascent, and lateral emplacement began at the lower contact of more rigid overburden (from Kavanagh et al., 2006).

## **Methods**

This section outlines how I tested the hypotheses stated in the introduction. Field work was used to test the *pulsed construction*, *magmatic flow characteristics*, and *host rock mechanical heterogeneity* hypotheses. Crystal size distribution, thin section petrography, and inductively coupled plasma mass spectrometry was used to test the *pulsed construction* hypothesis. Anisotropy of magnetic susceptibility was used to test the *magmatic flow characteristics* hypothesis. Below, each technique is explained in detail.

### **Field Work**

Igneous and sedimentary units were mapped in the field using high resolution aerial photography and a handheld GPS unit for accurate positioning. Field maps were later scanned and digitized using ArcGIS computer software. Sedimentary rock units were described and bedding measured. Igneous rocks were described, and any observable fabric measured. From 168 stations, 70 oriented igneous samples were collected for laboratory analysis. Sedimentary samples were collected from the four oldest units exposed in the field area: Triassic Moenkopi formation, and the White Rim, Organ Rock Tongue, and Cedar Mesa members of the Permian Cutler formation.

Cross-cutting igneous contacts observed in the field were distinguished by markedly different intrusion orientations and corresponding textural variation between the adjacent intrusive bodies. Textural distinctions were based primarily on field observations of different plagioclase phenocryst size and abundance.

Magmatic fabrics form in relation to the strain produced by magma flow. In the restricted spaces near the fingered tips of sheet intrusions, convergent flow dominates; as such, extension and flow direction share similar orientations (Paterson et al., 1998). When the magma cools and solidifies, aligned crystals are locked in place (Yoshinobu et al., 1998). These mineral alignment fabrics, when compared to unit geometry, can be interpreted as magmatic paleoflow indicators. For this study, field-measured magmatic fabrics, defined by aligned hornblende phenocrysts, were observed and measured in the field where possible. However, these fabrics are commonly weak and difficult to measure with confidence.

Field work can be used to test whether the mechanical properties of host rock played an important role in the intrusion of dikes and sills. The most current geologic evidence indicates the geometry of the CIB of Mount Hillers is laccolithic (Jackson and Pollard, 1988; Broda, 2014). When the original igneous body began doming, whether as a single injection of magma or through stacking of individual sheets, the overlying rock was bent and uplifted to make space for underlying magma. This deformation eventually caused radial fractures to form throughout the overburden (Jackson and Pollard, 1990). For this study, field work involved the observation and mapping of radial dikes around the southern flank of Mount Hillers, some extending out at least 1 km from the central intrusive body.

Observing the contacts between sills and sedimentary host rock may provide insight into emplacement mechanisms like the use of bedding planes, fluid-related brecciation of host rock, and intrusion inflation with consequent uplift of the overburden. Field observations may also show that mechanical heterogeneity in the host rock (like competence and rigidity contrasts between underlying and overlying layers) may have some control on the transition from dike ascent to sill emplacement, as demonstrated by Kavanagh et al. (2006).

## Crystal Size Distribution

Crystal size distribution (CSD) is a quantitative method to measure crystal populations in a sample and can shed light on magma crystallization histories of magmatic systems. CSD has been applied to studies of igneous rocks in the past (e.g. Cashman and Marsh, 1988; Higgins and Roberge, 2003; Mock et al., 2003), quantifying textural heterogeneities in single intrusive bodies and interpreting dynamic crystallization histories of their respective magmas. More recently, using CSD analysis on intrusions in the Gold Creek area on the eastern margin of Mount Hillers, Gwyn (2011) obtained two distinct plagioclase phenocryst populations and interpreted these to represent two separate pulses of magma in the area.

Marsh (1988) developed the theory behind CSDs and created the standard CSD curve to visualize the data. In a melt, crystals grow over time, producing a range of sizes in the cooled rock from relatively large (longest growth time) to relatively small (shortest growth time). The growth of these crystals in a melt is expressed in the following equation:

$$n = n_0 \exp\left(-\frac{L}{G\tau}\right)$$

where  $n$  is population density,  $n_0$  is the population density of nucleus-size crystals,  $L$  is crystal size,  $G$  is crystal growth rate, and  $\tau$  is residence time.

Analyzing crystal sizes yields a list of length, width, area, and orientation of the crystals, as well as the area occupied by the crystals. The normal distribution of CSD data is logarithmic, so grouping these data in logarithmic size intervals (bins) typically produces the clearest results. Plotting logarithmic population density [ $\ln(n)$ ] measured in the inverse of crystal size per unit volume versus crystal size in mm produces the CSD curve. Linear regression analysis on the

CSD curve produces measures of nucleation density (y-intercept) and the negative inverse of the product of growth rate and residence time (slope). If crystals nucleated and grew at a constant rate, the resulting CSD curve for that magma would be a straight line. Nonlinear CSD curves are the result of more complicated crystallization histories and may be the result of magma mixing (Higgins, 1996) or sequential cooling events at different depths (Armienti et al., 1994), or both.

Higgins (2000) summarizes the theory behind CSD, discusses issues with 2-d to 3-d data conversion, and presents the CSDCorrections computer software to conduct these calculations. Obtaining crystal sizes for CSD analysis requires measuring crystal faces on a planar surface (thin section, rock slab, etc.) Because crystals are not perfect three dimensional shapes (sphere, cube, pyramid, etc.), issues arise when converting data from 2-d to 3-d. According to Higgins (2000), the intersection probability effect states that large crystals are more likely to be seen on a 2-d plane than small crystals; the cut section effect states that variation in the cut orientation through one particular crystal will generate different crystal “sizes” on the plane. These issues are resolved mathematically using computer software developed by Higgins (2000).

For this study, igneous rock samples collected in the field were slabbed and scanned. The ImageJ computer program was used to analyze the digital images. This involved cleaning up the image margins, adjusting image threshold to create plagioclase-only and hornblende-only binary images, and finally analyzing the crystals for their size data. Care was taken to surpass the minimum crystal sections required for accurate crystal habit determination suggested by Morgan and Jerram (2006). These data were then corrected for 2-d/3-d effects using CSDCorrections, generating CSD curves for all slabbed samples. Hornblende phenocrysts of 9 samples and plagioclase phenocrysts of 17 samples were analyzed. Multiple CSDs in a single phenocryst type may suggest the involvement of multiple distinct magma batches in the

construction of the intrusive sheet network. The comparison of the CSDs between dikes and sills provides a quantitative check on the directly observable crystal sizes at outcrop and hand sample scale. This analysis also allows for quantitative comparison of rock textures across the field area.

### **Thin Section Petrography**

As field work allows for the observation of textural differences at outcrop and hand sample scale, thin section petrography allows for the examination of these textural differences at much higher resolution. Billets of twenty igneous samples and four sedimentary samples were cut in house and sent off to be made into polished thin sections. Of the twenty igneous thin sections, ten are from cross-cutting dikes and sills, and two were taken from a possible dike feeder/sill system. By comparing thin sections of dikes and sills, I can conduct a more thorough analysis of the mineralogical and textural variations seen in the rocks, which may signify distinct crystallization histories. The four sedimentary rock thin sections are from the Triassic Moenkopi formation, and the White Rim, Organ Rock Tongue, and Cedar Mesa members of the Permian Cutler formation. Studying the mineralogy and alteration of these sedimentary units may provide insight into the temperature history and metamorphic fluids present during igneous emplacement.

### **Geochemistry**

Whole-rock major and trace element geochemistry was conducted using inductively coupled plasma mass spectrometry (ICP-MS; Montaser, 1998) by Acme Analytical Laboratories. Major and trace element geochemistry data were plotted on geological maps to assess spatial

trends. Additionally, geochemical signatures were compared between distinct textures and intrusion types.

### **Anisotropy of Magnetic Susceptibility**

Anisotropy of magnetic susceptibility (AMS) analysis provides a quantitative measure of mineral alignment fabric within a sample. Because AMS is highly sensitive, it is especially useful when field fabrics are weak or otherwise difficult to measure. AMS analysis has been used in previous studies (e.g. Knight and Walker, 1988; Callot et al., 2001; Horsman et al., 2005; Saint Blanquat et al., 2006; Stevenson et al., 2007; Morgan et al., 2008) to interpret magma flow directions.

AMS fabric is idealized as an ellipsoid with long ( $K_1$ ), intermediate ( $K_2$ ), and short ( $K_3$ ) axes.  $K_1$  is considered the magnetic lineation, while  $K_3$  is the pole to the magnetic foliation (Rochette et al., 1992). Interpretation requires information about magnetic mineralogy. To test magnetic mineralogy, susceptibility versus temperature data were collected by Michael Petronis at New Mexico Highlands University. Samples from the field area have a magnetic signal dominated by magnetite (Figure 13). The AMS of igneous rocks in the Henry Mountains is mainly controlled by multi-domain magnetite grains (Horsman et al., 2005; Saint Blanquat et al., 2006), so the orientation of the ellipsoid should reflect the preferred orientation of magnetite grains in the rock.

Scalar parameters are calculated to describe the overall susceptibility, intensity, and shape of the AMS ellipsoid. Bulk Susceptibility ( $K_m$ ), also known as average susceptibility, is defined as:

$$K_m = \frac{K_1 + K_2 + K_3}{3}$$

and provides information on the abundance and variety of magnetic minerals in a given sample.

The degree of anisotropy ( $P_j$ ) is defined as:

$$P_j = \exp(2[(\eta_1 - \eta_b)^2 + (\eta_2 - \eta_b)^2 + (\eta_3 - \eta_b)^2]^{1/2})$$

where  $\eta_i = \ln K_i$  and  $\eta_b = \ln(\eta_1 * \eta_2 * \eta_3)^{1/3}$ .  $P_j$  is a calculation of the strength or intensity of the AMS ellipsoid and fabric, where higher values indicate stronger fabrics. The mean shape parameter ( $T$ ) is defined as:

$$T = [2 \frac{\ln(K_2/K_3)}{\ln(K_1/K_3)}] - 1$$

and calculates the overall shape of the AMS ellipsoid, where oblate ellipsoids have values ranging from 0 to 1, prolate ellipsoids have values ranging from 0 to -1, and perfect spheres have a value of 0.

AMS analysis was conducted on 70 igneous samples collected from the intrusive sheet complex on the southern margin of Mount Hillers. Oriented hand samples were cored in the laboratory using a 1" diameter drill press and the orientation of each individual core was determined. The AMS of 22-mm-long specimens cut from the oriented cores was then measured on an AGICO MFK1-A Kappabridge at East Carolina University. The SAFYR software program collected data, while the Anisoft program compiled the data for visualization purposes. These data were compared to their nearby intrusion boundary orientations in order to make general interpretations about how magma flowed in these bodies during ascent and emplacement.

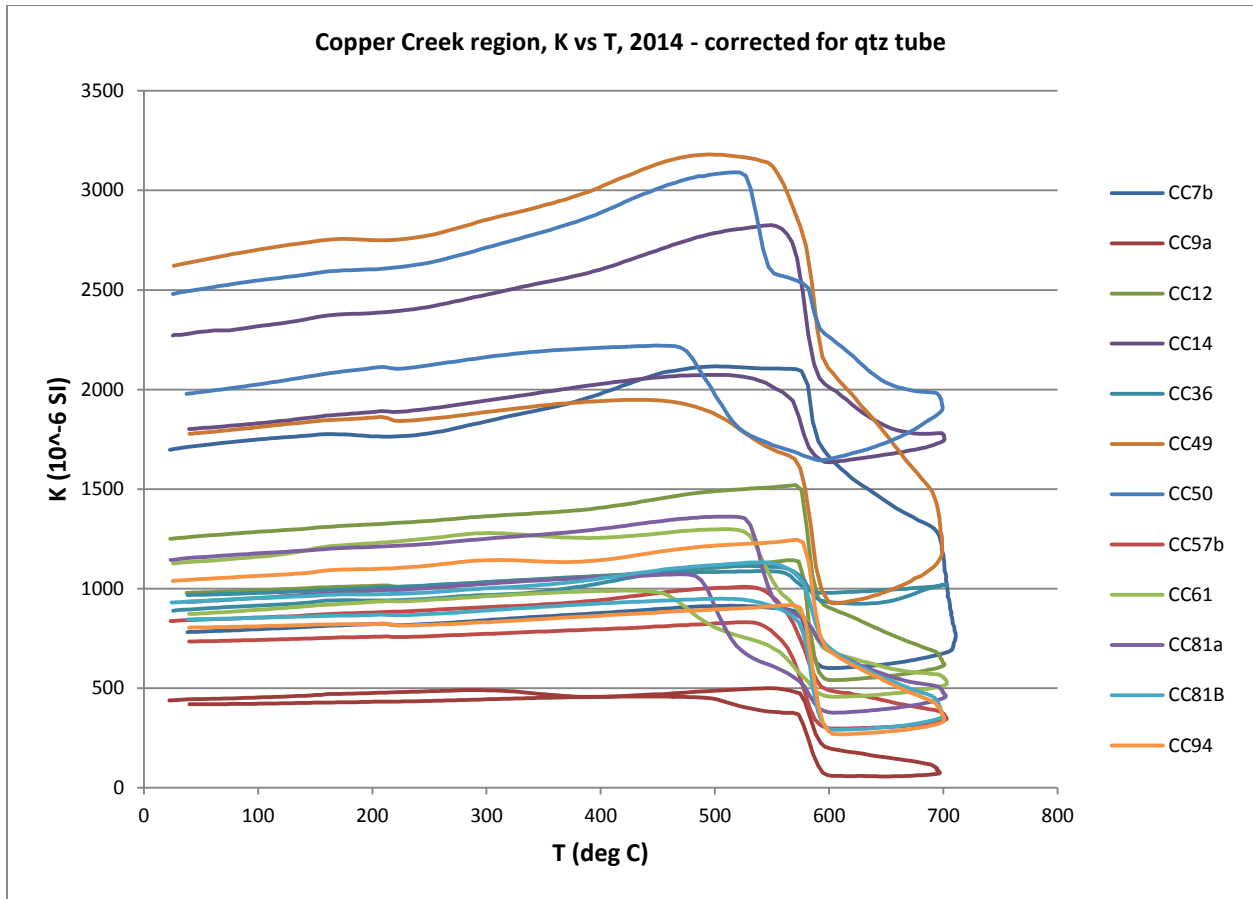


Figure 13. A plot of susceptibility vs. temperature for 12 samples from the intrusive sheet network on the southern flank of Mount Hillers. The susceptibilities of all samples is dominated by magnetite (Curie  $T \approx 570$  °C), as shown by the drop in susceptibility at 550-600 °C.

## **Results**

### **A Note on Textural Terms**

Textural terms developed during field work to describe rocks are used throughout the results and discussion sections. For this study, texture is defined largely by plagioclase phenocryst size. Three main textures are observed in the field: (1) fine-grained, defined by small, clustered plagioclase phenocrysts; (2) coarse-grained, defined by large, generally dispersed plagioclase phenocrysts; and (3) medium-grained, defined by plagioclase crystals of intermediate size.

### **Field Work**

A detailed geologic map of the southern margin of Mount Hillers was constructed using the field observations (Figure 14). Sedimentary units dip in concentric rings around the CIB (Figure 15); shallow dips ( $10-20^\circ$ ) are observed in the Cretaceous Dakota sandstone on the very outer margin of the field area, and abruptly steepen to almost vertical ( $75-90^\circ$ ) in the Jurassic Salt Wash member of the Morrison Formation. In the eastern region of the field area, shallow bedding persists farther toward the center of Mount Hillers, with outcrops of Jurassic Salt Wash gradually steepening from  $\sim 10^\circ$  to  $\sim 35^\circ$  over several 100 meters (Figure 16). Subvertical bedding persists through Jurassic and Triassic units to where the early Triassic Moenkopi formation bedding is measured at  $\sim 60-65^\circ$ . This moderately steep attitude shallows toward the center of the mountain, where Permian White Rim sandstone, Organ Rock Tongue shale, and Cedar Mesa sandstone generally dip between  $45-60^\circ$ . Three radial cross sections (Figure 17) show that the sedimentary rocks have been significantly deformed and domed about the

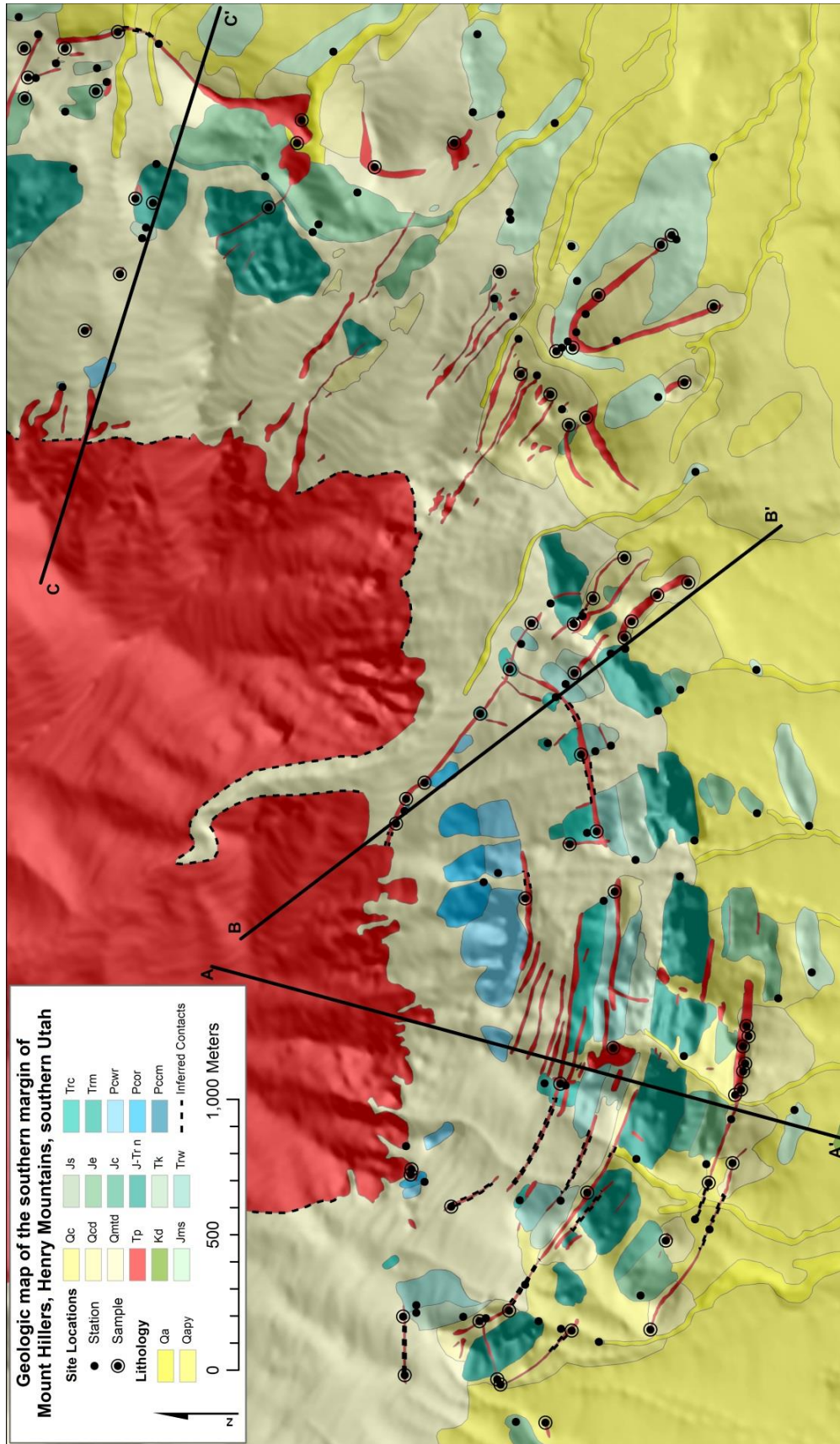


Figure 14. Geologic map of the southern margin of Mount Hillers. Station locations and stations where oriented samples were collected are noted. Cross section transects A-A', B-B', and C-C' are also marked.

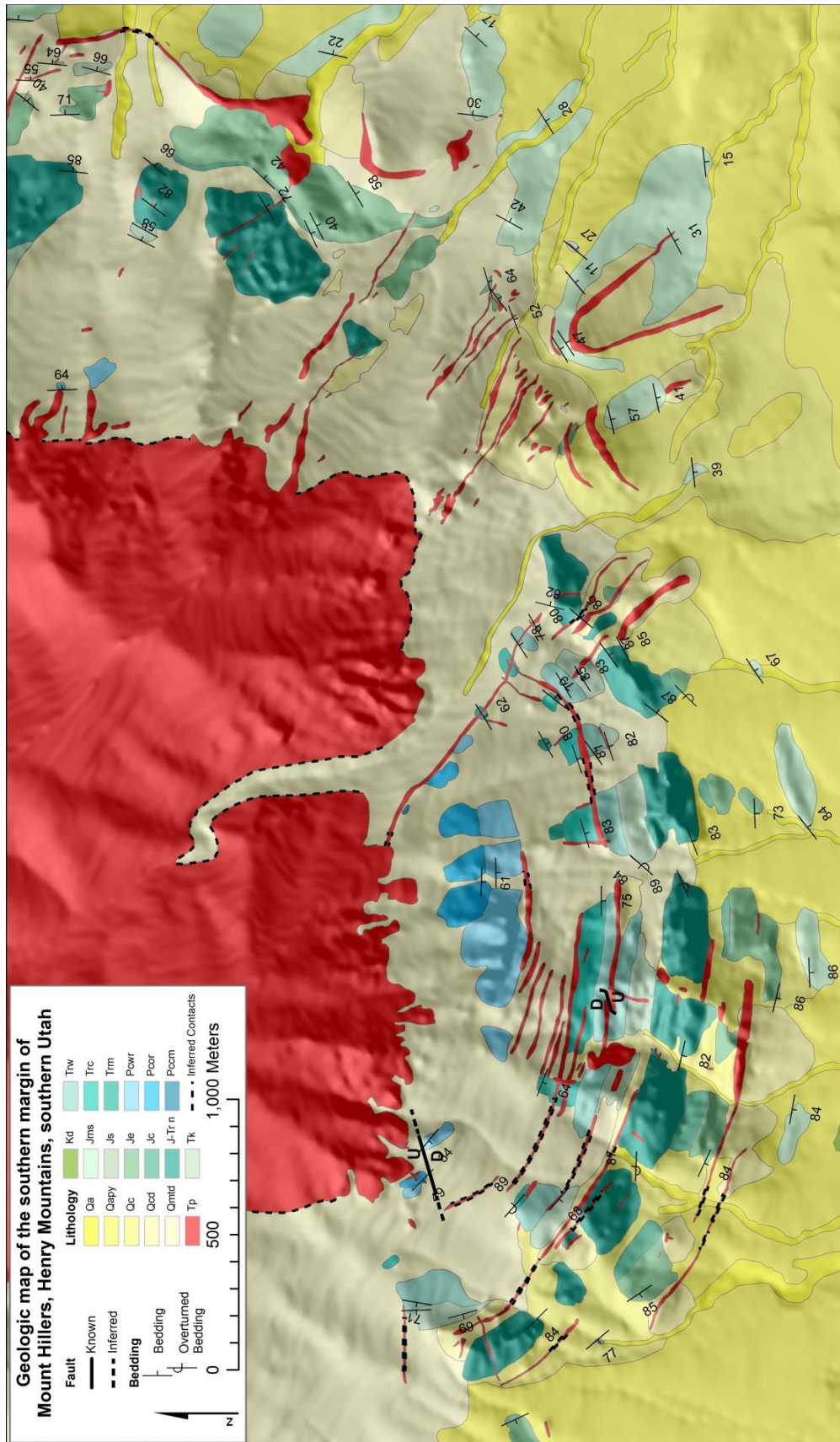
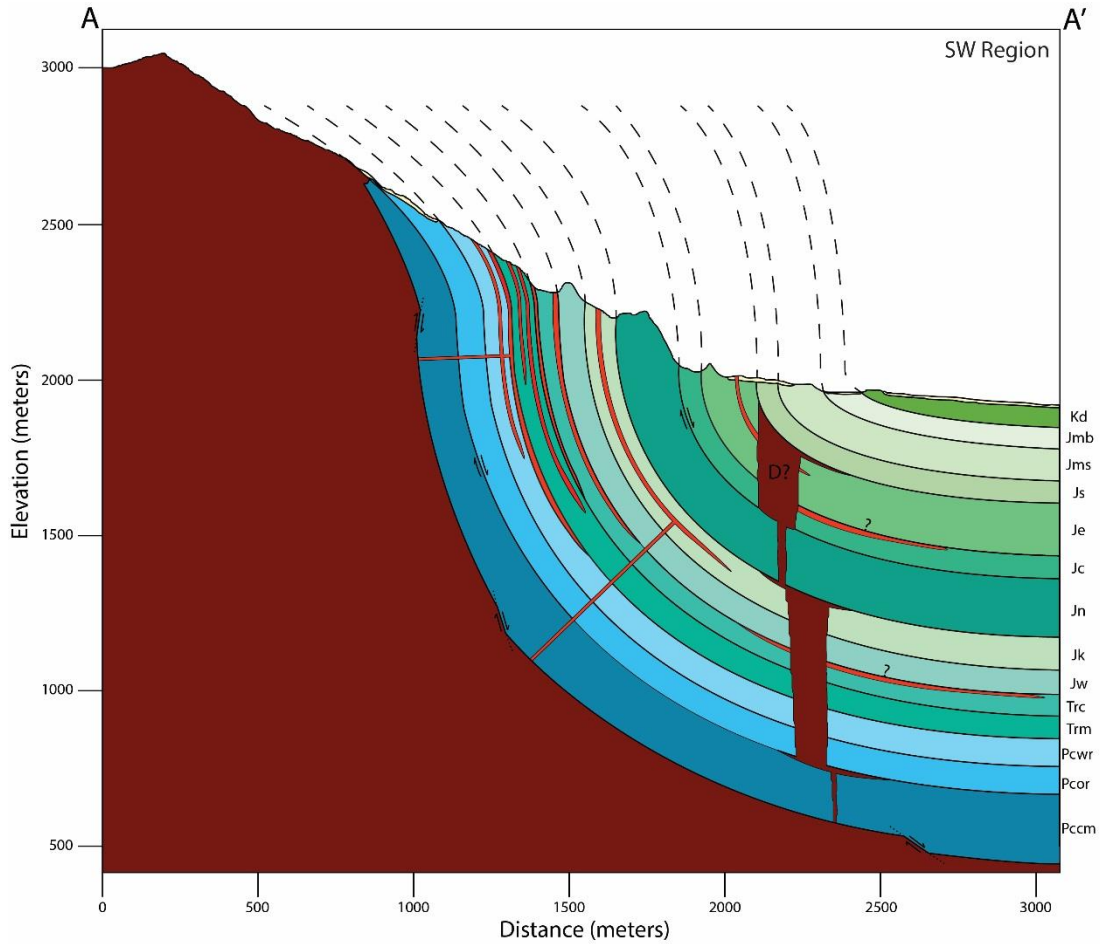


Figure 15. Geologic map of the southern margin of Mount Hillers with bedding measurements.



Figure 16. Picture of Jurassic Salt Wash outcrop, facing north. Bedding gradually steepens from east to west (right to left).



### Explanation

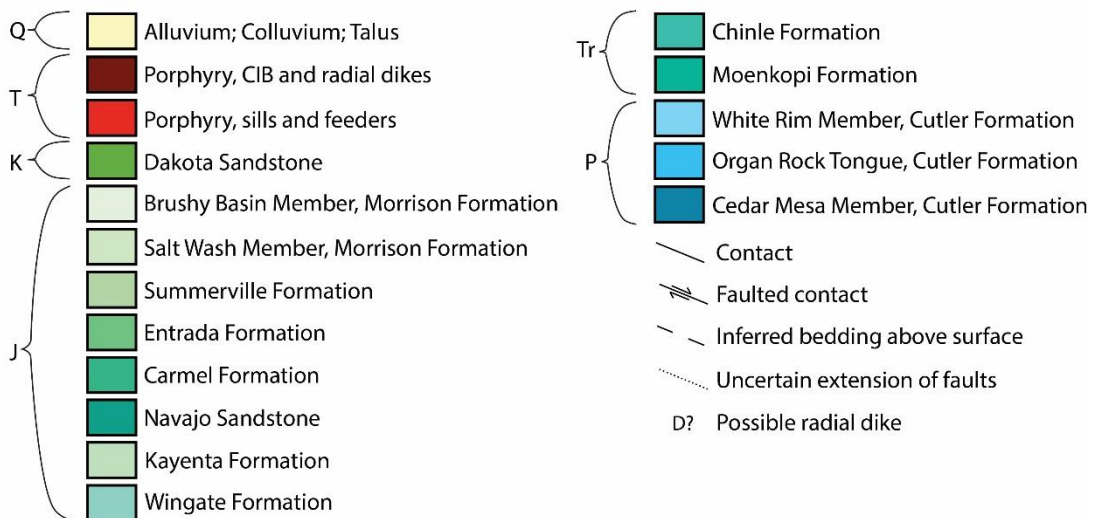
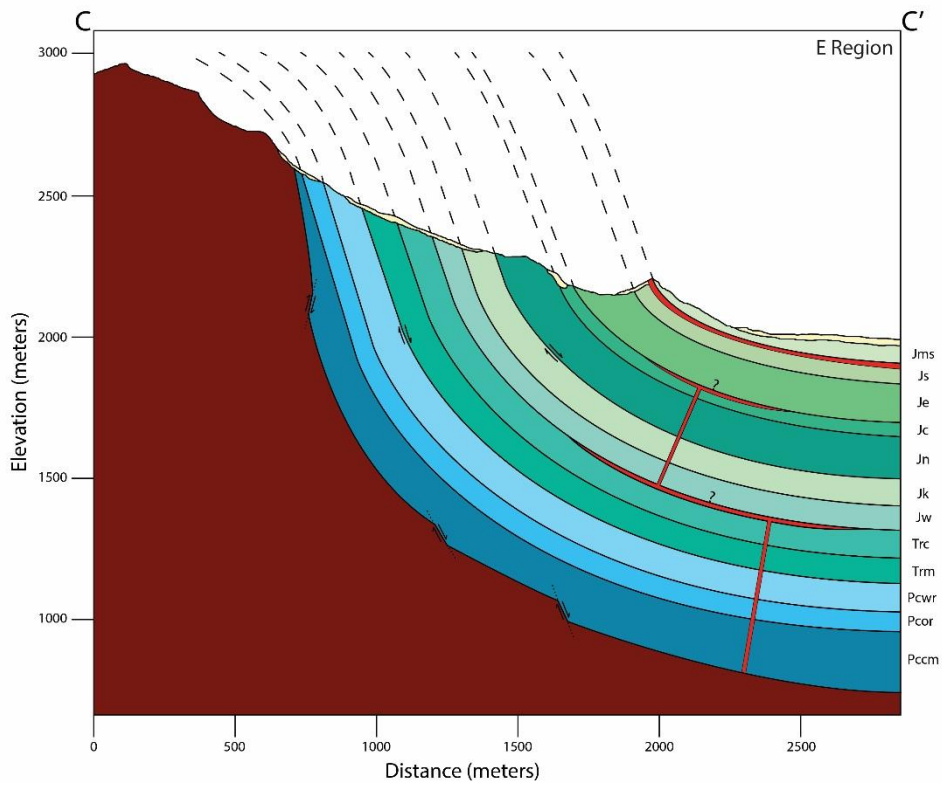
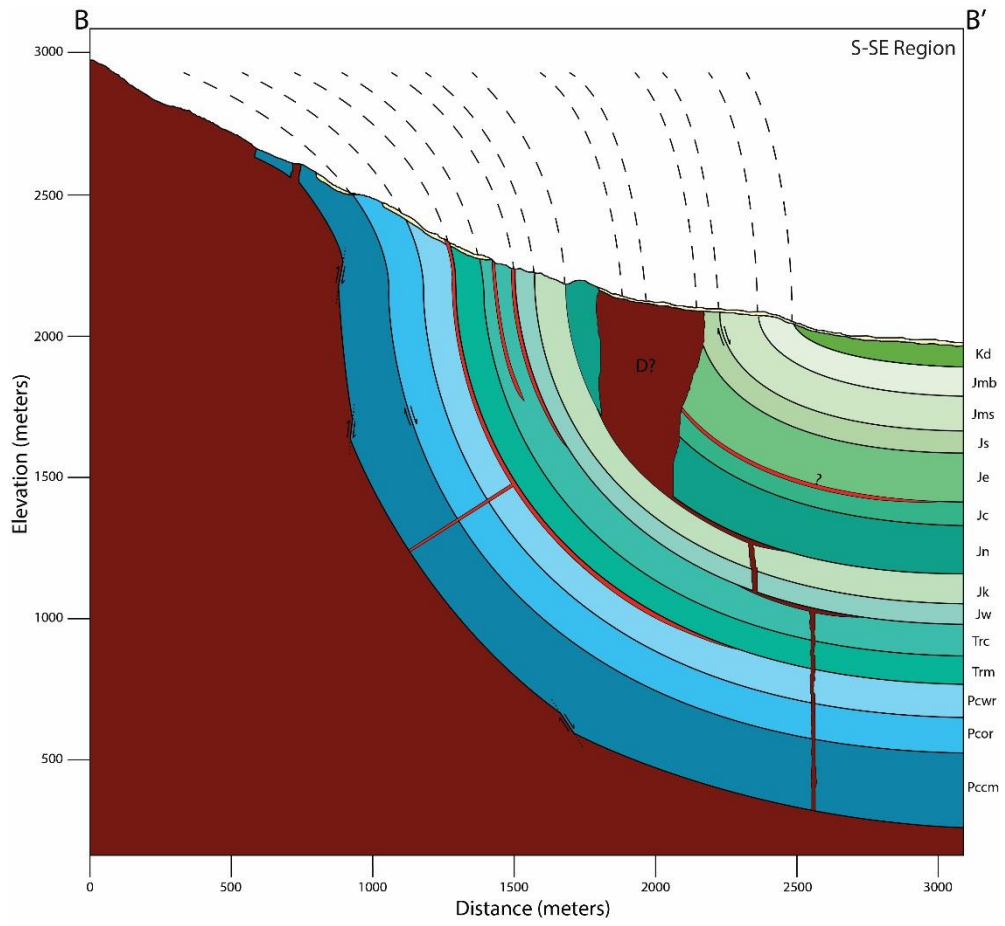


Figure 17. Cross sections (transects from Figure 13) of the southern margin of Mount Hillers with no vertical exaggeration. Note the double hinged geometry of the sedimentary strata. A-A' transect located in the SW region. B-B' transect located in the S-SE region. C-C' transect located in the E region. Faulted contacts included based on Jackson and Pollard (1990).



central intrusion.

At least 16 sills, intruding at various levels in the stratigraphic section, are observed. These intrusive sheets are bedding concordant, and strike concentrically around the central igneous intrusion. Sills are variably continuous around the margin of Mount Hillers, ranging from tens of meters to over 1000 m in length. Sill thickness is also variable, ranging from 1 to 20 m. Only the distal tips of these sills are exposed at the surface; their geometries are often discontinuous, with several 10- to 20-meter-long sections punctuated by areas of no exposed outcrop (Figure 18A). Textures of the sills of Mount Hillers are medium- to coarse-grained; plagioclase phenocrysts are generally 3-10 mm, sometimes up to ~15 mm, and hornblende phenocrysts are usually 1-6 mm, with the rare prism reaching 10 mm. Matrix is always aphanitic and appears in shades of dark grey to light grey depending on the outcrop. Phenocryst abundances in sills range between 35 and 50%.

Numerous dikes intrude the host rock on the southern flank of Mount Hillers. These dikes are generally oriented radially around the center of the CIB, and their continuous exposures range from tens of meters to over 1000 m. Dike thickness varies from 2 to 15 m, but most are thinner than 10 m. Dikes often crop out similar to sills, with staggered exposures. In the southeast region of the field area, dikes crop out in a pseudo-swarm (Figure 18B). Dike textures are fine- to medium-grained. Plagioclase phenocrysts are 1-5 mm, and hornblende phenocrysts are 1-3 mm, sometimes up to 5 mm. Matrix is aphanitic and generally medium grey, and phenocryst abundance is approximately 50%.

Nine clear instances of cross-cutting relationships in the intrusive sheet network were found in the field. In all these cases, a younger, fine-grained dike cross-cuts an older, coarse-

grained sill (Figure 19A-D). A tenth cross-cutting contact is observable from aerial photography (approximate UTM: zone 12N 526599E, 4190290N) but is inaccessible without rock-climbing gear. Here too the dike appears to cross-cut the sill, however confirmation would require direct field observation. These cross-cutting relationships, together with coarse-grained igneous inclusions (Figure 19E-F) observed within fine-grained igneous float, indicate two distinct relative ages of magma.

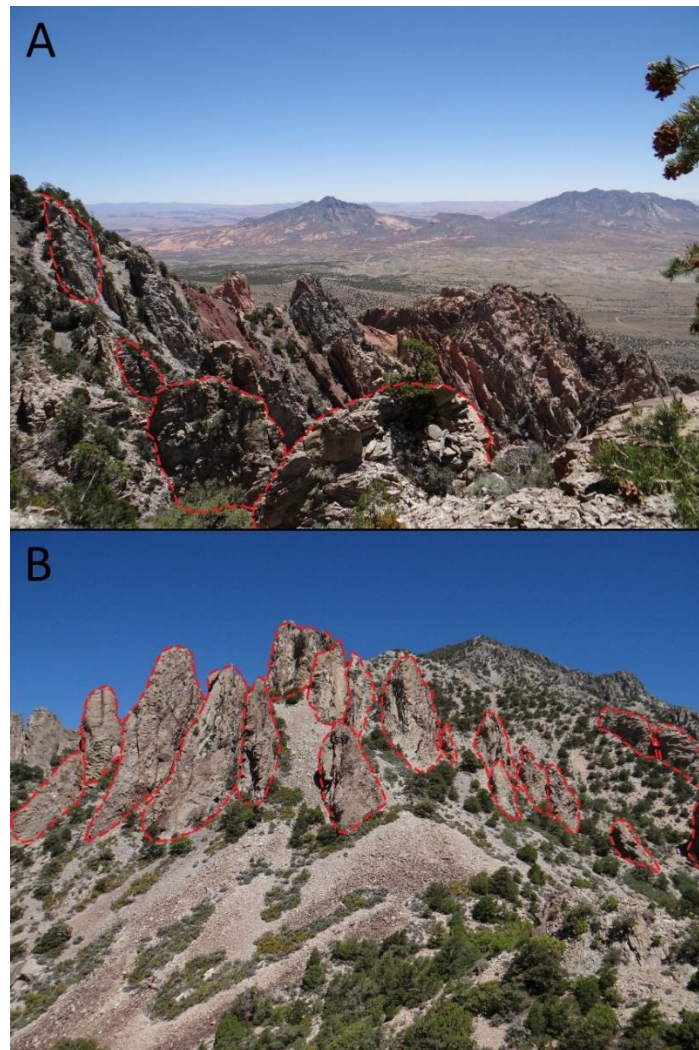


Figure 18. Pictures of intrusion geometries. (A) Bedding-concordant sill, with 10+ meter segments separated by areas with no igneous outcrop. Mount Holmes (left) and Mount Ellsworth (right) in the background. (B) Dike pseudo-swarm displaying discontinuous outcrop pattern common in the field area. Mount Hillers sister peak in the background.

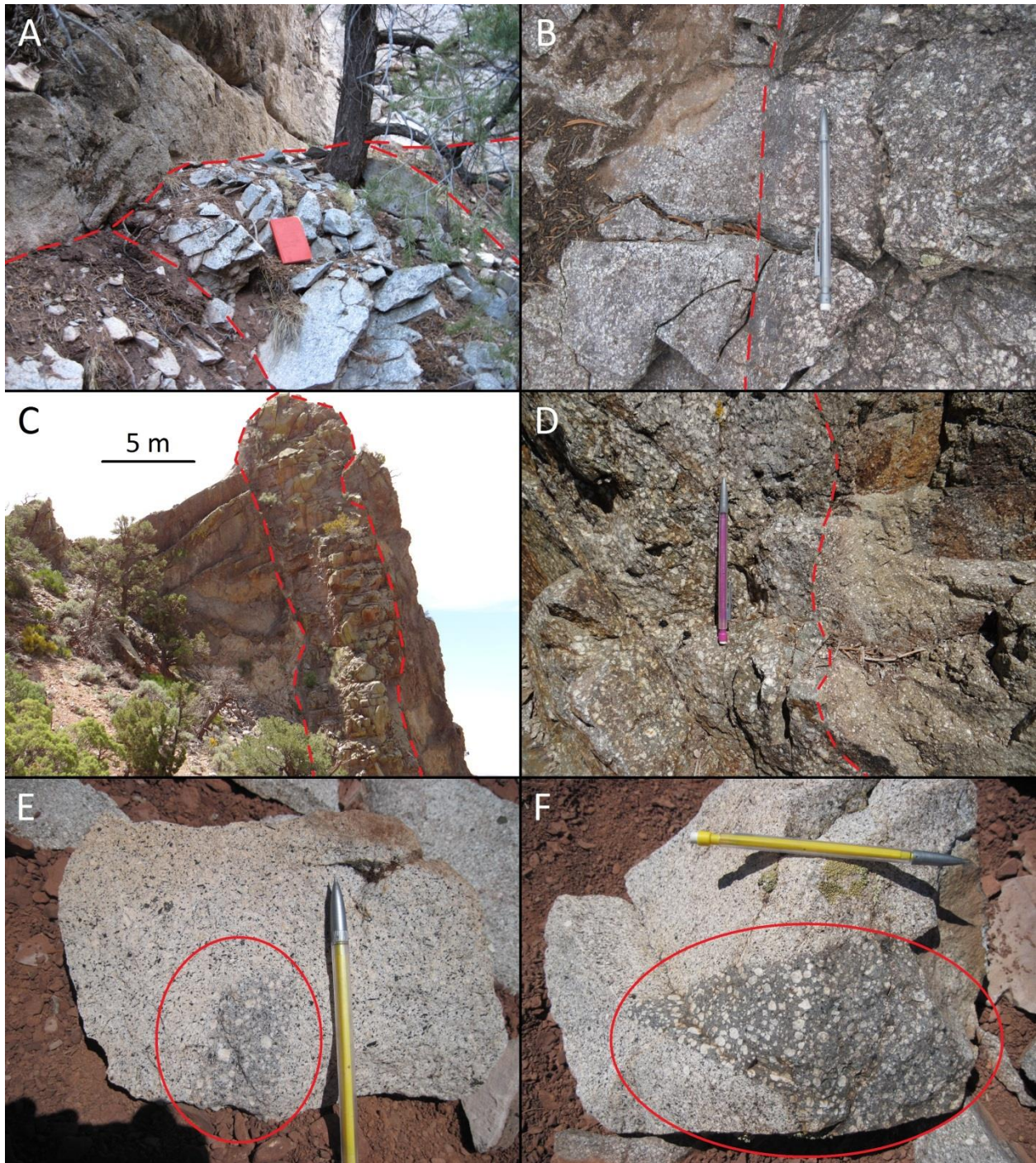


Figure 19. Pictures illustrating the relative ages of dikes and sills. Relevant features are marked or outlined. (A) Light-colored, coarse-grained sill terminating against a dark-colored, fine-grained dike, outcrop scale. Field book for scale. (B) Fine-grained dike (left) cross-cutting a coarse-grained sill (right), with a sheared contact. Pencil for scale. (C) Large, fine-grained dike subvertically cross-cutting a coarse-grained sill. (D) Cross-cutting contact between a fine-grained dike (right) and a coarse-grained sill (left). Pencil for scale. (E & F) Fine-grained dike float with coarse-grained igneous inclusions. Pencils for scale.

The preferred orientations of hornblende phenocrysts for sills and dikes were plotted on three equal-angle lower hemisphere stereographic projections based on region (Figure 20). Jackson and Pollard (1988) proposed subhorizontal sill emplacement prior to the doming and bending of the sedimentary host rock; therefore, data gathered from sills were rotated around the strike of nearby bedding to paleo-horizontal. Except for two stations in the S-SE region, rotated field fabrics are subhorizontal and trend radially. According to Jackson and Pollard (1988), radial dikes cut through the overburden during the final stages of central intrusion growth, so dike fabrics were not rotated with respect to bedding attitude. Fabrics measured from dikes range from subhorizontal to subvertical, with trends broadly in alignment with the general orientation of dikes in their respective regions.

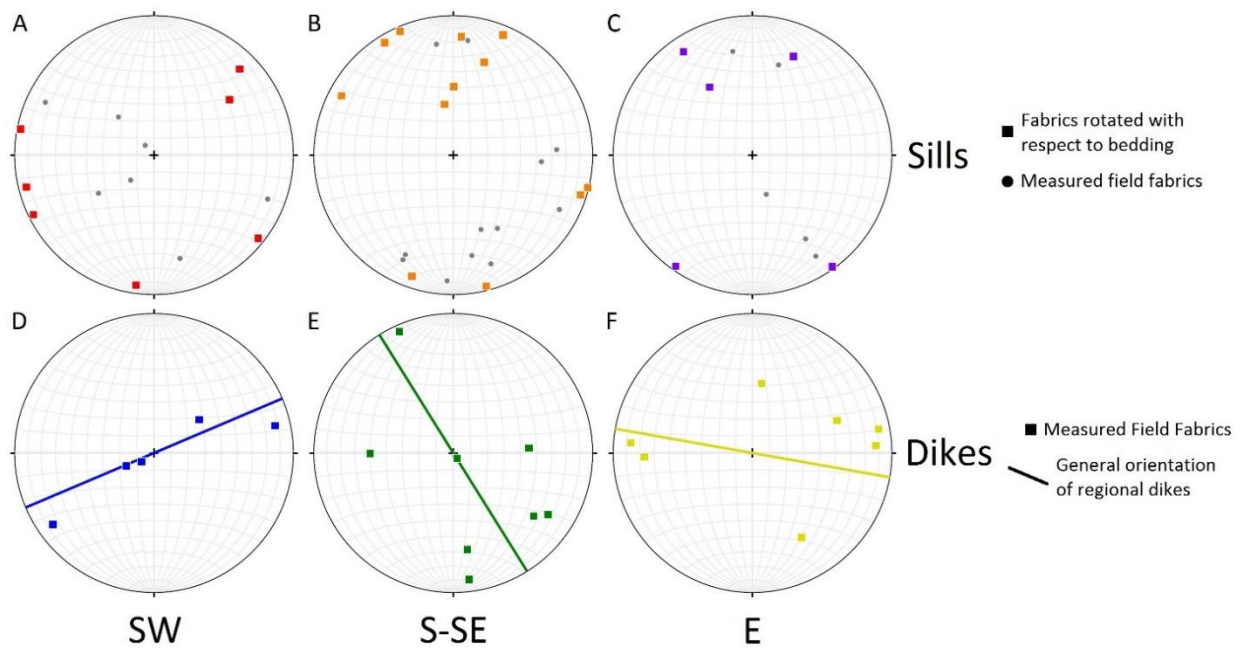


Figure 20. Equal angle lower hemisphere stereographic projections of long axis orientations of elongate hornblende phenocrysts from sills (A, B, C) and dikes (D, E, F) in the three regions (SW, S-SE, E) of the study area. Grey dots represent measured field fabric orientations, colored squares represent fabrics rotated around the strike of bedding to paleo-horizontal, and colored lines represent the general orientation of regional dikes.

At station CC9, the lower contact of the sill is stepped (Figure 21). These steps are fairly regular, with the long axes subparallel and spaced from 10 to 20 cm apart. A veneer of Chinle

formation shale covers the face of this intrusion contact. The long axes of these steps are typically perpendicular to flow (Horsman, personal communication, 2012), so magma probably flowed in a similar way in this particular intrusion.

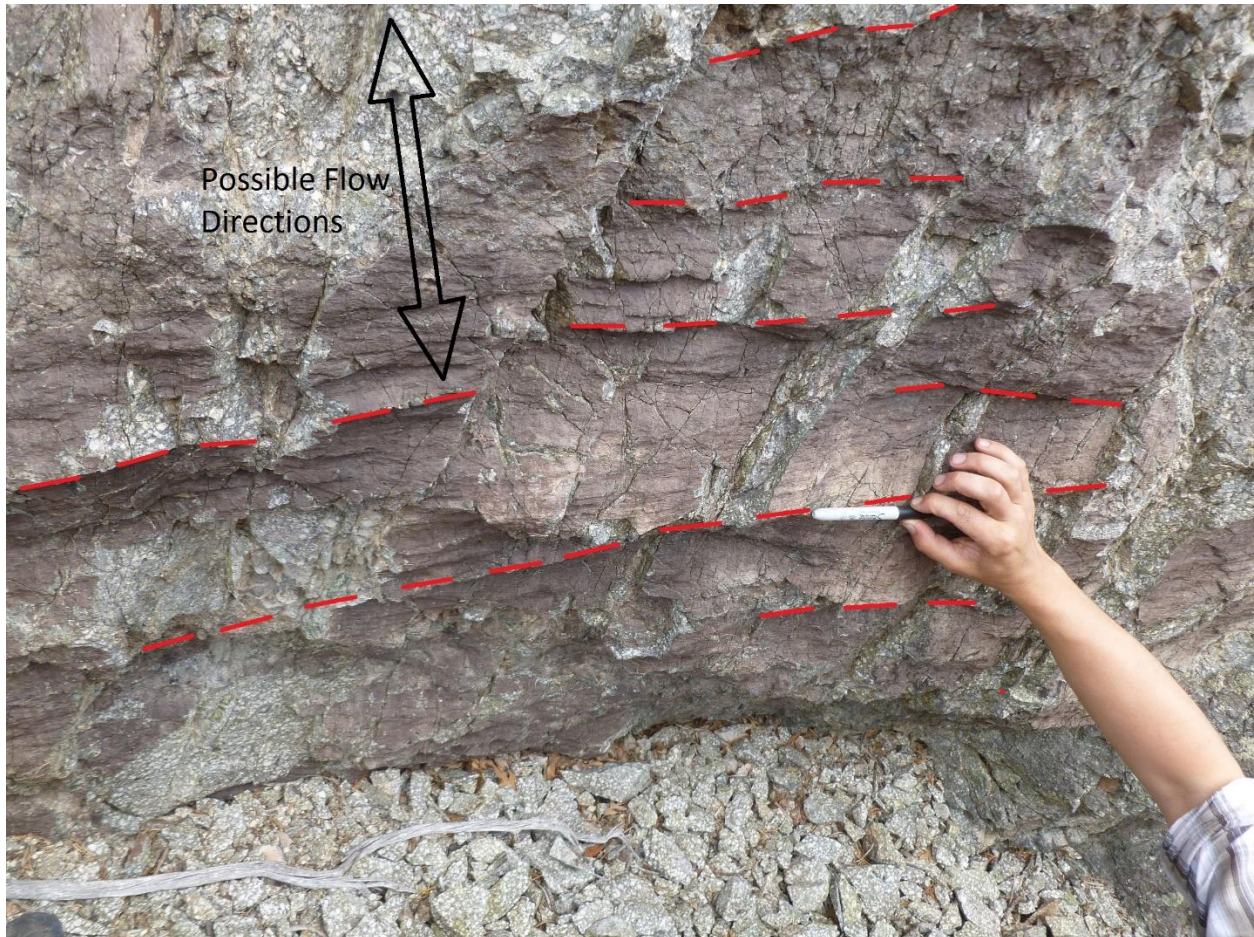


Figure 21. Photograph of stepped intrusive margin, individual step edges outlined in red. Possible flow directions indicated by arrow. Pen for scale.

Dikes in the study area consistently outcrop radially around the central igneous intrusion of Mount Hillers (Figure 14), with three general orientations: (1) In the southwest region, dikes trend generally NE-SW; (2) In the south-southeast region, dikes trend generally NW-SE; and (3) In the east region, dikes trend generally WNW-ESE. While dike outcrops are common, they are often discontinuous (e.g. Figure 18), and outcrops of the CIB are rare and difficult to accurately

identify. Consequently, there are no direct observations of dike contacts with the central laccolithic intrusion. However, indirect observations using aerial photography show several ridges (observed in the field to be dikes) which seem to extend out from the CIB.

Direct observations of early dikes that fed the sills of the study area are rare. While most of these dikes are probably buried, a few are exposed on Mount Hillers. In the Gold Creek region of Mount Hillers (just north of the eastern region of the study area), a tilted sill and its feeder dike intrude Entrada formation sandstone (Figure 22A). In the southwest region of the field area, a possible feeder dike is exposed in the upper portion of a Navajo formation hogback (Figure 22B). While these exposures are relatively rare, their existence suggests that at least some portion of magma involved with sill emplacement reached the shallow crust through subvertical dikes.

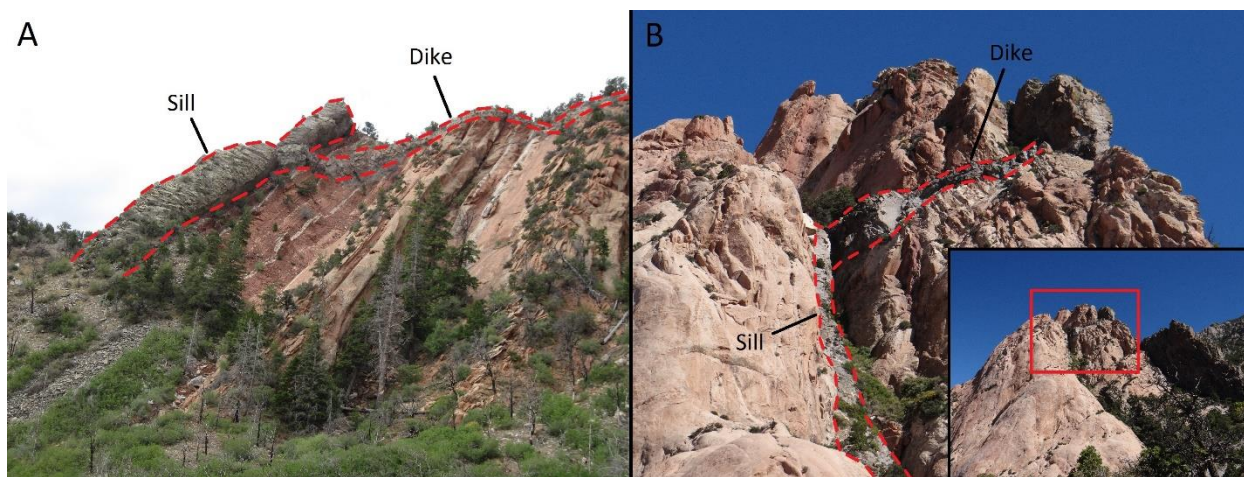


Figure 22. Photographs of possible feeder dikes on Mount Hillers. Features outlined and labeled. (A) Sill intruding the contact between Entrada and Summerville (now eroded) formations in the Gold Creek region. Feeder dike shown capping the sedimentary exposure. (B) Feeder dike and sill intruding the Navajo formation sandstone in the southwest region of the study area. Inset shows the location of these intrusions within the Navajo outcrop.

Sills are commonly observed to intrude along bedding planes throughout the field area. These contacts exist between two different sedimentary units and within single units. Observed at these contacts occasionally is fluidized brecciation (Figure 23). This slurry of igneous and

sedimentary fragments indicates that magma was able to weaken and break apart the host rock to make space for itself.



Figure 23. Fluidized breccia of maroon Chinle formation shale and porphyry fragments, outlined in red. Pencil for scale.

Approximate thickness measurements were made on twelve sills in the study area (Appendix A). Six sills intruded competent sedimentary host rock (sandstone-sandstone contact), and six intruded at least partially incompetent host rock (shale-shale or sandstone-shale contact). Sills intruding totally competent host rock range in thickness from 1 to 10 meters, with an average thickness of 6.2 meters. Sills intruding incompetent host rock range in thickness from 8 to 18 meters, with an average thickness of 12 meters. These observations are consistent throughout the field area; sills intruding at least partially incompetent host rock are regularly thicker than sills intruding competent host rock, and this variation is observable even over a relatively small area (Figure 24).



Figure 24. Photograph from the southeastern region, looking north. Dark grey sills (Td, outlined in red) of varying thickness observed in a relatively small area. West sill (left) is ~3-5 meters thick, and intrudes rigid, competent Navajo sandstone (J-Tr n). East sill (right) is ~10 meters thick, and intrudes the contact between competent Entrada sandstone (Je) and overlying incompetent Summerville shale (Js, now eroded away).

## Crystal Size Distribution

CSD image processing produces binary images of scanned slabs (Figure 25) that accentuate the textural differences observed in hand samples. Textures (fine-grained, medium-grained, and coarse-grained) were defined based on field descriptions of samples. Plots of CSD data (Appendix B) provide insight into the magma crystallization histories. CSD curves of hornblende phenocrysts are similar across textures (Figure 26). The curves exhibit a broadly consistent slope, with the exception of a shallow segment at smaller crystal sizes. Overall, crystals sizes are similar, ranging in most samples from <1 to 3.2 mm. Hornblende phenocrysts do not exceed 3.2 mm in samples collected from sills.

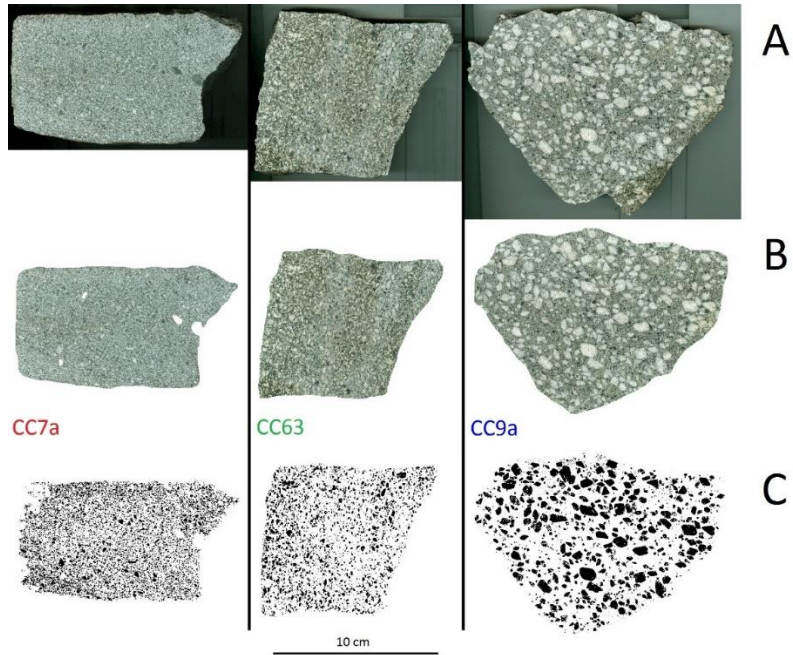


Figure 25. Pictures of CSD samples at different stages of processing. (A) Fine- (left), medium- (middle), and coarse-grained (right) samples are slabbed and scanned. (B) ImageJ is used to prepare the image for analysis, which includes removing the background from the scanner hood and any weathered segment of the slab, and deleting any xenoliths which would disrupt hornblende CSD results. (C) Threshold is adjusted to produce a binary image, with black polygons representing the crystals of interest (in this case, plagioclase phenocrysts).

### Crystal Size Distributions, Hornblende Phenocrysts

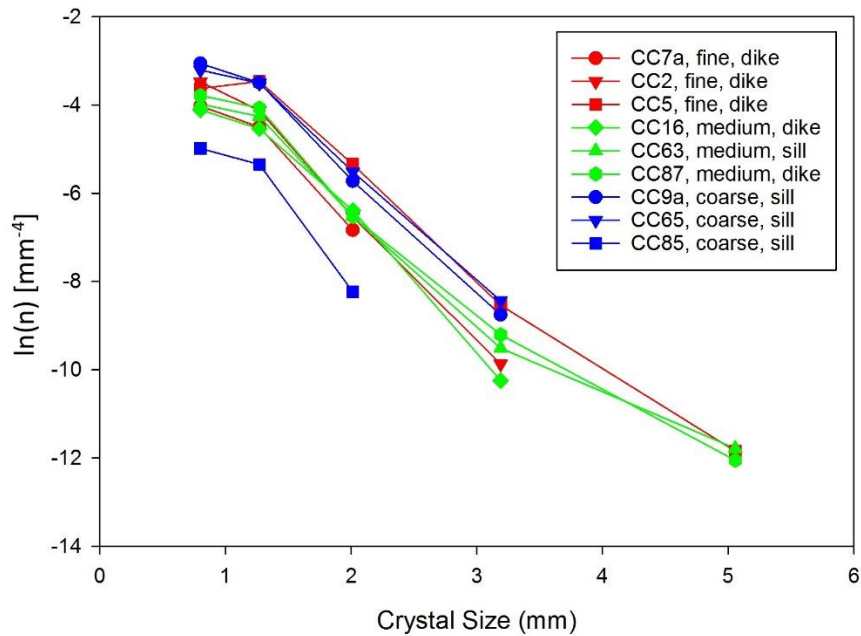


Figure 26. Crystal size distributions for hornblende phenocrysts in fine-, medium-, and coarse-grained samples.

Two distinct CSDs of plagioclase phenocrysts exist (Figure 27), based on texture and intrusion type. CSD curves of coarse-grained samples, all collected from sills, have shallow slopes and a slight concave up shape. Size range is greatest in these samples, some containing phenocrysts greater than 20 mm. CSDs of fine-grained samples were all collected from dikes, and have the steepest slopes. Maximum crystal size is smallest in these samples, with all but one sample peaking at 5 mm (the one sample peaks at 8 mm). Medium-grained samples, taken from three dikes and two sills, have slopes of intermediate steepness. Four of the five samples show a maximum crystal size of 8 mm, with the fifth reaching 5 mm. When compared, the CSDs of the medium-grained samples are more similar to the fine-grained samples than to the coarse-grained samples.

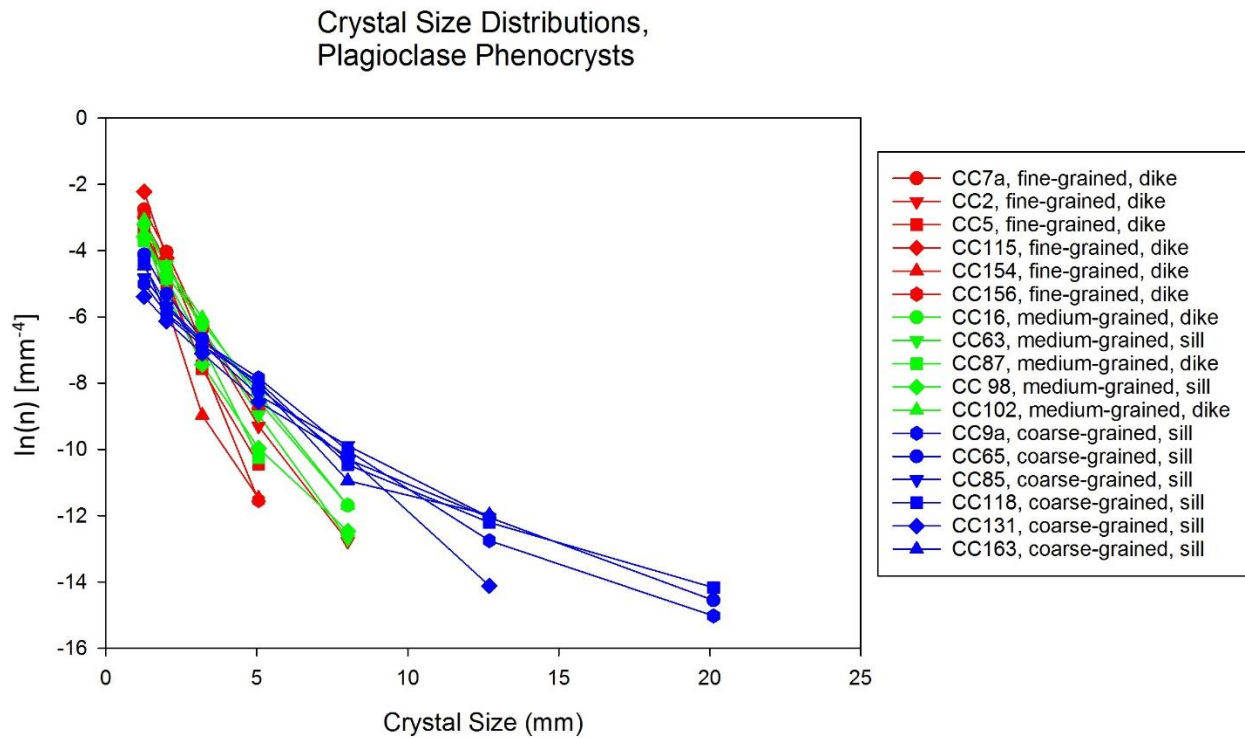


Figure 27. Crystal size distributions for plagioclase phenocrysts in fine-, medium-, and coarse-grained samples.

Performing linear regression analysis on all plagioclase CSDs provided the nucleation density and characteristic length of crystals for each sample. Nucleation density is the number of individual sites in a sample at which crystals form and is defined by the y-intercept. Characteristic length is the average size of all crystals, assuming they formed in a steady state system, and is defined by the product of growth rate and residence time, which is obtained by the negative inverse of the slope. A plot of these data against each other (Figure 28) further illustrates the differences in crystallization these rocks underwent. All coarse-grained sills have the highest characteristic lengths and lowest nucleation densities of the analyzed samples. The fine-grained dikes generally have some of the lowest characteristic lengths and highest nucleation densities of the analyzed samples. The medium-grained dikes and sills have characteristic CSDs intermediate between the coarse-grained and fine-grained samples, but skew closer to the fine-grained samples.

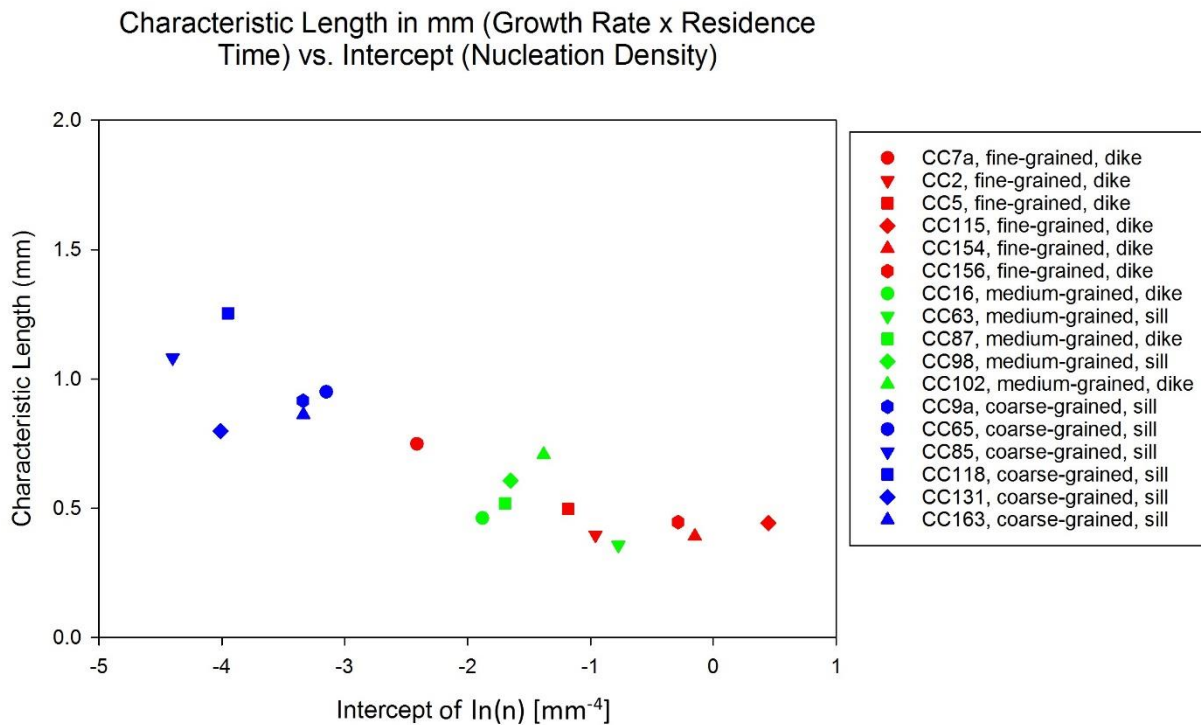


Figure 28. Characteristic length vs. intercept of plagioclase crystals in all analyzed samples.

## Thin Section Petrography

Texture analyses on thin sections of cross-cutting sill/dike groups support the observations seen at outcrops and in hand-samples (Figure 29). Plagioclase phenocrysts in coarse-grained sills are equidimensional to elongate prisms, ranging from ~1 to 12 mm, averaging ~5.5 mm. Hornblende phenocrysts are usually elongate prisms or laths, and range from 300 microns to 4 mm, averaging ~1 mm. Oxides, mainly magnetite, make up the remainder of phenocrysts; these crystals are generally equidimensional and much smaller, ranging up to ~300 microns. There are fewer phenocrysts in coarse-grained sills than in fine-grained dikes. Matrix color varies by sample, from light grey to dark grey-brown. Matrix crystals range up to ~100 microns, most being between 10 and 50 microns. Trace minerals in the sills and dikes include apatite, zircon, calcite, quartz, epidote, and clinopyroxene.

Fine-grained dikes contain phenocrysts of plagioclase, hornblende, and FeTi oxides, and these minerals share the same crystal habits as phenocrysts in coarse-grained rocks. Plagioclase phenocrysts range from 300 microns to rarely 5 mm, most averaging between 1 to 2 mm. Hornblende phenocrysts range from 300 microns to 4 mm, averaging ~800 microns. FeTi oxides range up to ~300 microns. Phenocrysts are much more numerous in fine-grained samples than coarse-grained samples. Matrix color is variable, from light-medium grey to dark greyish brown. Matrix crystals range up to ~300 microns, most being between 10 and 50 microns. With comparable hornblende phenocryst sizes and very similar FeTi oxide and matrix crystal sizes, coarse-grained and fine-grained rocks in the study area are distinguished exclusively by plagioclase phenocryst sizes; coarse-grained rocks have larger plagioclase phenocrysts than their fine-grained counterparts. It should be noted that when samples have an average plagioclase size

of ~2 mm and notably less clustered phenocrysts, the rock is considered medium-grained for the purposes of this study.

One sample, CC94, was collected from what is interpreted as the CIB. The texture of this sample is very similar to that of the fine-grained dike samples (Figure 30). Plagioclase phenocrysts range from 300 microns to 2.5 mm, averaging ~1.7 mm. Hornblende phenocrysts range from 300 microns to 2 mm, averaging ~700 microns. FeTi oxides range up to ~300 microns. Phenocrysts are very abundant. Matrix color is dark-greyish brown, and matrix crystals are mostly between 10 and 50 microns.

Samples CC57a and CC57b are from a dike/sill system in the eastern region of the field area. No notable grain-size difference or cross-cutting contact was observed between these two intrusive sheets. Instead, both were medium-grained with no sharp contact between them. Two thin sections, one from each intrusion, are compared in Figure 31. Plagioclase phenocrysts are comparable in size (averaging ~1.5 to 2.5 mm), both rocks are rich in hornblende, and matrix colors are similar.

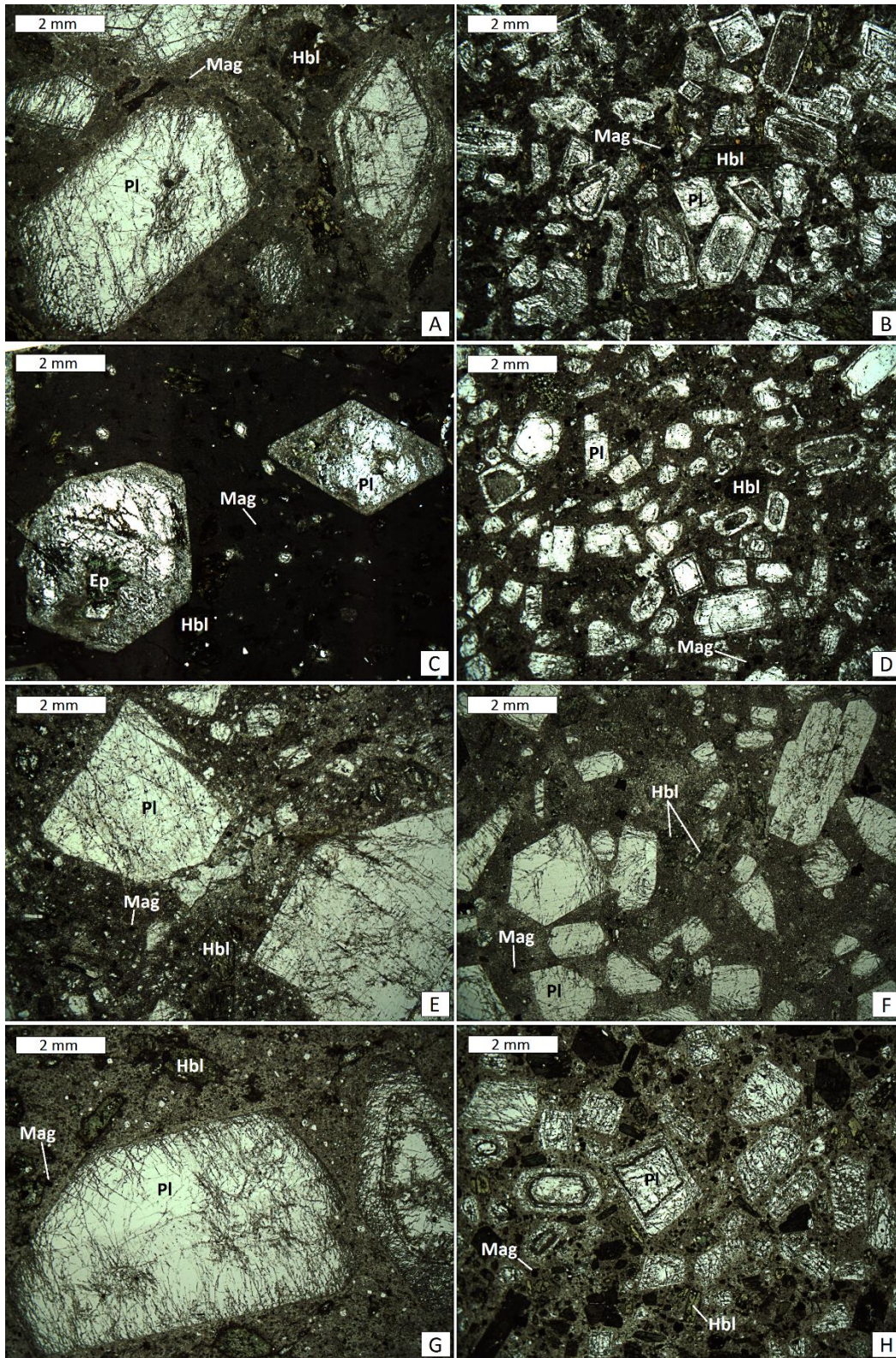


Figure 29. Photomicrographs taken in plane-polarized light, showing textural variation between cross-cutting intrusive sheets. All images captured at 2x magnification. (A) CC3a is a sill, cross-cut by (B) CC3b; (C) CC7b is a sill, cross-cut by (D) CC7a; (E) CC81b is a sill, cross-cut by (F) CC81a; (G) CC160b is a sill, cross-cut by (H) CC160a. All sills (left) have notably larger plagioclase phenocrysts than dikes (right).

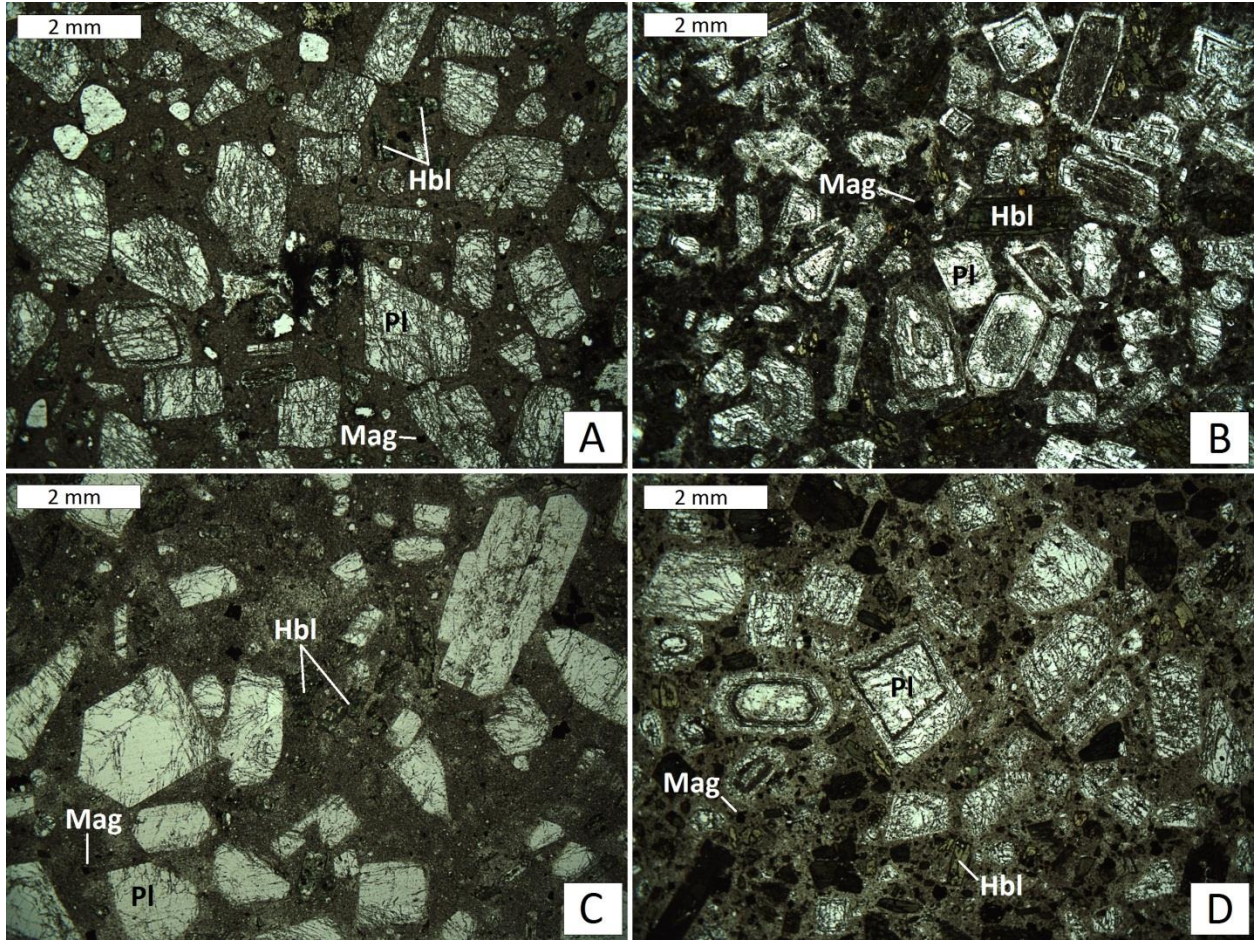


Figure 30. Photomicrographs taken in plane-polarized light, comparing CIB texture (A, CC94) and fine- to medium-grained dike texture (B, C, D). B, C, and D are CC3b, CC81a, and CC160a, respectively.

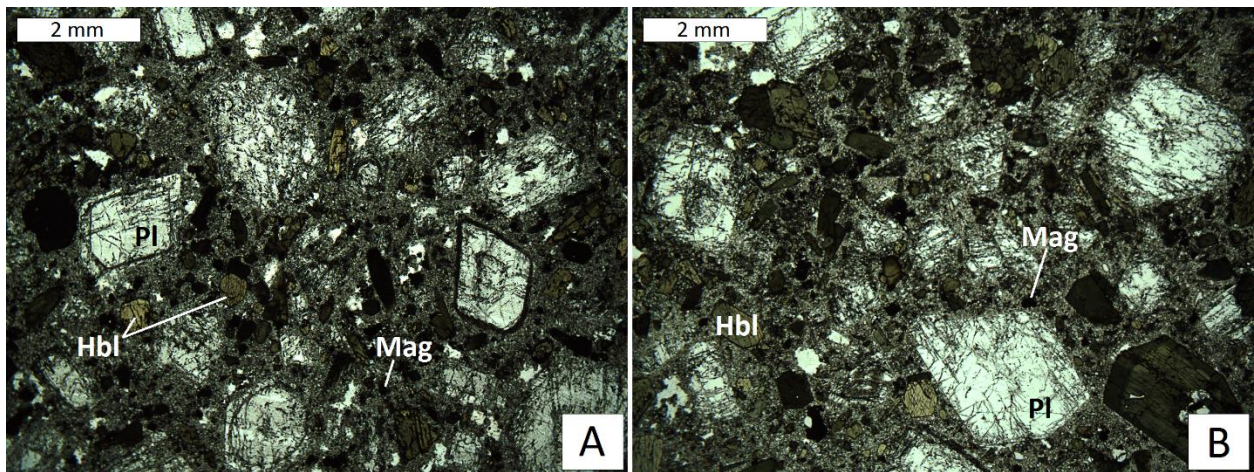


Figure 31. Photomicrographs taken in plane-polarized light, comparing CC57a (A, sill) and CC57b (B, dike), from intrusive sheets in the eastern region of the field area.

Ubiquitous fracturing exists in plagioclase phenocrysts (Figure 32). Alteration of plagioclase is concentrated along these fractures, and may include sericite with some opaques (most likely magnetite). Alteration rings are also common in the plagioclase phenocrysts. A typical phenocryst from these rocks may include a relatively clean core surrounded by a thin, dark band of mineralization, with a final relatively clean outer zone. There is variation, in that some phenocrysts have no visible alteration rings, while others have many. The dark mineralization bands may include plagioclase-altered sericite and opaques (probably magnetite). Hornblende alteration is variable; while some phenocrysts exhibit minimal alteration, most show some pseudomorphic chlorite-calcite-magnetite alteration.

Sedimentary thin sections of the four lowest exposed units on Mount Hillers show several interesting features (Figure 33). The Moenkopi formation in the study area is predominantly a silty sandstone, with quartz grains (ranging from silt to very fine-grained sand) in a chlorite groundmass, a possible alteration product of clay minerals. Notable in the Moenkopi are magnetite crystals within the groundmass (Figure 33A), that probably formed during the alteration of the clay-rich groundmass to chlorite. The White Rim sandstone is a tan quartzite. In thin section, grains range from 250 to 500 microns. Preserved bedding is recognized by parallel bands of small quartz grains ranging from 60 to 250 microns (Figure 33B). The Organ Rock Tongue outcrops as a green hornfels. The thin section shows small quartz grains ( $\leq 60$  microns) in a chlorite groundmass (Figure 33C). A major feature present is an actinolite-chlorite veinlet that most likely formed during an influx of fluid related to contact metamorphism. In outcrop, the Cedar Mesa sandstone member is a highly fractured quartzite. Crystal size ranges from ~60 to 500 microns. The quartzite is in direct contact with a coarse-grained sill (Figure 33D). Along with fractures in the quartzite, a general reduction in crystal size is observed with

proximity to the contact. Also noteworthy are the quartz inclusions within the porphyry, likely ripped from the sandstone during intrusion.

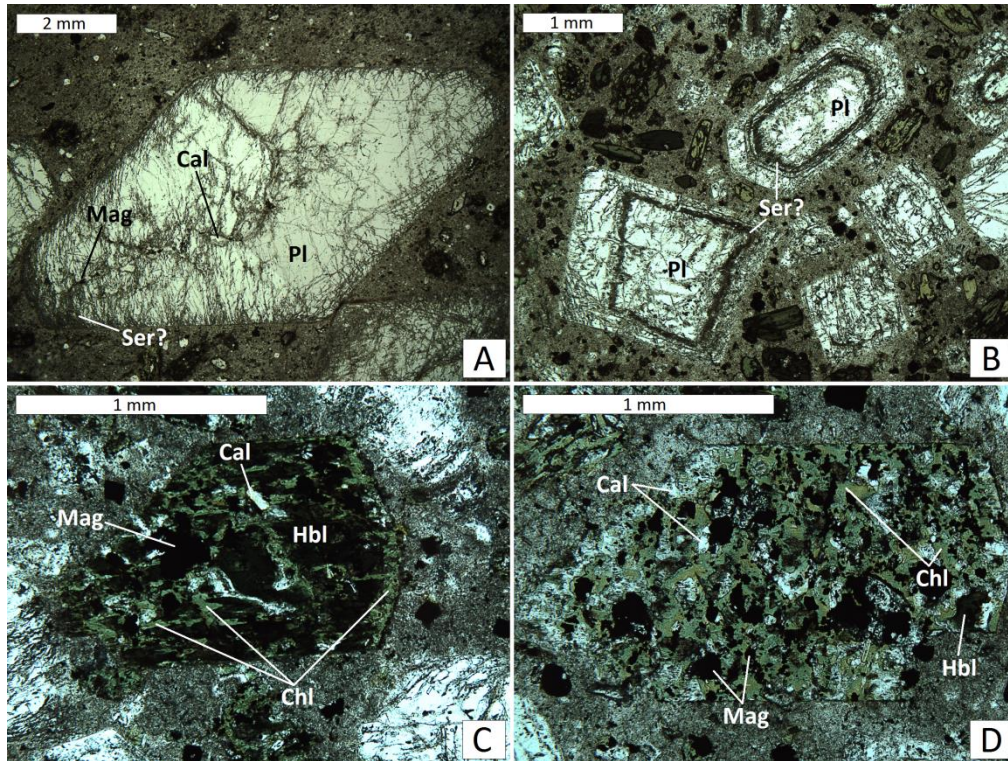


Figure 32. Photomicrographs taken in plane-polarized light, showing select features and alteration in phenocrysts. (A) Plagioclase phenocryst with extensive fracturing and associated alteration. (B) Plagioclase phenocrysts with alteration halos of sericite(?) surrounding the cores. These halos mirror the zoning orientations. (C, D) Hornblende phenocrysts extensively altered to pseudomorphic chlorite, calcite and magnetite.

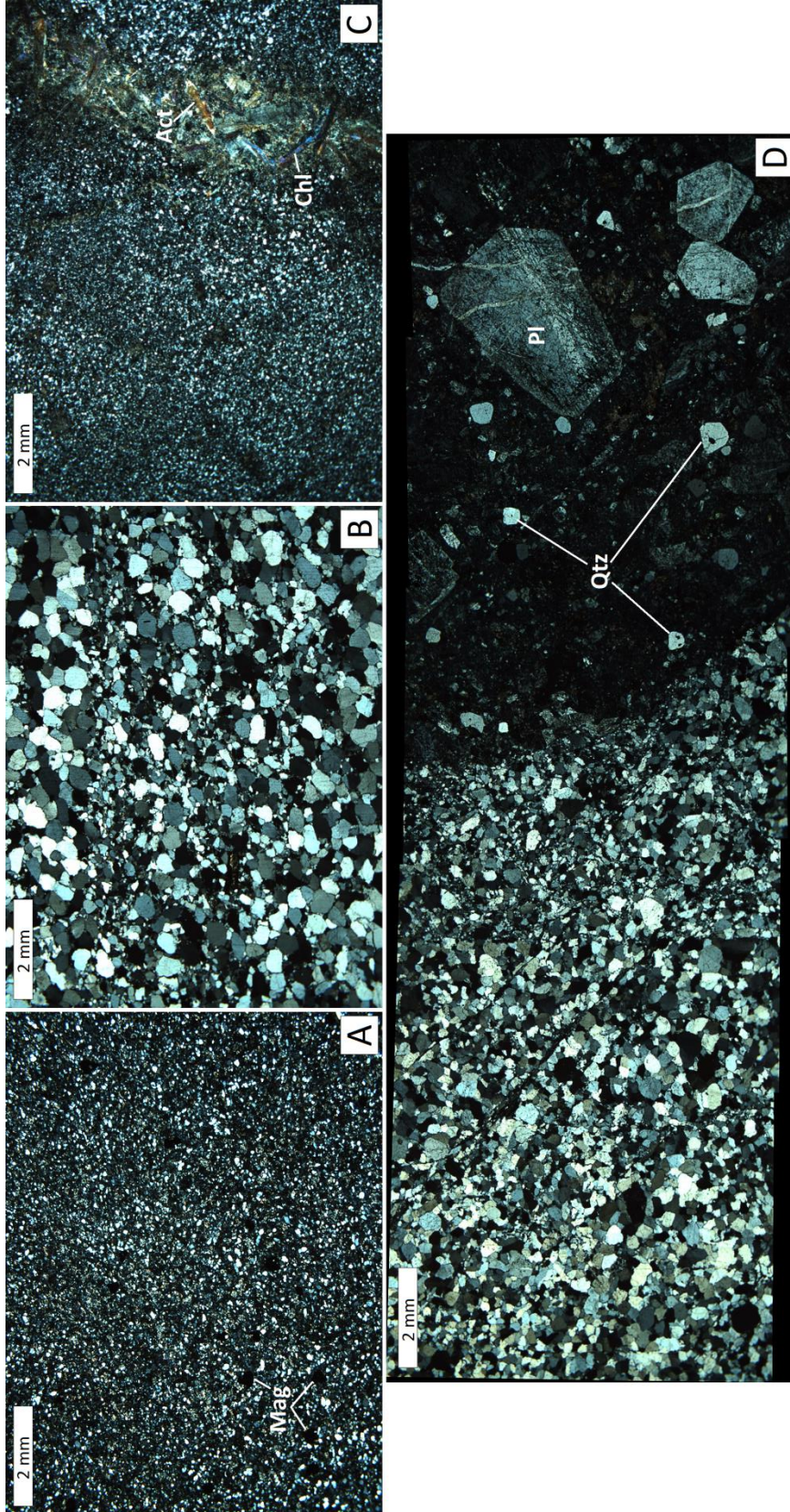


Figure 33. Photomicrographs taken in cross-polarized light, presenting select features in the four lowest exposed sedimentary units on Mount Hillers. (A) Moenkopi formation, quartz grains in a chlorite groundmass, with magnetite crystals. (B) White Rim sandstone, now metamorphosed to quartzite. Preserved bedding (parallel to top and bottom of photo) is defined by subparallel zones of relatively fine-grained quartz. (C) Organ Rock Tongue, metamorphosed to hornfels, quartz grains in a chlorite groundmass. Veinlet of actinolite and chlorite observed on the right. (D) Photomicrograph stitch of Cedar Mesa sandstone (left) contacting porphyry sill (right). Cedar Mesa is metamorphosed to quartzite. Quartz grain inclusions are observed within the igneous porphyry.

## Geochemistry

SiO<sub>2</sub> contents (Appendix C) range from 58 wt. % to 62.5 wt. %, averaging 60.1 wt. %. Overall, these rocks are intermediate in composition and the results are consistent with previous geochemical analysis (Nelson and Davidson, 1993; Gwyn, 2011). Plotting total alkalis versus silica (Figure 34) produces a spread along the andesite/trachyandesite boundary, similar to that observed by Nelson and Davidson (1993). The fine-grained dikes show the least variation in overall composition, while the medium-grained intrusions (two dikes and two sills) and coarse-grained sills have slightly more variable compositions.

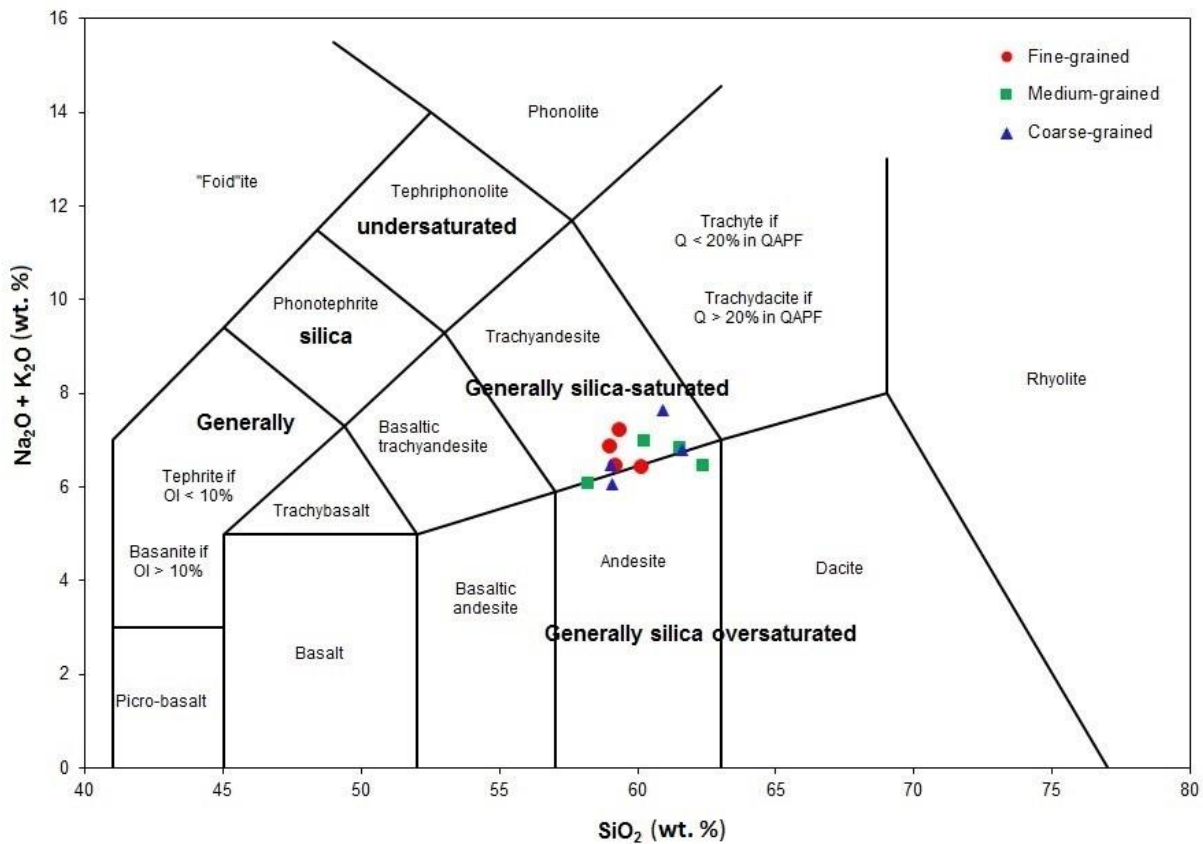


Figure 34. Total alkalis (Na<sub>2</sub>O + K<sub>2</sub>O) versus silica (SiO<sub>2</sub>) diagram (Le Bas et al., 1986) for samples from twelve intrusive sheets on the southern flank of Mount Hillers.

K<sub>2</sub>O abundances and eleven trace elements (Rb, Zr, Th, Hf, La, Ce, Pr, Nd, Sm, Dy, and Lu) showed statistically significant (1-sigma) variation with respect to texture. In all cases, fine-grained dikes were enriched in the analyzed element relative to medium- and coarse-grained samples, and coarse-grained sills tended to be most depleted in these elements (nine of the twelve elements). K<sub>2</sub>O, Rb, Zr, and Nd were mapped (Figure 35) to look for spatial trends. Highest abundances are generally observed in the south-central region of the field area, while the lowest abundances tend to concentrate in the southwest region. These spatial trends may be artifacts of the sampling, however; the south-central region is composed of three dike samples, and three of the five samples in the southwest region are sill samples.

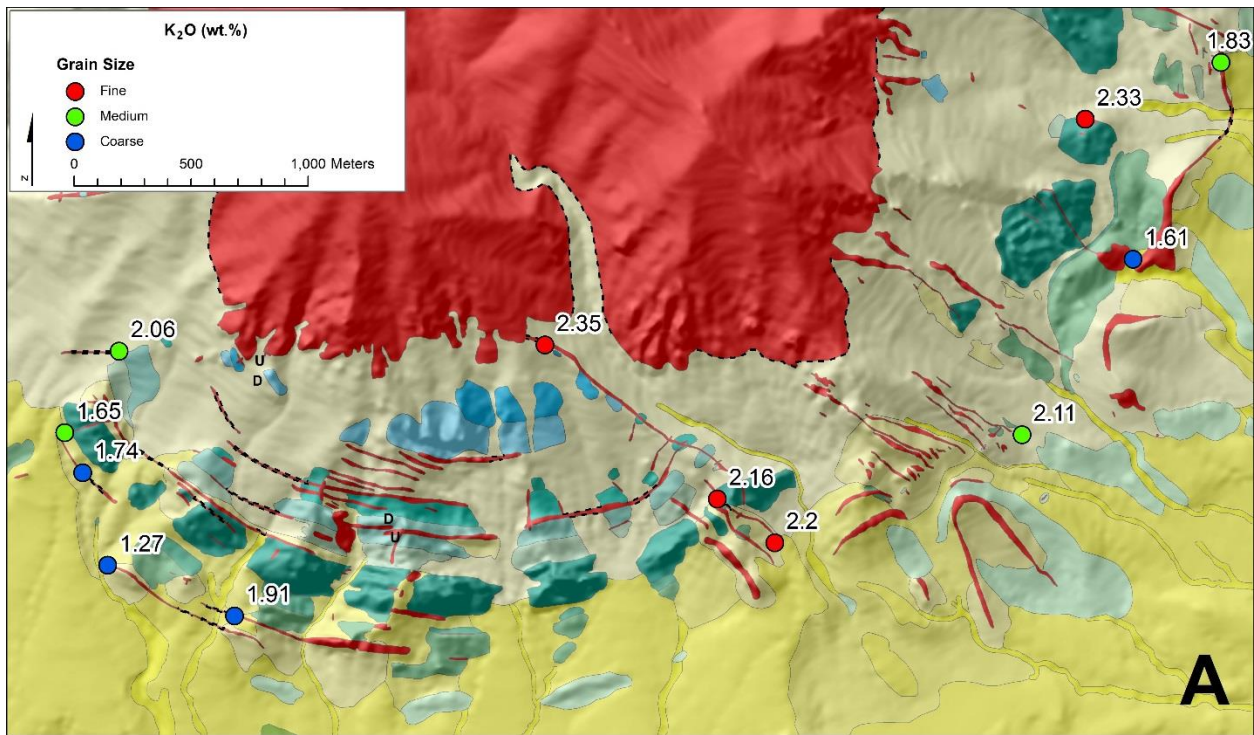
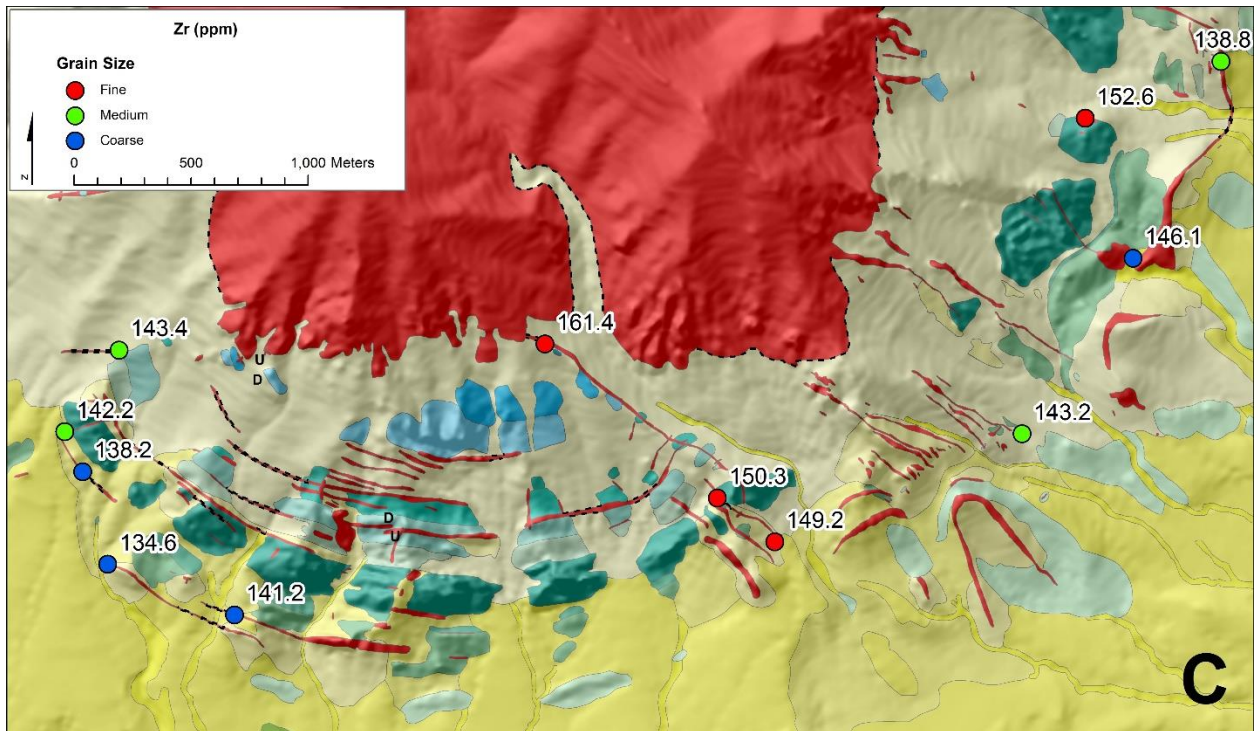
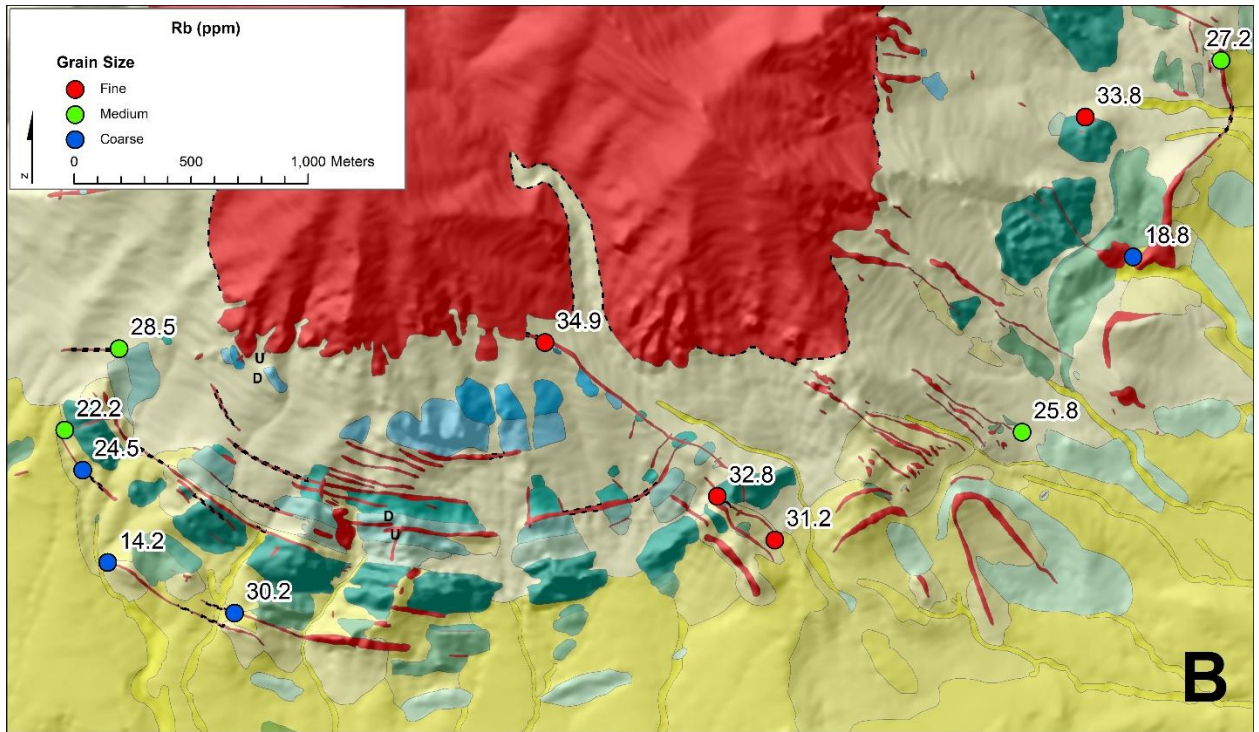
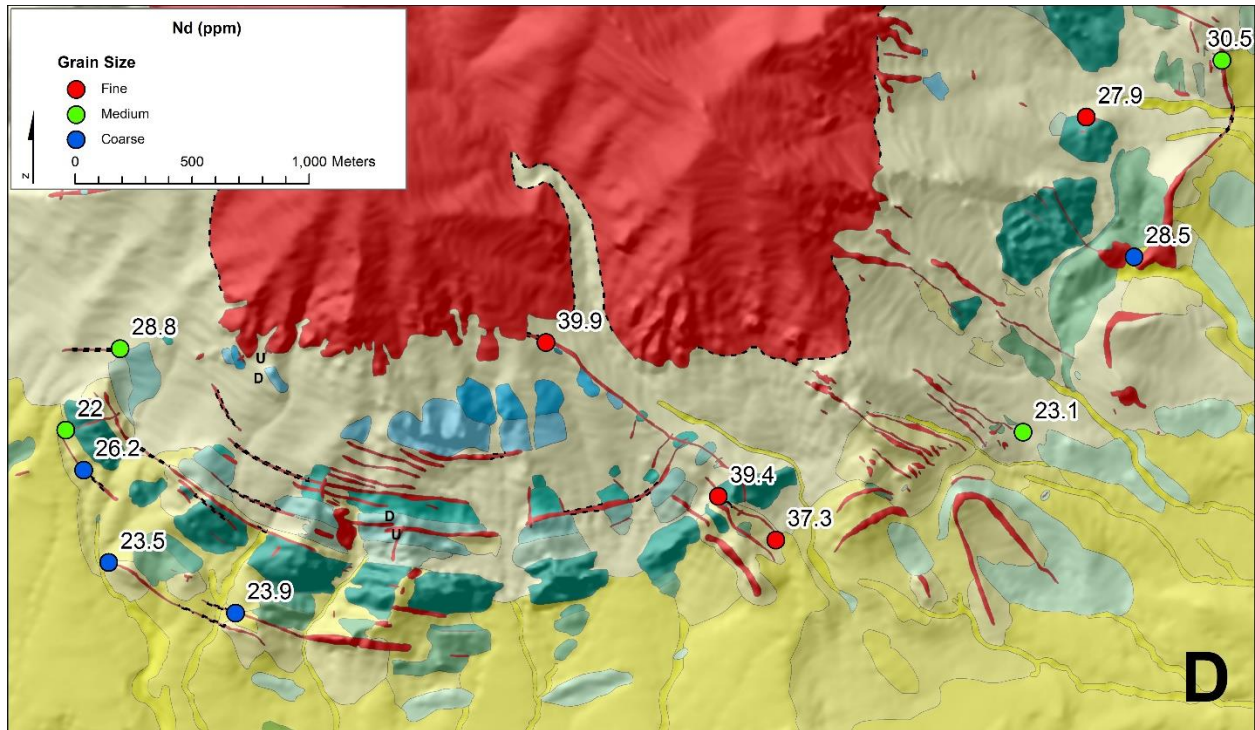


Figure 35. Select major and trace element abundances which show statistically significant variation with respect to grain size, mapped at their sampling locations. (A) K<sub>2</sub>O abundances in wt. %. (B) Rb abundances in ppm. (C) Zr abundances in ppm. (D) Nd abundances in ppm.





Plotting trace element abundance versus silica content (Figure 36) illustrates several trends: (1) The fine-grained dike samples have the highest overall trace element abundances; and (2) With higher silica content, the range and abundance of trace elements decreases. Because sampling size is low, these preliminary trends may simply be artifacts. However, these elements do show statistically significant variation to one standard deviation, so the observed trends are worth discussion.

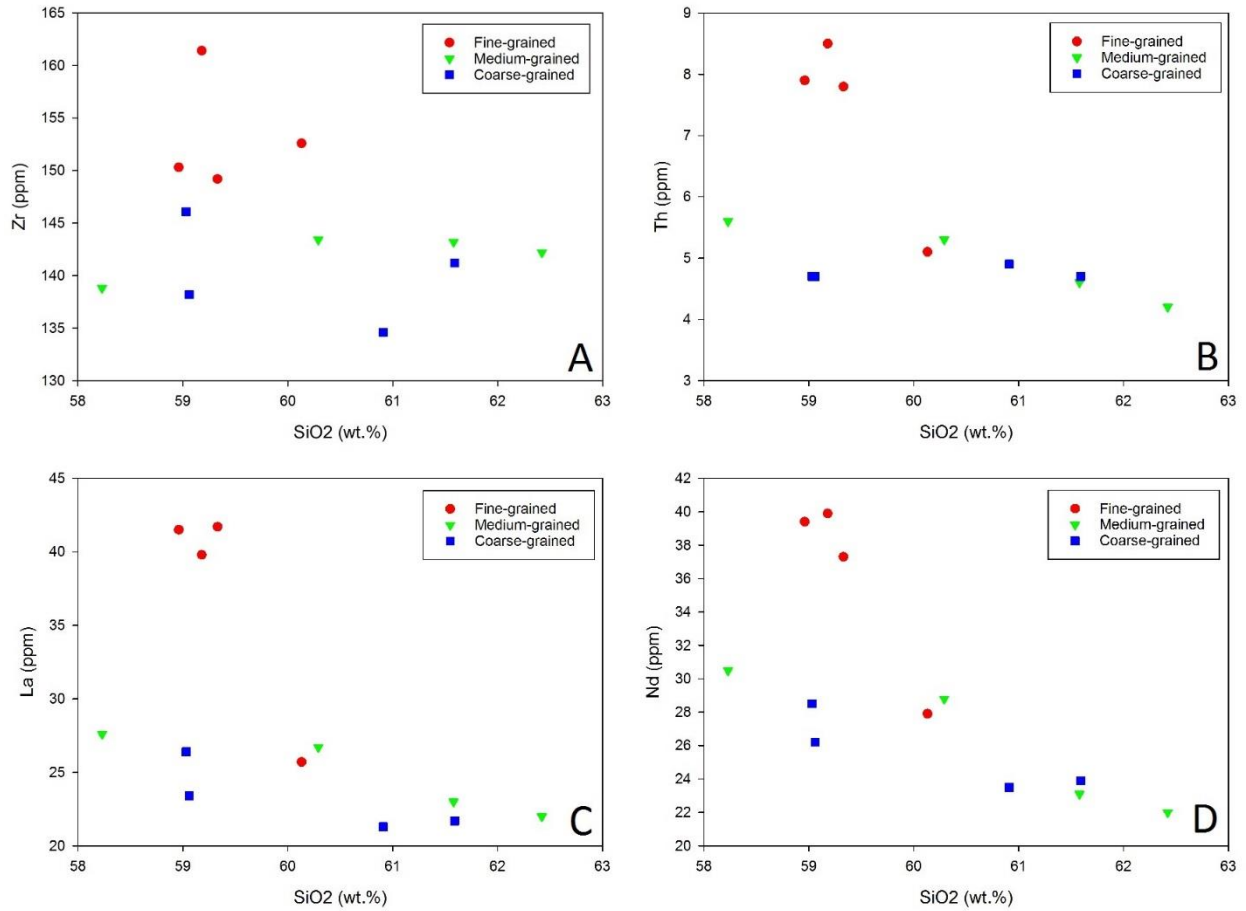


Figure 36. Select trace element variations (ppm) versus SiO<sub>2</sub> (wt. %) diagrams for fine-, medium-, and coarse-grained samples. (A) Zr vs. SiO<sub>2</sub>. (B) Th vs. SiO<sub>2</sub>. (C) La vs. SiO<sub>2</sub>. (D) Nd vs. SiO<sub>2</sub>.

Chondrite-normalized (McDonough and Sun, 1995) rare earth element (REE) patterns show variation between textures (Figure 37) and intrusion type (Figure 38). REE patterns for normalized grain size averages and intrusion type averages (Figure 37D, Figure 38C) illustrate the relative REE enrichment of fine-grained dike samples to medium- and coarse-grained sill samples. Low values and flattening of the REE pattern is observed in the heavy REE. No significant Eu anomaly is observed in the REE patterns.

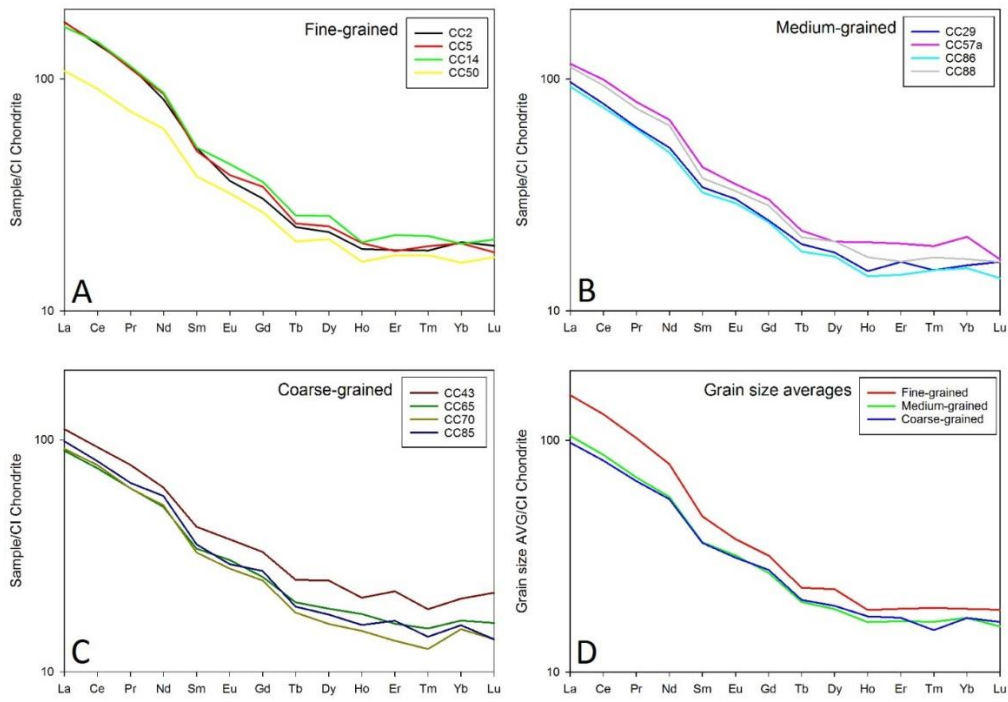


Figure 37. Chondrite-normalized (McDonough and Sun, 1995) REE patterns for fine-, medium-, and coarse-grained intrusion samples. (A) Fine-grained REE patterns. (B) Medium-grained REE patterns. (C) Coarse-grained REE patterns. (D) Normalized average grain size REE patterns for fine-, medium-, and coarse-grained samples.

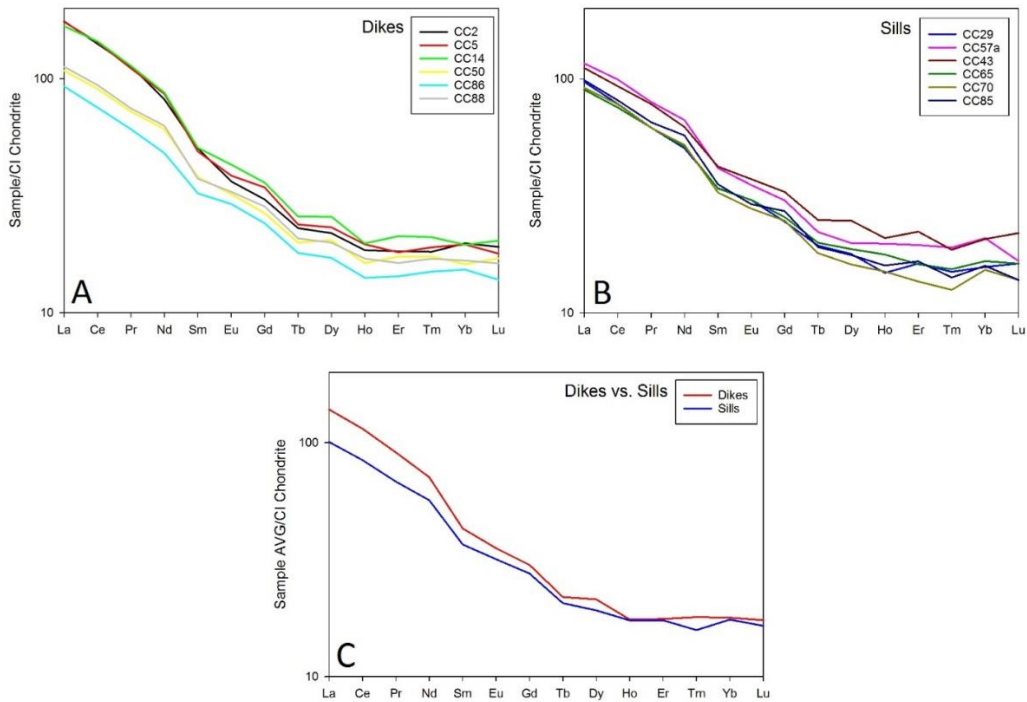


Figure 38. Chondrite-normalized (McDonough and Sun, 1995) REE patterns for dikes and sills. (A) Dike REE patterns. (B) Sill REE patterns. (C) Normalized dike and sill average REE patterns.

## Anisotropy of Magnetic Susceptibility

$K_1$  orientations (magnetic lineations) in sills have been rotated to horizontal around the strike of bedding, assuming the strata were subhorizontal when sills were emplaced. The orientations (Appendix D) of these fabrics vary by region (Figure 39): (1) fabrics in the SW trend broadly along a NW-SE girdle; (2) fabrics in the S-SE trend broadly along an E-W girdle; (3) fabrics in the E trend broadly along a NE-SW girdle. The girdle orientations are similar to tilted sill orientations observed in the respective regions. Magnetic lineations in dikes were not rotated, assuming they intruded during the final stages of CIB growth after rotation of the host rock. The orientations of these fabrics also vary by region: (1) fabrics in the SW trend very broadly NE-SW with shallow plunges; (2) fabrics in the S-SE trend broadly SE-NW, plunging subhorizontally to steeply; (3) fabrics in the E trend broadly ESE-WNW and plunge shallowly to subvertically. These lineation trends appear to correspond with the general orientation of dikes in their respective region.

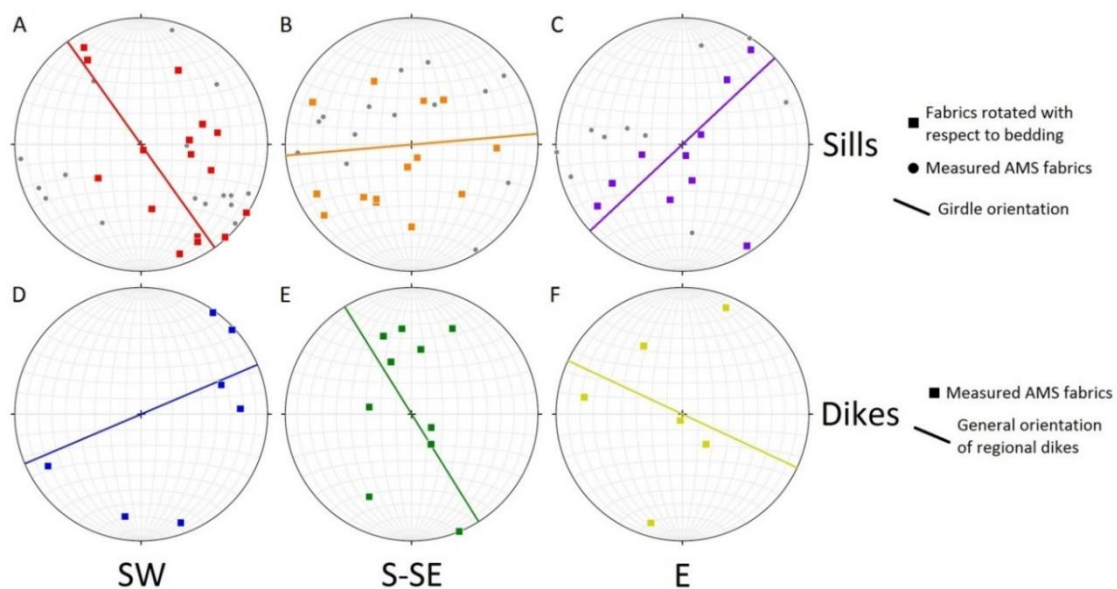


Figure 39. Equal angle lower hemisphere stereographic projections of magnetic lineations of sills (A, B, C) and dikes (D, E, F) in the three regions (SW, S-SE, E) of the study area. Grey dots represent measured AMS lineation orientations, colored squares represent lineations rotated around the strike of bedding to paleo-horizontal, and colored lines represent the general orientation of regional sills and dikes.

Assuming subhorizontal emplacement of the sills,  $K_3$  orientations (poles to magnetic foliations) in sills have been rotated to horizontal around the strike of bedding (Figure 40). Magnetic foliation orientation patterns differ based on region: (1) in the SW, poles to magnetic foliations align broadly along a SW-NE girdle; (2) in the S-SE, poles to magnetic foliations align broadly along a SSE-NNW girdle; (3) in the E, poles to magnetic foliations align broadly along a SE-NW girdle. Magnetic foliation orientation patterns in dikes also vary based on region: (1) Magnetic foliations in the SW are roughly subhorizontal; (2) Magnetic foliations in the S-SE trend generally NW-SE, and dip moderately to steeply to the NE-SW; (3) Magnetic foliations in the E do not show a consistent pattern.

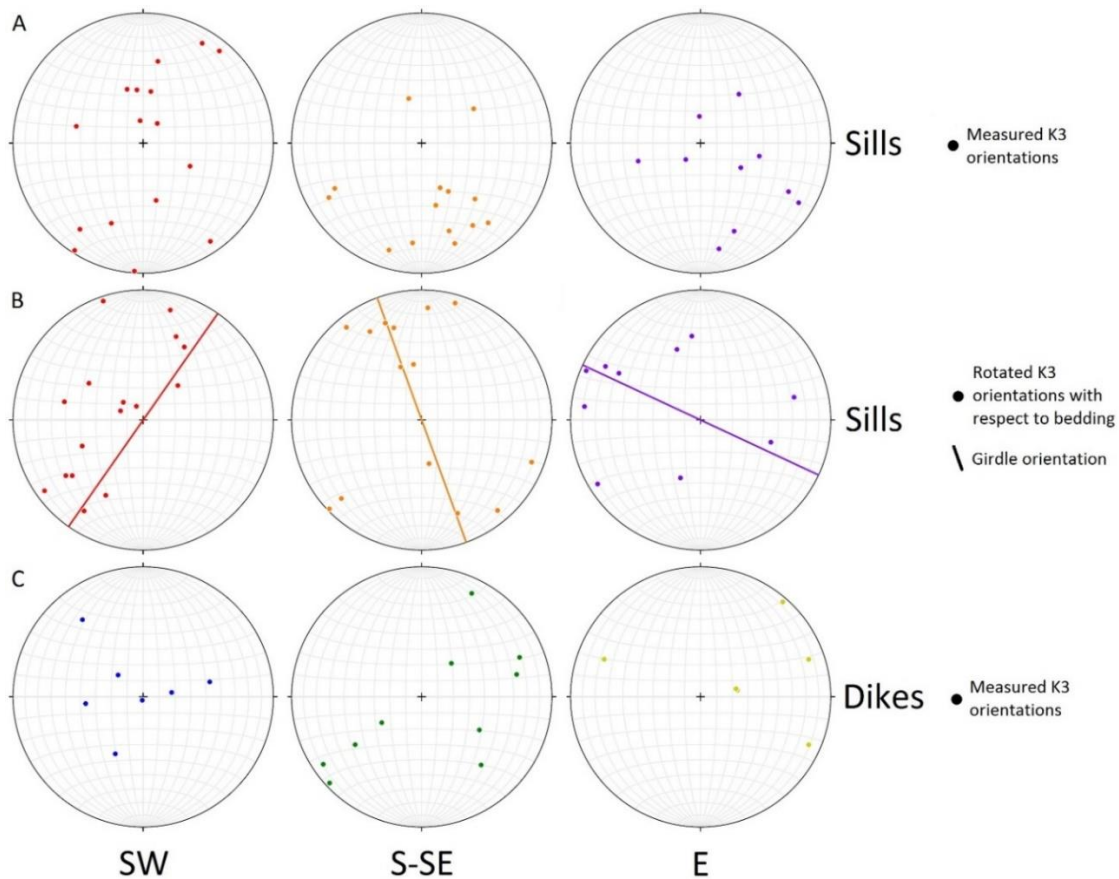


Figure 40. Equal angle lower hemisphere stereographic projections of measured and rotated magnetic foliations of sills (A, B) and dikes (C) in the three regions (SW, S-SE, E) of the study area. Grey dots represent measured AMS lineation orientations, colored squares represent lineations rotated around the strike of bedding to paleo-horizontal, and colored lines represent the general orientation of regional sills and dikes.

Scalar parameters calculated from the AMS results are plotted against each other in Figure 41. Bulk susceptibility ( $K_m$ ) ranges from 3560 to 46200  $\mu\text{SI}$ . Coarse-grained samples tend to have lower  $K_m$  values (16606  $\mu\text{SI}$  average) than fine-grained samples (30250  $\mu\text{SI}$  average), while medium-grained samples have intermediate values (23520  $\mu\text{SI}$  average). Similarly, samples collected from sills tend to have lower  $K_m$  values (18671  $\mu\text{SI}$  average) than samples collected from dikes (26783  $\mu\text{SI}$  average). No trends exist between  $K_m$  and the other scalar parameters.

Values of the degree of anisotropy ( $P_j$ ) range from 1.011 to 1.072. There is no significant difference in  $P_j$  values based on texture or intrusion type. At low  $P_j$  values, the greatest range of  $T$  values exist. As  $P_j$  values increase,  $T$  values decrease in range and become generally less negative. No trend exists between  $P_j$  and  $K_m$ .

Values for the shape parameter ( $T$ ) range from -0.572 to 0.635. Coarse- and medium-grained samples, and samples collected from sills, average a nearly spherical ( $T = 0$ ) fabric shape. Fine-grained samples, along with samples collected from dikes, average a generally oblate ( $T > 0$ ) fabric shape. No trend exists between  $T$  and  $K_m$ .

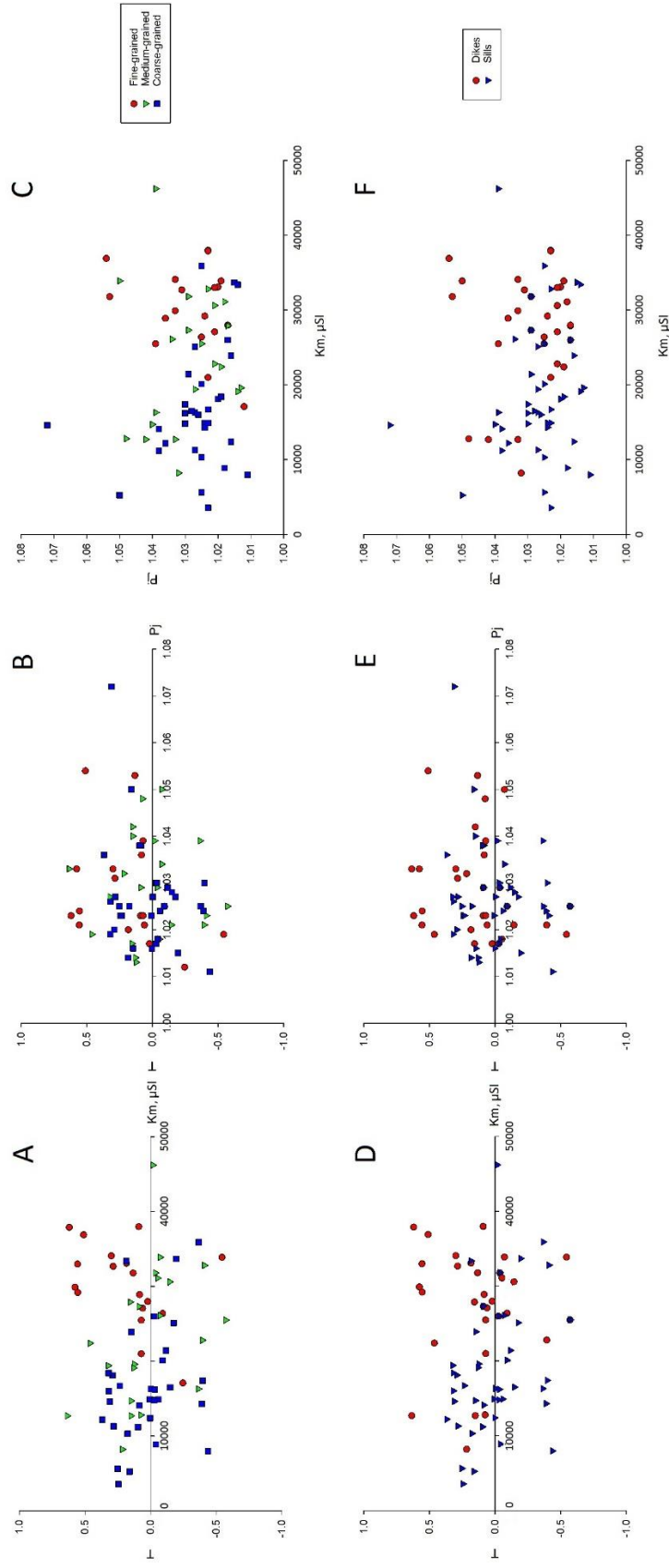


Figure 41. Plots of AMS scalar parameters based on grain-size (A, B, C) and intrusion type (D, E, F). (A, D) Shape parameter vs. degree of anisotropy. (C, F) Degree of anisotropy vs. bulk susceptibility. (B, E) Shape parameter vs. degree

## **Discussion**

### **Field Work**

My geologic map and cross sections illustrate a sedimentary rock deformation pattern consistent with doming of a central laccolithic body. This supports Jackson and Pollard's (1988) findings, as opposed to the central stock hypothesized by Hunt et al. (1953).

Pollard et al. (1975) posit that the tips of intrusive sheets propagate as fingerlike protrusions at the sheet margins. The authors believe these fingers originate in areas with preexisting weaknesses within the host rock. Driving pressure within the finger deforms the surrounding host rock, making space for the magma as the sill propagates. Porphyritic rocks in the study area do not exhibit notable zones of preferential fracturing that would lead to enhanced weathering and erosion. Therefore, the discontinuous, staggered outcrops observed in the field are interpreted as the very distal fingerlike lobes of a more continuous subsurface intrusive sheet (Figure 42). Uplift and erosion have presumably destroyed the less competent host rock that was previously in contact with these fingers. Fingered protuberances in intrusive sheets have been described previously (e.g. Hurlbut and Griggs, 1939; Tweto, 1951; Dutcher et al., 1966; Johnson and Pollard, 1973; Horsman et al., 2005), so this is a reasonable interpretation based on field observations.

Cross-cutting relationships and igneous inclusions indicate that sills in the field area are consistently older than the younger radial dikes. These observations are consistent with two very broad magma pulses in the construction of the intrusive sheet network: (1) an older pulse of magma with relatively large plagioclase phenocrysts emplaced as a series of sills in the sedimentary host rock; and (2) a younger pulse of magma with relatively small plagioclase

phenocrysts that cuts radially through both the sediments and sill complex. In detail, the pulsed construction history of the field area is most certainly more complicated than this. A synthesis of results from all techniques is used to devise a construction model, which is described in the final section of this discussion.

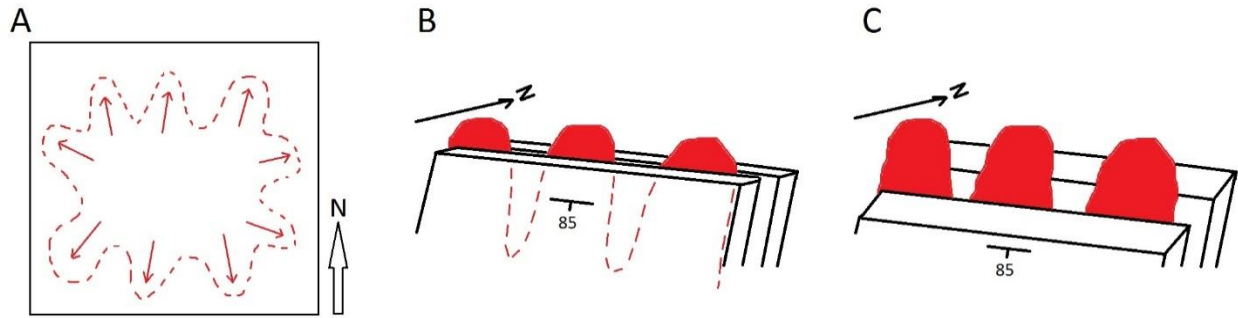


Figure 42. Schematic diagrams of general finger geometries observed in intrusive sheets. (A) Map view of a subsurface sill, outlined in red. Finger-like protrusions line the margins of a central continuous body. (B) Block diagram of the fingered margin of a sill (red) between sedimentary host rock (black). Strata and sill have been tilted to subvertical to mirror attitudes on the southern margin of Mount Hillers. (C) Block diagram of strata and sill, now eroded to resemble observations from the southern margin of Mount Hillers.

Subhorizontal, radially trending field fabrics in sills, following rotation to bedding-horizontal, are consistent with subhorizontal, radial spreading of magma from unexposed subvertical feeders. Shallowly to steeply plunging field fabrics in dikes aligning generally along the trend of regional dike orientations may suggest that dikes intruded throughout host rock rotation, and not just during the final stages of CIB growth. If this is the case, the subvertical rotation of the earliest dikes likely produced the observed subhorizontal fabrics, while the latest dikes intruded post-rotation and yielded the observed subvertical fabrics. Moderately plunging fabrics record the intermediate rotation of dikes that intruded sometime during the tilting of strata by CIB growth. It should be noted that because field fabrics in the study area are often weak, these interpretations are tentative.

Despite no direct observations of dike contacts with the CIB, the radial outcropping and aerial photography analysis suggest that dikes originated from the CIB and exploited radial fractures

throughout the overburden as the central dome of the CIB grew (Jackson and Pollard, 1990). Combined with the common emplacement of sills along bedding planes throughout the study area, it is evident that propagating magma commonly exploits preexisting host rock weaknesses during intrusion.

Field observations of sill thickness variability are consistent throughout the study area. Sills intruding at least partially incompetent host rock (i.e. shale-shale or sandstone-shale contact) are consistently thicker than sills intruding more competent host rock (sandstone-sandstone contact). These observations are consistent with the hypothesis that rigidity contrasts in host rock may influence sill emplacement (Kavanagh et al., 2006; Menand, 2008). I hypothesize that rigidity contrasts may affect not only the location of sill emplacement, but also the thickness of sills. Interestingly, the experimental results of Kavanagh et al. (2006) found that under hydrostatic conditions, sills only formed when the feeder dike ascended to the contact between underlying incompetent material and overlying competent material. Observations of this study show that sills can form at the contact between underlying competent rock and overlying incompetent rock (e.g. the east sill in Figure 24 intrudes the contact between underlying Entrada sandstone and overlying Summerville shale).

According to Menand (2011), buoyancy, rheology, rigidity, and stress control sill emplacement in the crust. Field observations (e.g. Johnson and Pollard, 1973) and seismic data (e.g. Thomson and Hutton, 2004) do not support neutral buoyancy as a sole mechanism for dike arrest and sill emplacement. In the study area, the shallow depth of emplacement (2-4 km) suggests dominantly brittle rock behavior, meaning rheology contrasts are likely insignificant. While host rock rigidity contrast is most likely an important factor for sill emplacement in this study, it alone does not explain the location of the sills described above. Finally, because no

evidence exists for syn- or post-emplacement regional deformation, stress rotation caused by shifting stress regimes is not a controlling factor in this case. As none of the major emplacement mechanisms explain the location of sills with incompetent roof rocks observed in this study, I interpret these sills formed as a result of declining magma pressures during ascent.

### **Crystal Size Distribution**

The broadly steady slope observed in the hornblende CSDs is consistent with nearly steady-state crystallization of hornblende phenocrysts. The shallowly sloping segment of the CSDs indicates there are fewer small crystals than expected and suggests a change in conditions under which hornblende was crystallizing. Rapid cooling at shallow depths increases nucleation and leads to reduced crystal size, typically producing CSDs of much steeper slopes at small crystal sizes. Instead, the observed shallowing of slope might be explained by a brief period of textural coarsening at depth, as explained by Higgins (1998): (1) as magma resides in deep crustal chambers, hornblende and plagioclase crystallize; (2) with continued crystallization, heat is retained and reduces undercooling, which limits nucleation; (3) smaller crystals are resorbed into melt, allowing for the coarsening of already large crystals. Textural coarsening of hornblende phenocrysts would have abruptly ceased once magma began rapid ascent and cooling to form the aphanitic matrix at shallow depths in the crust. Finally, although hornblende CSDs are similar across textures and intrusion types, the smaller maximum crystal size observed in coarse-grained sills is notable. As nucleation densities for hornblende are similar in all samples, growth conditions (growth rate and/or residence time) for coarse-grained sills likely differed from those of the fine- and medium-grained intrusive sheets.

Two distinct CSDs in plagioclase phenocrysts indicate that coarse-grained sill magma crystallized under different conditions from the fine- and medium-grained magmas. The slight concave up shape observed in the coarse-grained sill samples may be a result of either magma mixing (Higgins, 1996) or sequential cooling events at increasingly shallow levels in the crust (Armienti et al., 1994), or both. Given the relative geochemical homogeneity of porphyritic rocks in the field area, the contribution of magma mixing is most likely limited. Therefore, it appears sequential crystallization at varying depths in the crust produced the slight curve in coarse-grained sill CSDs. The steep, relatively straight CSDs of fine- and medium-grained samples suggest a possible single stage of crystallization of these magmas. Greater maximum crystal sizes in coarse-grained samples may suggest the respective magma resided longer in a deep chamber than the fine- and medium-grained samples.

Lower nucleation densities and greater characteristic lengths are representative of low undercooling at depth. Greater nucleation densities and lesser characteristic lengths are typical of higher degrees of undercooling at shallower depths. Results summarized on Figure 28 further suggest different crystallization histories for coarse-grained samples and fine- and medium-grained samples. One possible scenario to explain these results is that a volume of magma crystallized slowly in a deep chamber before ascent and emplacement as coarse-grained sills. Later, another volume of magma spent less time cooling at depth before ascending to shallow crustal levels as fine- and medium-grained dikes and sills, and possibly the CIB.

### **Thin Section Petrography**

The textural variations observed in thin section support the field observations and CSD data: coarse-grained sills and fine-grained dikes have distinct crystallization histories. The

textural similarities between sample CC94 (interpreted as representative of CIB) and fine-grained dike samples suggest that the CIB and dikes crystallized from a similar magma. These observations are consistent with the hypothesis of Jackson and Pollard (1988) that late stage radial dikes originated from the CIB. Textural similarities and lack of a distinct contact between samples CC57a and CC57b suggest that these intrusive sheets represent a cohesive dike/sill system where the dike magma ascended and directly fed the sill.

The intensity of fracturing observed in the plagioclase phenocrysts is pervasive. The Colorado Plateau has been relatively stable since ascent and emplacement of magma ~25 Ma, so regional deformation is likely not responsible. Several possibilities exist to explain the widespread intense fracturing of plagioclase phenocrysts: (1) strain partitioning in plagioclase phenocrysts during deformation attributed to CIB growth, assuming sill and dike intrusion occurred before the CIB finished growing; (2) expansion and subsequent decompression of plagioclase phenocrysts as magma ascended through the crust and cooled rapidly at shallow depths; and (3) fracturing may be a result of thin section preparation. Alternating zones of plagioclase and dark alteration rings in plagioclase phenocrysts suggest a complex history of alternating phases of crystallization during storage and unstable decomposition during ascent. This interpretation is consistent with the sequential crystallization at varying depths suggested by the concave CSD curve observed in coarse-grained sill samples. Zoning in the plagioclase phenocrysts of dike samples suggests a similar step-wise ascent through the crust; however, this ascent was probably rapid as suggested by the relatively straight CSDs for fine-grained dike samples.

The contact metamorphic zone at the outer margin of the CIB was documented in Jackson and Pollard (1988) as extending to the base of the White Rim sandstone. Thin sections

of Cedar Mesa, Organ Rock Tongue, and White Rim confirm metamorphism from the CIB reaches at least this far. However, possible chlorite alteration of clay minerals and magnetite crystals in the Moenkopi formation suggests the metamorphic aureole may extend farther than initially reported. As metamorphism associated with minor sills is localized to <1 meter-thick baked zones adjacent to contacts, the alteration observed in the Moenkopi thin section is most likely related to contact metamorphism with the CIB.

## **Geochemistry**

The plot of total alkalis vs. silica (Figure 34) shows compositional variation is limited in fine-grained dike samples. If the radial dikes originated from the CIB as proposed by Jackson and Pollard (1988), this common source explains this observation. Medium- and coarse-grained intrusions have higher compositional variation relative to fine-grained dikes. While likely not enough variation to suggest multiple distinct sources, different individual crystallization histories may explain the variations observed.

Relative trace element enrichment in fine-grained dike samples is likely explained by higher hornblende concentrations in these samples relative to coarse-grained sill samples. The general decrease in both range and abundances of trace elements with increasing silica content is unusual. Nelson and Davidson (1993) observed a similar trend with enriched mafic samples and depleted evolved samples from Mount Ellen in the Henry Mountains. They suggested apatite fractionation resulting in REE depletion in the residual melts as an explanation for this phenomenon. Zircon, apatite, and monazite (REE-bearing phosphate) fractionation during early magma evolution may explain the lower REE abundances observed in samples with higher silica content.

REE variation between fine-grained dikes and coarse-grained sills suggests distinct crystallization histories of the associated parent magmas (e.g. the parent magmas underwent varying degrees of fractional crystallization). Given the relative abundance of plagioclase phenocrysts in these rocks, the absence of a Eu anomaly is significant. Nelson and Davidson (1993) also observed this phenomenon, and proposed a low  $\text{Eu}^{2+}/\text{Eu}^{3+}$  ratio stemming from oxidizing magmatic conditions (after McKay, 1989). Alternatively, the lack of a Eu anomaly may be explained by a lack of either plagioclase addition to or segregation from a crystallizing magma body.

### **Anisotropy of Magnetic Susceptibility**

Previous studies in the Henry Mountains have used AMS to make interpretations of magma flow within single igneous bodies (e.g. Horsman et al., 2005; Morgan et al., 2008). Consistently subhorizontal magnetic lineations were mapped and interpreted to represent the internal flow of magma within these single intrusions into subhorizontal sedimentary rocks. In this study, numerous intrusive bodies reside within three different regions, and internal magma flow patterns for each individual intrusive sheet of similar orientation were different to some degree. Also, variation in the strike of intrusion orientation can vary by as much as  $\sim 50^\circ$  within a region. These factors complicate the interpretations of the magnetic fabrics. Cañón-Tapia (2004) reviews some of the difficulties with interpreting AMS results in tabular intrusions, and states in some cases, AMS interpretations may remain uncertain. The interpretations provided below are tentative, and future study in the area should involve more rigorous sampling of sheet intrusions (multiple samples per intrusion along transects across length and width) in an attempt to provide clearer data, allowing for better interpretations.

Given the subhorizontal sill emplacement suggested by Jackson and Pollard (1988), magnetic lineations rotated around the strike of bedding to horizontal are expected to plunge subhorizontally to reflect magma flow direction within the plane of the intruding sheet. However, magnetic lineation data do not reflect this expected pattern, as orientations of these fabrics are subhorizontal to subvertical. There are several possible explanations for these data. First, the AMS fabrics may not be tracking magma flow in these sheet intrusions. Hornblende alteration is commonly observed in thin section, and magnetite is a common product of this alteration. The orientations of these new magnetite grains may not reflect magma flow patterns during intrusion, and therefore may complicate AMS data, as suggested by Rochette et al. (1991). Another possible explanation for the complex AMS fabrics is related to complex magma flow within sheet intrusions. Depending on the sampled location within an intrusion, the fabric may reflect very different conditions in flow (e.g. fabric imbrication along intrusion margins, possible directional dispersion within the center of the intrusion), as suggested by Neres et al. (2014).

Across the regions of the study area, variation in the plunge of magnetic lineations of sills broadly indicates that the magma flow within sills was complex. A rough interpretation of the AMS fabrics may suggest that sill emplacement orientation changed in relation to the orientation of the overburden during CIB growth. Following fabric rotation to horizontal, the following broad interpretations are made: (1) shallowly plunging AMS lineations record expected magma flow directions of sills through subhorizontal strata prior to CIB growth; (2) moderately and steeply plunging AMS lineations represent magma flow in sills that intruded strata that was uplifted and tilted as a result of doming around the CIB.

Magnetic lineations of dikes are interpreted to reflect the magma flow direction of dikes by region. Following the interpretations for dike field fabrics, subhorizontal magnetic lineations in the SW region suggest dikes flowed subvertically up from the CIB and were subsequently rotated during CIB growth and host rock rotation. Subhorizontal to subvertical magnetic lineations in the S-SE and E regions record the intrusion and flow of dikes and subsequent rotation of these intrusive sheets throughout CIB growth.

Magnetic foliation planes are interpreted to lie subparallel with the plane of intrusion, and record flattening forces during emplacement as magma flowed between layers of restrictive sedimentary host rock. Similar to magnetic lineations, variation in the magnetic foliations of sills is interpreted as variation in emplacement orientation of sills, and suggests that sill emplacement did not occur as one large event, but transpired progressively as the CIB grew and rotated the surrounding host rock. Following magnetic pole to foliation rotation around the strike of bedding to horizontal, samples with subhorizontal magnetic foliations represent subhorizontally intruded sills, while samples with subvertical magnetic foliations represent subvertically intruded sills. Samples with moderately dipping magnetic foliations represent sills that intruded moderately dipping strata. Interpretations for magnetic foliation planes in dikes are consistent with the interpretations of the respective magnetic lineations in dikes.

While not statistically significant, the variation in bulk susceptibility between textures and intrusion types is notable and is possibly a result of the difference in abundance of magnetic minerals in the rocks. This variation may suggest the involvement of distinct magma pulses in the intrusion of coarse-grained sills and fine-grained dikes.

Weak to moderate agreement exists between field fabrics and AMS fabrics. Of the 17 AMS samples that had corresponding field fabrics measured within 20 meters of the sample location, 8 samples shared subhorizontal, moderate, or subvertical fabrics with the respective field-measured counterparts. AMS fabrics are usually within  $40^\circ$  of the corresponding field fabric, and are very rarely perpendicular. Because field fabrics measure the shape preferred orientation of hornblende in the field and AMS measures the magnetic properties of the rock, total agreement between these techniques is not expected. Variability between the results of these techniques may be ascribed to the relatively small size of the field fabric data set. Also, as field fabrics are often weak, the precision with which field fabrics are measured may lead to variability. Overall, the field fabrics do not contradict the AMS fabrics in this study.

### **Proposed Mount Hillers Construction Model**

The growth model of central igneous domes in the southern Henry Mountains proposed by Jackson and Pollard (1988) is largely supported by results from this study. However new data from this study suggest that certain aspects of this proposed growth history are more complex than initially considered. Below is a revised construction model for Mount Hillers, accounting for new data.

Horizontal sill intrusion into the upper 4 km of the crust began  $\sim 25$  Ma (Figure 43A). Field evidence (Figure 22) suggests this magma reached the shallow crust through initially subvertical dikes. Many of these sills had relatively small volumes of 0.01 to 0.1 km<sup>3</sup> (Jackson and Pollard, 1988). Concurrently, at the base of the Permian Cutler formation, the incipient CIB began to grow. Whether through continuous injection of magma from depth or vertical stacking of individual sheets, the growth of the CIB began gently doming the overburden to make space

for itself (Figure 43B). This early-stage CIB may have reached the appropriate size where magma fluid pressure was greater than overburden weight, resulting in uplift and bending of the overburden. Deformation associated with doming of the overburden included bedding plane faults, radial and circumferential host rock stretching, and radial fractures (Jackson and Pollard, 1990).

Rotation of the overlying sills occurred as growth of the CIB continued to bend the overburden. AMS data suggest sill intrusion was complex and may have persisted throughout growth of the CIB. A series of dikes, possibly ascending from the CIB, exploited the radial fractures throughout the overlying sedimentary rocks (Figure 43B, 43C). AMS data suggest dikes in the SW region intruded relatively early in rotation of the sedimentary cover, while dikes in the S-SE and E regions intruded throughout CIB growth. Cross-cutting relationships suggest that sill formation in each region may have ceased before subsequent radial dikes cut the sills. During cooling of the CIB, the contact metamorphic aureole extended out to at least the Triassic Moenkopi formation. Total construction time for Mount Hillers has been constrained to  $\leq 1$  million years (Paquette et al., 2010), while individual sheets intruded much more rapidly and probably cooled below the solidus on the order of several weeks to a few years (Saint Blanquat et al., 2011).

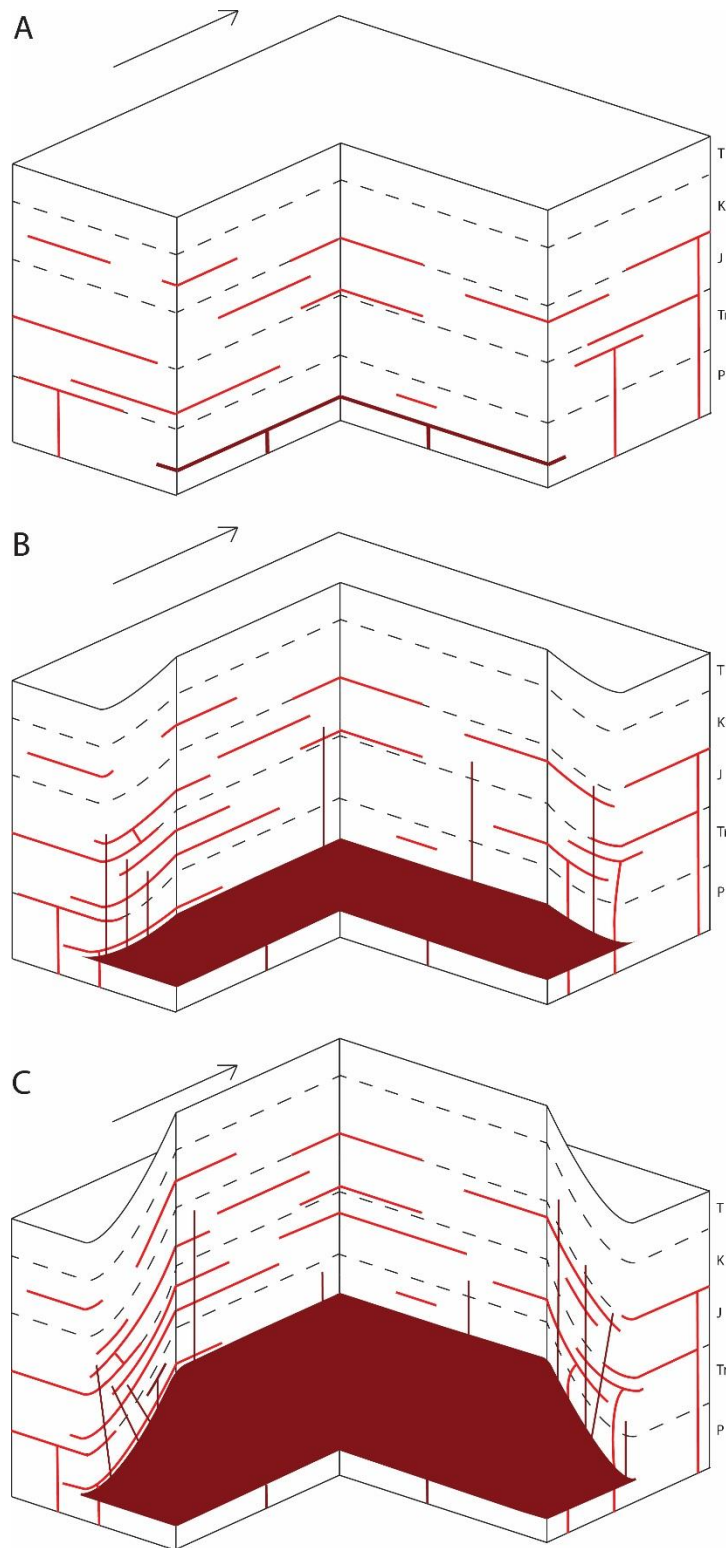


Figure 43. Schematic construction model for the intrusive sheet network on the southern margin of Mount Hillers. (A) Sills, fed by subvertical dikes, intrude the Phanerozoic sedimentary strata. The incipient CIB intrudes near the base of the Permian Cutler formation, growing over a large lateral extent. (B) The CIB begins doming the overburden as vertical growth begins. Sills continue to intrude the host rock, and radial dikes cut through both overlying sediments and sills. (C) As growth of the CIB continues, overburden is sharply bent and rotated. Late sills intrude the bent overburden, and late radial dikes remain unrotated as growth of the CIB concludes.

## Conclusions

Field observations of the sill/dike network on the southern margin of Mount Hillers show that coarse-grained sills are older than fine-grained dikes. CSD analysis on plagioclase phenocrysts indicates that sills and dikes have distinct crystallization histories. The data suggest that parental sill magma spent more time at depths conducive to plagioclase crystallization, alternating between short periods of ascent and long periods of storage at different crustal levels, while parental dike magma spent less time in storage and ascended relatively rapidly. Textural analysis on thin sections corroborates the CSD data, and trace element geochemistry also demonstrates distinctions between coarse-grained sills and fine-grained dikes. These data are interpreted as evidence for two texturally and geochemically distinct pulses of magma: (1) an older batch of relatively coarse-grained magma; and (2) a younger batch of relatively fine-grained magma.

Although often difficult to measure precisely, field fabrics of aligned hornblende phenocrysts are consistent with the subhorizontal emplacement of certain sills throughout the study area. Assuming magma flowed subparallel to the plane of intrusion, AMS data may suggest that sills intruded both before and during CIB growth and associated host rock rotation, while radial dikes may have intruded throughout host rock rotation as well.

Field observations of radial dikes and sills intruding along bedding planes show that magma commonly exploits mechanical heterogeneities in the shallow crust during ascent and emplacement. Sill thickness appears to be at least partially controlled by the rigidity of the local host rock; sills intruding incompetent host rock are consistently thicker than that sills intruding

competent host rock. Rigidity contrasts between adjacent sedimentary units and decreasing driving pressures during magma ascent may control where sill emplacement occurred.

During early stages of construction, dike-fed sills intruded subhorizontal sedimentary strata. Around the same time, the incipient CIB intruded near the base of the Permian Cutler formation. Once magma fluid pressure within the CIB exceeded the overburden weight, uplift and bending of the overburden commenced. Sills residing structurally above the growing CIB were rotated concurrently with the sedimentary host rock. Throughout growth of the CIB, sills may have continued intruding the rotated host rock. A series of dikes, possibly ascending from the CIB, exploited radial fractures in the host rock, cutting through both sedimentary and igneous overburden. During cooling of the CIB, the contact metamorphic aureole extended out to at least the Triassic Moenkopi formation. Construction of the CIB and the intrusive sheet network took up to 1 million years, while individual sheets intruded much more rapidly and probably cooled below the solidus on the order of several weeks to a few years.

## References Cited

- Allmendinger, R.W., Hauge, T.A., Hauser, E.C., Potter, C.J, Klemperer, S.L., Nelson, K.D., Knuepfer, P., and Oliver, J., 1987, Overview of the COCORP 40°N Transect, western United States: The fabric of an orogenic belt: *Geological Society of America Bulletin*, v. 98, no. 3, p. 308.
- Armienti, P., Pareschi, M.T., Innocenti, F., and Pompilio, M., 1994, Effects of magma storage and ascent on the kinetics of crystal growth: The case of the 1991-93 Mt. Etna eruption: *Contributions to Mineralogy and Petrology*, v. 115, no. 4, p. 402-414.
- Bachmann, O., Miller, C.F., and de Silva, S.L., 2007, The volcanic-plutonic connection as a stage for understanding crustal magmatism: *Journal of Volcanology and Geothermal Research*, v. 167, no. 1, p. 1-23.
- Barbey, P., 2009, Layering and schlieren in granitoids: A record of interactions between magma emplacement, crystallization and deformation in growing plutons: *Geologica Belgica*, v. 12, no. 3-4, p. 109-133.
- Bas, M.J.L., Maitre, R.W.L., Streckeisen, A., and Zanettin, B., 1986, A chemical classification of volcanic rocks based on the total alkali-silica diagram: *Journal of Petrology*, v. 27, no. 3, p. 745-750.
- Bateman, P.C., 1992, Plutonism in the central part of the Sierra Nevada batholith, California: U.S. Geological Survey Professional Paper 1483, 186 p.
- Broda, R.J., 2014, Geometry and progressive development of a shallow crustal intrusive complex, Mount Hillers, Henry Mountains, Utah [Master's Thesis]: East Carolina University, 111 p.
- Bump, A.P., 2004, Three-dimensional Laramide deformation of the Colorado Plateau: Competing stresses from the Sevier thrust belt and the flat Farallon slab: *Tectonics*, v. 23, no. 1, p. TC1008.
- Cadman, A.C., Park, R.G., Tarney, J., and Halls, H.C., 1992, Significance of anisotropy of magnetic susceptibility fabrics in Proterozoic mafic dykes, Hopedale Block, Labrador: *Tectonophysics*, v. 207, p. 303-314.
- Callot, J.-P., Geoffroy, L., Aubourg, C., Pozzi, J.P., and Mege, D., 2001, Magma flow directions of shallow dykes from the East Greenland volcanic margin inferred from magnetic fabric studies: *Tectonophysics*, v. 335, no. 3, p. 313-329.
- Cañón-Tapia, E., 2004, Anisotropy of magnetic susceptibility of lava flows and dykes: A historical account: *Geological Society of London Special Publication*, v. 238, p. 205-225.

- Cashman, K.V., and Marsh, B.D., 1988, Crystal size distribution (CSD) in rocks and the kinetics and dynamics of crystallization II: Makaopuhi lava lake: *Contributions to Mineralogy and Petrology*, v. 99, no. 3, p. 292-305.
- Coleman, D.S., Gray, W., and Glazner, A.F., 2004, Rethinking the emplacement and evolution of zoned plutons: Geochronologic evidence for incremental assembly of the Tuolumne Intrusive Suite, California: *Geology*, v. 32, no. 5, p. 433-436.
- Cruden, A.R., and Bungler, A., 2010, Emplacement dynamics of laccoliths, sills, and dykes from dimensional scaling and mechanical models: LASI 4 Conference, *Physical Geology of Subvolcanic Systems: Laccolith, Sills, and Dykes, Abstracts*, p. 15-16.
- Cruden, A.R., and McCaffrey, K.J.W., 2001, Growth of plutons by floor-subsidence: Implications for rates of emplacement, intrusion spacing and melt-extraction mechanisms: *Physics and Chemistry of the Earth, Part A: Solid Earth and Geodesy*, v. 26, no. 4-5, p. 303-315.
- de Saint-Blanquat, M., Habert, G., Horsman, E., Morgan, S.S., Tikoff, B., Launeau, P., and Gleizes, G., 2006, Mechanisms and duration of non-tectonically assisted magma emplacement in the upper crust: The Black Mesa pluton, Henry Mountains, Utah: *Tectonophysics*, v. 428, no. 1, p. 1-31.
- de Saint Blanquat, M., Horsman, E., Habert, G., Morgan, S., Vanderhaeghe, O., Law, R., and Tikoff, B., 2011, Multiscale magmatic cyclicality, duration of pluton construction, and the paradoxical relationship between tectonism and plutonism in continental arcs: *Tectonophysics*, v. 500, no. 1-4, p. 20-33.
- Doelling, H.H., 1975, *Geology and mineral resources of Garfield County, Utah: Utah Geological and Mineral Survey Bulletin 107*, 175 p.
- Dutcher, R.R., Campbell, D.L., and Thornton, C.P., 1966, Coal metamorphism and igneous intrusives in Colorado: *American Chemical Society, Advances in Chemistry*, v. 55, p. 708-723.
- Ernst, R.E., and Baragar, W.R.A., 1992, Evidence from magnetic fabric for the flow pattern of magma in the Mackenzie giant radiating dyke swarm: *Nature*, v. 356, p. 511-513.
- Ferré, E.C., Bordarier, C., and Marsh, J.S., 2002, Magma flow inferred from AMS fabrics in a layered mafic sill. Insizwa, South Africa: *Tectonophysics*, v. 354, p. 1-23.
- Fossen, H., 2010, *Structural geology: New York, Cambridge University Press*, 463 p.
- Gilbert, G.K., 1877, *Report on the geology of the Henry Mountains: U.S. Geological Survey*, 170 p.

- Glazner, A.F., and Bartley, J.M., 2006, Is stopping a volumetrically significant pluton emplacement process? *Geological Society of America Bulletin*, v. 118, no. 9-10, p. 1185-1195.
- Gwyn, N.Z., 2011, Emplacement and growth of large complex intrusions in the shallow crust, Henry Mountains, Utah [Master's Thesis]: East Carolina University, 89 p.
- Hawkesworth, C.J., and Kemp, A.I.S., 2006, Evolution of the continental crust: *Nature*, v. 443, p. 811-817.
- Higgins, M.D., 1996, Magma dynamics beneath Kameni volcano, Thera, Greece, as revealed by crystal size and shape measurements: *Journal of Volcanology and Geothermal Research*, v. 70, no. 1, p. 37-48.
- Higgins, M.D., 1998, Origin of anorthosite by textural coarsening: quantitative measurements of a natural sequence of textural development: *Journal of Petrology*, v. 39, no. 7, p. 1307-1323.
- Higgins, M.D., 2000, Measurement of crystal size distributions: *American Mineralogist*, v. 85, no. 9, p. 1105-1116.
- Higgins, M.D., and Roberge, J., 2003, Crystal size distribution of plagioclase and amphibole from Soufrière Hills Volcano, Montserrat: Evidence for dynamic crystallization-textural coarsening cycle: *Journal of Petrology*, v. 44, no. 8, p. 1401-1411.
- Horsman, E., Morgan, S., de Saint-Blanquat, M., Habert, G., Nugent, A., Hunter, R.A., and Tikoff, B., 2010, Emplacement and assembly of shallow intrusions from multiple magma pulses, Henry Mountains, Utah: *Earth and Environmental Science Transactions of the Royal Society of Edinburgh*, v. 100, p. 117-132.
- Horsman, E., Tikoff, B., and Morgan, S., 2005, Emplacement-related fabric and multiple sheets in the Maiden Creek sill, Henry Mountains, Utah, USA: *Journal of Structural Geology*, v. 27, no. 8, p. 1426-1444.
- Hunt, C.B., Averitt, P., and Miller, R.L., 1953, Geology and geography of the Henry Mountains region, Utah: *US Geological Survey Professional Paper 228*, 234 p.
- Hurlbut, C.S., and Griggs, D.T., 1939, Igneous rocks of the Highwood Mountains, Montana: *Geological Society of America Bulletin*, v. 50, p. 1043-1112.
- Jackson, M.D., and Pollard, D.D., 1988, The laccolith-stock controversy - new results from the southern Henry Mountains, Utah: *Geological Society of America Bulletin*, v. 100, no. 1, p. 117-139.
- Jackson, M.D., and Pollard, D.D., 1990, Flexure and faulting of sedimentary host rocks during growth of igneous domes, Henry Mountains, Utah: *Journal of Structural Geology*, v. 12, no. 2, p. 185-206.

- Johnson, A.M., and Pollard, D.D., 1973, Mechanics of growth of some laccolithic intrusions in the Henry Mountains, Utah, I, *Tectonophysics*, v. 18, 261-309.
- Kavanagh, J.L., Menand, T., and Sparks, R.S.J., 2006, An experimental investigation of sill formation and propagation in layered elastic media: *Earth and Planetary Science Letters*, v. 245, no. 3, p. 799-813.
- Knight, M.D., and Walker, G.P.L., 1988, Magma flow directions in dikes of the Koolau complex, Oahu, determined from magnetic fabric studies: *Journal of Geophysical Research*, v. 93, no. 5, p. 4301-4319.
- Le Corvec, N., Menand, T., and Lindsay, J., 2013, Interaction of ascending magma with pre-existing crustal fractures in monogenetic basaltic volcanism: An experimental approach: *Journal of Geophysical Research B: Solid Earth*, v. 118, no. 3, p. 968-984.
- Marsh, B.D., 1988, Crystal size distribution (CSD) in rocks and the kinetics and dynamics of crystallization - I. Theory: *Contributions to Mineralogy and Petrology*, v. 99, no. 3, p. 277-291.
- McDonough, W.F., and Sun, S.-s., 1995, The composition of the Earth: *Chemical Geology*, v. 120, no. 3, p. 223-253.
- KcKay, G.A., 1989, Partitioning of rare earth elements between major silicate minerals and basaltic melts: *Reviews in Mineralogy and Geochemistry*, v. 21, p. 45-77.
- Menand, T., 2008, The mechanics and dynamics of sills in layered elastic rocks and their implications for the growth of laccoliths and other igneous complexes: *Earth and Planetary Science Letters*, v. 267, no. 1, p. 93-99.
- Menand, T., 2011, Physical controls and depth of emplacement of igneous bodies: A review: *Tectonophysics*, v. 500, no. 1, p. 11-19.
- Mock, A., Jerram, D.A., and Breikreuz, C., 2003, Using quantitative textural analysis to understand the emplacement of shallow-level rhyolitic laccoliths - A case study from the Halle Volcanic Complex, Germany: *Journal of Petrology*, v. 44, no. 5, p. 833-849.
- Montaser, A., 1998, *Inductively coupled plasma mass spectrometry*: New York, Wiley, 967 p.
- Morgan, D.J., and Jerram, D.A., 2006, On estimating crystal shape for crystal size distribution analysis: *Journal of Volcanology and Geothermal Research*, v. 154, no. 1, p. 1-7.
- Morgan, S., Stanik, A., Horsman, E., Tikoff, B., de Saint Blanquat, M., and Habert, G., 2008, Emplacement of multiple magma sheets and wall rock deformation: Trachyte Mesa intrusion, Henry Mountains, Utah: *Journal of Structural Geology*, v. 30, no. 4, p. 491-512.

- Muirhead, J.D., Airoidi, G., Rowland, J.V., and White, J.D.L., 2012, Interconnected sills and inclined sheet intrusions control shallow magma transport in the Ferrar large igneous province, Antarctica: *Geological Society of America Bulletin*, v. 124, no. 1-2, p. 162-180.
- Nelson, S.T., and Davidson, J.P., 1993, Interactions between mantle-derived magmas and mafic crust, Henry Mountains, Utah: *Journal of Geophysical Research*, v. 98, no. 2, p. 1837-1852.
- Nelson, S.T., Davidson, J.P., and Sullivan, K.R., 1992, New age determinations of central Colorado Plateau laccoliths, Utah: Recognizing disturbed K-Ar systematics and re-evaluating tectonomagmatic relationships: *Geological Society of America Bulletin*, v. 104, no. 12, p. 1547-1560.
- Neres, M., Bouchez, J.L., Terrinha, P., Font, E., Moreira, M., Miranda, R., Launeau, P., and Carvalho, C., 2014, Magnetic fabric in a Cretaceous sill (Foz da Fonte, Portugal): flow model and implications for regional magmatism: *Geophysical Journal International*, v. 199, p. 78-101.
- Paquette, J.-L., de Saint Blanquat, M., Delpech, G., Horsman, E., and Morgan, S., 2010, LA-ICPMS U-Pb zircon dating of Mount Hillers laccolite and satellite intrusions: rapid emplacement and large Proterozoic inheritance: LASI 4 Conference, *Physical Geology of Subvolcanic Systems: Laccolith, Sills, and Dykes, Abstracts*, p. 41-42.
- Park, J.K., Tanczyk, E.I., and Desbarats, A., 1988, Magnetic fabric and its significance in the 1400 Ma Mealy diabase dykes of Labrador, Canada: *Journal of Geophysical Research*, v. 93, p. 13689-13704.
- Parsons, T., Sleep, N.H., and Thompson, G.A., 1992, Host rock rheology controls on the emplacement of tabular intrusions: implications for underplating of extending crust: *Tectonics*, v. 11, no. 6, p. 1348-1356.
- Paterson, S.R., Fowler, T.K., Schmidt, K.L., Yoshinobu, A.S., Yuan, E.S., and Miller, R.B., 1998, Interpreting magmatic fabric patterns in plutons, *Lithos*, v. 44, p. 53-82.
- Petford, N., Cruden, A.R., and McCaffrey, K.J.W., 2000, Granite magma formation, transport and emplacement in the Earth's crust: *Nature*, v. 408, p. 669-673.
- Petford, N., Kerr, R.C., and Lister, J.R., 1993, Dike transport of granitoid magmas: *Geology*, v. 21, no. 9, p. 845-848.
- Petford, N., Lister, J.R., and Kerr, R.C., 1994, The ascent of felsic magmas in dykes: *Lithos*, v. 32, no. 1, p. 161-168.
- Pollard, D.D., and Johnson, A.M., 1973, Mechanics of growth of some laccolithic intrusions in the Henry Mountains, Utah, II: *Tectonophysics*, v. 18, p. 311-354.

- Pollard, D.D., Muller, O.H., and Dockstader, D.R., 1975, The form and growth of fingered sheet intrusions: *Geological Society of America Bulletin*, v. 86, no. 3, p. 351-363.
- Raposo, M.I.B., and Ernesto, M., 1995, Anisotropy of magnetic susceptibility in the Ponta Grossa dyke swarm (Brazil) and its relationship with magma flow direction: *Physics of the Earth and Planetary Interiors*, v. 87, p. 183-196.
- Rocchi, S., Westerman, D.S., Dini, A., and Farina, F., 2010, Intrusive sheets and sheeted intrusions at Elba Island, Italy: *Geosphere*, v. 6, no. 3, p. 225-236.
- Rochette, P., Jackson, M., and Aubourg, C., 1992, Rock magnetism and the interpretation of anisotropy of magnetic susceptibility: *Reviews of Geophysics*, v. 30, no. 3, p. 209-226.
- Rochette, P., Jenatton, L., Dupuy, C., Boudier, F., and Reuber, I., 1991, Diabase dikes emplacement in the Oman Ophiolite: a magnetic fabric study with reference to geochemistry, *in* Peters, T., Nicolas, A., and Coleman, R.G., eds., *Ophiolite genesis and evolution of the oceanic lithosphere: Ministry of petroleum and minerals, Sultanate of Oman*, p. 55-82.
- Stevenson, C.T.E., Owens, W.H., and Hutton, D.H.W., 2007, Flow lobes in granite: The determination of magma flow direction in the Trawenagh Bay Granite, northwestern Ireland, using anisotropy of magnetic susceptibility: *Geological Society of America Bulletin*, v. 119, no. 11-12, p. 1368-1386.
- Thompson, G.A., and Zoback, M.L., 1979, Regional geophysics of the Colorado Plateau: *Tectonophysics*, v. 61, no. 1, p. 149-181.
- Thomson, K., and Hutton, D., 2004, Geometry and growth of sill complexes: insights using 3D seismic from the North Rockall Trough: *Bulletin of Volcanology*, v. 66, no. 4, p. 364-375.
- Tweto, O., 1951, Form and structure of sills near Pando, Colorado: *Geological Society of America Bulletin*, v. 62, p. 507-532.
- Varga, R.J., Gee, J., Staudigel, H., and Tauxe, L., 1998, Dike surface lineations as magma flow indicators within the sheeted dike complex of the Troodos Ophiolite, Cyprus: *Journal of Geophysical Research*, v. 103, p. 5241-5256.
- Vigneresse, J.L., and Clemens, J.D., 2000, Granitic magma ascent and emplacement: neither diapirism nor neutral buoyancy: *Geological Society of London Special Publication*, v. 174, no. 1, p. 1-19.
- Yoshinobu, A.S., Okaya, D.A., and Paterson, S.R., 1998, Modeling the thermal evolution of fault-controlled magma emplacement models: implications for the solidification of granitoid plutons: *Journal of Structural Geology*, v. 20, no. 9, p. 1205-1218.

## Appendix A      Measurements of Sill Thickness

Sills intruding competent roof/floor host rocks			Sills intruding partially incompetent roof/floor host rocks		
Station #	Host rock intruded	Thickness (m)	Station #	Host rock intruded	Thickness (m)
-	Entrada/Carmel	1-2	CC105	Summerville	10-15
-	Entrada	5-8	CC118	Chinle/Moenkopi	8-12
CC41	Navajo	3-5	CC113	Chinle	12-18
CC120	Wingate	10	CC44	Entrada/Summerville	10-12
CC131	Entrada	10	-	Chinle/Moenkopi	10
-	Navajo	5	-	Summerville	12-15
	Average thickness	6		Average Thickness	12

## Appendix B Crystal Size Distribution Data

CSD data for hornblende phenocrysts

HORNBLLENDE						
Fine-grained						
Sample #	CC7a		CC2		CC5	
	Bin Size	(ln)Pop. Density	Bin Size	(ln)Pop. Density	Bin Size	(ln)Pop. Density
	2.0129	-6.8369	3.1903	-9.8696	5.0563	-11.8451
	1.2701	-4.5007	2.0129	-6.5345	3.1903	-8.5378
	0.8014	-4.0235	1.2701	-4.1269	2.0129	-5.3439
			0.8014	-3.4766	1.2701	-3.466
					0.8014	-3.6258
Medium-grained						
Sample #	CC16		CC63		CC87	
	Bin Size	(ln)Pop. Density	Bin Size	(ln)Pop. Density	Bin Size	(ln)Pop. Density
	3.1903	-10.2487	5.0563	-11.7844	5.0563	-12.0538
	2.0129	-6.3902	3.1903	-9.5138	3.1903	-9.2097
	1.2701	-4.5383	2.0129	-6.529	2.0129	-6.5269
	0.8014	-4.1093	1.2701	-4.2596	1.2701	-4.0679
			0.8014	-3.98	0.8014	-3.7856
Coarse-grained						
Sample #	CC9a		CC65		CC85	
	Bin Size	(ln)Pop. Density	Bin Size	(ln)Pop. Density	Bin Size	(ln)Pop. Density
	3.1903	-8.7517	3.1903	-8.4347	2.0129	-8.2306
	2.0129	-5.7258	2.0129	-5.5133	1.2701	-5.3478
	1.2701	-3.4961	1.2701	-3.5075	0.8014	-4.9839
	0.8014	-3.0627	0.8014	-3.2093		

CSD data for plagioclase phenocrysts

PLAGIOCLASE						
Fine-grained						
Sample #	CC7a		CC2		CC5	
	Bin Size	(ln)Pop. Density	Bin Size	(ln)Pop. Density	Bin Size	(ln)Pop. Density
	5.0563	-8.8136	8.0137	-12.7733	5.0563	-10.4494
	3.1903	-6.3744	5.0563	-9.2969	3.1903	-7.5678
	2.0129	-4.0385	3.1903	-6.3845	2.0129	-4.8146
	1.2701	-2.7611	2.0129	-4.3327	1.2701	-3.372
			1.2701	-3.0975		
Medium-grained						
Sample #	CC16		CC63		CC87	
	Bin Size	(ln)Pop. Density	Bin Size	(ln)Pop. Density	Bin Size	(ln)Pop. Density
	8.0137	-11.6953	8.0137	-12.7038	5.0563	-10.253
	5.0563	-8.3306	5.0563	-8.9584	3.1903	-6.8323
	3.1903	-6.1683	3.1903	-6.3466	2.0129	-4.8547
	2.0129	-4.7481	2.0129	-4.4276	1.2701	-3.6962
	1.2701	-3.5958	1.2701	-3.3216		
Coarse-grained						
Sample #	CC9a		CC65		CC85	
	Bin Size	(ln)Pop. Density	Bin Size	(ln)Pop. Density	Bin Size	(ln)Pop. Density
	20.1294	-15.0272	20.1294	-14.5559	12.7008	-12.0513
	12.7008	-12.7567	12.7008	-12.0572	8.0137	-9.8857
	8.0137	-10.0343	8.0137	-10.3017	5.0563	-8.3673
	5.0563	-7.8423	5.0563	-8.1345	3.1903	-6.819
	3.1903	-6.7408	3.1903	-6.6566	2.0129	-5.6909
	2.0129	-5.8982	2.0129	-5.3063	1.2701	-4.8192
	1.2701	-5.0028	1.2701	-4.1157		

CSD data for plagioclase phenocrysts, continued

PLAGIOCLASE						
Fine-grained						
Sample #	CC115		CC154		CC156	
	Bin Size	(ln)Pop. Density	Bin Size	(ln)Pop. Density	Bin Size	(ln)Pop. Density
	3.1903	-6.8702	5.0563	-11.4709	5.0563	-11.5425
	2.0129	-4.2278	3.1903	-8.9662	3.1903	-7.4084
	1.2701	-2.2219	2.0129	-5.6343	2.0129	-5.0339
			1.2701	-3.1183	1.2701	-2.9546
Medium-grained						
Sample #	CC98		CC102			
	Bin Size	(ln)Pop. Density	Bin Size	(ln)Pop. Density		
	8.0137	-12.4694	8.0137	-11.6946		
	5.0563	-9.9682	5.0563	-8.5346		
	3.1903	-7.4401	3.1903	-6.0279		
	2.0129	-5.2745	2.0129	-4.4796		
	1.2701	-3.581	1.2701	-3.0744		
Coarse-grained						
Sample #	CC118		CC131		CC163	
	Bin Size	(ln)Pop. Density	Bin Size	(ln)Pop. Density	Bin Size	(ln)Pop. Density
	20.1294	-14.1737	12.7008	-14.1189	12.7008	-11.9812
	12.7008	-12.2063	8.0137	-10.2095	8.0137	-10.9452
	8.0137	-10.4615	5.0563	-8.563	5.0563	-8.0266
	5.0563	-7.9529	3.1903	-7.1012	3.1903	-6.7289
	3.1903	-6.8662	2.0129	-6.1222	2.0129	-5.6301
	2.0129	-5.9528	1.2701	-5.3882	1.2701	-4.4626
	1.2701	-4.3913				

## Appendix C      Geochemistry Data

Whole-rock major element geochemistry data, dikes

		<b>Dikes</b>						
		CC2	CC5	CC14	CC50	CC86	CC88	
Major elements (wt %)								AVG
SiO <sub>2</sub>		59.33	58.96	59.18	60.13	62.42	60.29	60.05
Al <sub>2</sub> O <sub>3</sub>		17.50	17.83	17.81	18.00	18.01	17.77	17.82
TiO <sub>2</sub>		0.54	0.57	0.56	0.48	0.42	0.54	0.52
Fe <sub>2</sub> O <sub>3</sub> (tot)		5.07	5.45	5.29	4.83	4.43	5.63	5.12
MnO		0.17	0.17	0.17	0.14	0.16	0.14	0.16
MgO		1.67	1.60	1.37	1.14	1.04	1.58	1.40
CaO		4.98	5.73	5.76	5.30	4.78	5.51	5.34
Na <sub>2</sub> O		5.03	4.73	4.12	4.11	4.78	4.92	4.62
K <sub>2</sub> O		2.2	2.2	2.4	2.3	1.7	2.1	2.1
P <sub>2</sub> O <sub>5</sub>		0.2	0.2	0.2	0.2	0.2	0.2	0.2
LOI		3.0	2.2	2.8	3.0	1.9	1.0	2.3
Total		99.69	99.65	99.64	99.67	99.71	99.67	99.67

Whole-rock major element geochemistry data, sills

		<b>Sills</b>						
		CC29	CC57a	CC43	CC65	CC70	CC85	
Major elements (wt %)								AVG
SiO <sub>2</sub>		61.58	58.23	59.03	60.91	61.59	59.06	60.07
Al <sub>2</sub> O <sub>3</sub>		18.14	17.68	17.81	18.07	17.96	17.56	17.87
TiO <sub>2</sub>		0.48	0.63	0.59	0.48	0.45	0.47	0.52
Fe <sub>2</sub> O <sub>3</sub> (tot)		5.03	6.35	5.74	4.71	4.64	4.90	5.23
MnO		0.17	0.17	0.17	0.13	0.14	0.13	0.15
MgO		1.20	1.87	1.65	1.46	1.26	1.44	1.48
CaO		4.71	6.43	5.53	4.52	5.43	5.82	5.41
Na <sub>2</sub> O		4.71	4.23	4.87	6.38	4.88	4.31	4.90
K <sub>2</sub> O		2.1	1.8	1.6	1.3	1.9	1.7	1.7
P <sub>2</sub> O <sub>5</sub>		0.2	0.3	0.2	0.2	0.2	0.2	0.2
LOI		1.4	2.0	2.4	1.6	1.2	4.1	2.1
Total		99.70	99.68	99.65	99.71	99.68	99.70	99.69

Whole-rock trace element geochemistry data, dikes

		Dikes						
		CC2	CC5	CC14	CC50	CC86	CC88	
Trace elements (ppm)								AVG
Rb		31.2	32.8	34.9	33.8	22.2	28.5	30.6
Sr		800.2	954.2	1009.4	913.4	908.7	978.2	927.4
Zr		149.2	150.3	161.4	152.6	142.2	143.4	149.9
V		68.0	79.0	60.0	46.0	42.0	64.0	59.8
Ba		1050.0	1104.0	1231.0	1154.0	908.0	1109.0	1092.7
Y		30.4	32.3	33.6	27.9	23.7	25.6	28.9
Nb		6.5	6.9	6.7	5.5	6.1	6.3	6.3
Zn		71.0	85.0	86.0	79.0	103.0	46.0	78.3
Pb		6.0	12.7	1.8	4.3	2.4	3.7	5.2
Th		7.8	7.9	8.5	5.1	4.2	5.3	6.5
Hf		4.3	4.5	4.6	3.8	3.5	3.5	4.0
Ta		0.3	0.3	0.3	0.4	0.3	0.3	0.3
La		41.7	41.5	39.8	25.7	22.0	26.7	32.9
Ce		86.4	87.8	88.6	55.6	46.2	57.6	70.4
Pr		10.5	10.3	10.5	6.7	5.7	6.9	8.4
Nd		37.3	39.4	39.9	27.9	22.0	28.8	32.6
Sm		7.5	7.2	7.5	5.6	4.8	5.5	6.4
Eu		2.1	2.2	2.4	1.8	1.6	1.9	2.0
Gd		6.1	6.8	7.2	5.3	4.8	5.7	6.0
Tb		0.8	0.9	0.9	0.7	0.7	0.8	0.8
Dy		5.4	5.7	6.3	5.0	4.2	4.9	5.3
Ho		1.0	1.1	1.1	0.9	0.8	0.9	1.0
Er		2.9	2.9	3.4	2.8	2.3	2.6	2.8
Tm		0.5	0.5	0.5	0.4	0.4	0.4	0.4
Yb		3.2	3.2	3.1	2.6	2.5	2.7	2.9
Lu		0.5	0.4	0.5	0.4	0.3	0.4	0.4

Whole-rock trace element geochemistry data, dikes, continued

	Dikes							
	CC2	CC5	CC14	CC50	CC86	CC88		
Trace elements (ppm)							AVG	
Be	<1	<1	<1	<1	<1	<1	-	
S							-	
Sc	7.0	8.0	7.0	6.0	5.0	8.0	6.8	
Cr	<20	<20	<20	<20	20.0	30.0	-	
Co	5.3	6.7	5.2	5.1	4.0	6.7	5.5	
Ni	<20	<20	<20	<20	<20	<20	-	
Cu	5.0	7.3	1.8	1.6	2.0	72.0	15.0	
Ga	18.9	19.4	20.1	20.9	19.5	19.8	19.8	
Ge								
As	7.2	3.5	1.7	1.2	3.2	1.8	3.1	
Se	<0.5	<0.5	<0.5	<0.5	<0.5	<0.5	-	
Br							-	
Mo	0.2	0.2	0.2	0.3	0.2	0.2	0.2	
Ag	<0.1	<0.1	<0.1	<0.1	<0.1	<0.1	-	
Cd	<0.1	<0.1	<0.1	<0.1	<0.1	<0.1	-	
In							-	
Sn	1.0	2.0	1.0	2.0	<1	<1	-	
Sb	<0.1	0.1	<0.1	0.1	<0.1	<0.1	-	
Cs	2.3	1.4	0.9	2.4	0.7	0.6	1.4	
Tl	<0.1	<0.1	<0.1	<0.1	<0.1	<0.1	-	
W	<0.5	0.8	<0.5	<0.5	0.5	<0.5	0.7	
Ir							-	
Au (ppb)	1.3	1.2	0.8	<0.5	<0.5	2.3	-	
Hg	<0.01	<0.01	<0.01	<0.01	<0.01	<0.01	-	
Bi	<0.1	<0.1	<0.1	<0.1	<0.1	<0.1	-	
U	1.9	1.8	1.5	1.6	1.0	1.5	1.6	

Whole-rock trace element geochemistry data, sills

	Sills							
	CC29	CC57a	CC43	CC65	CC70	CC85		
Trace elements (ppm)							AVG	
Rb	25.8	27.2	18.8	14.2	30.2	24.5	23.5	
Sr	877.1	1008.2	962.0	945.7	1044.9	909.2	957.9	
Zr	143.2	138.8	146.1	134.6	141.2	138.2	140.4	
V	55.0	80.0	71.0	57.0	54.0	54.0	61.8	
Ba	960.0	950.0	1259.0	849.0	1011.0	864.0	982.2	
Y	24.3	30.5	34.3	25.9	22.8	24.6	27.1	
Nb	6.4	6.2	6.2	5.7	5.8	5.1	5.9	
Zn	66.0	54.0	57.0	44.0	48.0	101.0	61.7	
Pb	9.7	6.9	9.4	6.4	6.7	5.5	7.4	
Th	4.6	5.6	4.7	4.9	4.7	4.7	4.9	
Hf	3.8	3.4	4.2	3.6	3.9	3.0	3.7	
Ta	0.4	0.3	0.4	0.4	0.4	0.3	0.4	
La	23.0	27.6	26.4	21.3	21.7	23.4	23.9	
Ce	48.0	61.0	57.1	46.3	47.8	49.7	51.7	
Pr	5.8	7.4	7.3	5.8	5.7	6.1	6.3	
Nd	23.1	30.5	28.5	23.5	23.9	26.2	26.0	
Sm	5.1	6.2	6.3	5.0	4.8	5.3	5.4	
Eu	1.7	2.0	2.1	1.7	1.6	1.6	1.8	
Gd	4.9	6.0	6.5	5.1	4.9	5.4	5.5	
Tb	0.7	0.8	0.9	0.7	0.7	0.7	0.7	
Dy	4.4	4.9	6.1	4.6	4.0	4.4	4.7	
Ho	0.8	1.1	1.1	1.0	0.8	0.9	0.9	
Er	2.6	3.1	3.6	2.6	2.2	2.7	2.8	
Tm	0.4	0.5	0.5	0.4	0.3	0.4	0.4	
Yb	2.5	3.4	3.3	2.7	2.5	2.6	2.8	
Lu	0.4	0.4	0.5	0.4	0.3	0.3	0.4	

Whole-rock trace element geochemistry data, sills, continued

	Sills							AVG
	CC29	CC57a	CC43	CC65	CC70	CC85		
Trace elements (ppm)								
Be	<1	<1	<1	<1	1.0	2.0	-	
S							-	
Sc	6.0	10.0	9.0	7.0	6.0	7.0	7.5	
Cr	<20	20.0	<20	40.0	<20	30.0	-	
Co	5.7	8.7	7.2	5.5	5.8	5.8	6.5	
Ni	<20	<20	<20	<20	<20	<20	-	
Cu	15.1	10.5	17.6	2.9	8.5	6.3	10.2	
Ga	19.7	19.1	19.6	18.7	19.4	19.1	19.3	
Ge							-	
As	6.7	1.0	2.8	1.9	1.3	1.2	2.5	
Se	<0.5	<0.5	<0.5	<0.5	<0.5	<0.5	-	
Br							-	
Mo	0.4	0.2	0.2	0.1	0.2	0.2	0.2	
Ag	<0.1	<0.1	<0.1	<0.1	<0.1	<0.1	-	
Cd	<0.1	<0.1	<0.1	<0.1	<0.1	<0.1	-	
In							-	
Sn	<1	1.0	1.0	1.0	1.0	1.0	-	
Sb	0.1	<0.1	<0.1	<0.1	0.1	<0.1	-	
Cs	1.0	0.6	0.7	0.5	0.5	0.7	0.7	
Tl	<0.1	<0.1	<0.1	<0.1	<0.1	<0.1	-	
W	<0.5	<0.5	<0.5	<0.5	<0.5	<0.5	-	
Ir							-	
Au (ppb)	0.6	<0.5	0.6	<0.5	<0.5	0.8	-	
Hg	<0.01	<0.01	<0.01	<0.01	<0.01	<0.01	-	
Bi	0.3	<0.1	<0.1	<0.1	<0.1	<0.1	-	
U	1.4	1.4	1.3	1.6	1.6	1.7	1.5	

## Appendix D      Anisotropy of Magnetic Susceptibility Data

AMS data, dikes

Name	UTM E	UTM N	Num.	K <sub>m</sub> (SI)	K <sub>m</sub> 1 $\sigma$ (SI)	K1	K2	K3
Zone 12N (NAD 83)								
CC2	528202	4190246	6	0.032700	0.000514	1.013	1.003	0.984
CC3b	528052	4190362	6	0.034100	0.000495	1.014	1.003	0.983
CC5	527957	4190433	6	0.033100	0.000581	1.009	1.001	0.990
CC7a	527960	4190589	6	0.038000	0.001210	1.011	1.001	0.988
CC10a	527626	4190779	5	0.031800	0.000714	1.024	1.002	0.974
CC12	527371	4190985	6	0.029200	0.001970	1.008	1.005	0.987
CC14	527220	4191090	6	0.036900	0.001640	1.015	1.013	0.973
CC49	529513	4191989	6	0.033000	0.001180	1.008	1.004	0.988
CC50	529529	4192054	6	0.037900	0.000672	1.007	1.005	0.988
CC91b	525135	4191719	6	0.033900	0.001800	1.010	0.996	0.994
CC94	526277	4192353	6	0.021000	0.002620	1.009	1.001	0.990
CC15	527311	4191053	6	0.033900	0.000858	1.025	0.999	0.977
CC52	529250	4192111	6	0.008210	0.000249	1.014	1.002	0.984
CC55	530084	4192465	6	0.022800	0.000241	1.011	0.997	0.991
CC57b	530084	4192315	6	0.022400	0.001200	1.008	1.003	0.990
CC81a	525382	4190782	6	0.031100	0.000770	1.008	1.000	0.992
CC83	525007	4190538	6	0.027900	0.001080	1.006	1.002	0.992
CC86	525167	4190716	6	0.030600	0.001150	1.010	0.999	0.991
CC87	525183	4191058	6	0.012700	0.001210	1.019	1.002	0.979
CC88	525399	4191064	6	0.012800	0.000443	1.023	1.001	0.976
CC61	529899	4192463	6	0.026000	0.000282	1.008	1.000	0.992
CC52	529250	4192111	6	0.008210	0.000249	1.014	1.002	0.984
CC102	528813	4190518	5	0.012700	0.000247	1.011	1.006	0.982
CC108	528850	4190024	6	0.027100	0.000830	1.010	1.000	0.990
CC133a	526393	4190287	5	0.017100	0.002120	1.006	0.999	0.995
CC151	527778	4190436	5	0.025500	0.004210	1.018	0.996	0.986
CC154	527907	4190245	6	0.026400	0.001020	1.012	0.999	0.989
CC155	527967	4190219	6	0.028000	0.005050	1.008	1.001	0.992
CC157	528109	4190008	5	0.028900	0.000764	1.017	1.001	0.982
CC160a	526255	4190485	6	0.029900	0.001030	1.012	1.006	0.982
			AVG	0.026461				

AMS data, dikes, continued

Name	K1				K2				K3			
	decl.	incl.	$\alpha_{95}$ max	$\alpha_{95}$ min	decl.	incl.	$\alpha_{95}$ max	$\alpha_{95}$ min	decl.	incl.	$\alpha_{95}$ max	$\alpha_{95}$ min
CC2	123.9	75.1	7.0	2.1	318.1	14.4	7.6	2.7	227.2	3.5	4.3	1.8
CC3b	147.4	67.3	4.0	1.7	291.2	18.6	3.6	2.8	25.5	12.5	3.0	2.4
CC5	280.0	61.8	3.0	2.0	171.3	9.7	3.0	1.6	76.4	26.2	2.9	1.9
CC7a	25.2	26.0	4.8	1.9	122.2	14.0	5.6	4.3	237.8	60.0	5.4	1.3
CC10a	158.0	0.5	5.5	2.4	249.4	69.8	4.7	3.1	67.7	20.2	4.2	2.5
CC12	338.2	53.1	28.3	3.3	139.4	35.5	28.3	3.1	235.9	9.1	4.0	3.0
CC14	339.9	34.5	71.4	1.9	234.7	20.8	71.4	1.2	119.7	48.0	10.9	0.9
CC49	203.2	85.9	14.8	2.8	310.5	1.2	14.9	2.4	40.6	3.9	4.8	2.5
CC50	22.0	9.9	30.5	2.9	249.7	75.5	30.4	2.6	113.8	10.5	3.4	2.6
CC91b	47.0	2.3	8.1	2.9	137.9	21.1	34.0	5.2	311.1	68.8	33.9	6.5
CC94	306.0	46.6	25.6	4.1	60.1	21.1	26.7	6.7	166.2	35.8	13.8	4.3
CC15	207.6	27.6	3.8	1.9	300.4	5.4	5.0	3.3	40.7	61.8	4.7	1.7
CC52	142.0	65.8	9.6	5.2	25.8	11.2	11.5	8.2	291.4	21.2	12.4	5.2
CC55	280.0	21.9	2.4	0.7	187.0	7.5	5.2	1.6	79.2	66.7	5.1	1.4
CC57b	196.5	11.8	17.1	1.9	290.6	19.0	17.1	3.0	76.4	67.4	3.0	2.0
CC81a	189.3	19.7	18.0	4.6	294.7	36.6	17.9	9.6	76.9	46.7	10.0	4.7
CC83	35.1	2.0	29.8	7.1	305.1	0.4	29.5	9.3	203.8	88.0	11.5	5.5
CC86	160.0	10.1	8.9	0.8	62.9	35.0	13.3	8.3	263.8	53.1	13.0	1.0
CC87	86.7	22.8	11.5	1.6	342.0	31.1	11.4	5.4	206.5	49.8	5.5	2.1
CC88	69.6	33.2	3.6	2.0	202.5	46.2	4.4	1.8	321.8	25.1	5.3	1.3
CC61	330.1	37.6	8.3	3.1	176.4	49.3	9.2	6.2	70.6	13.3	8.3	4.6
CC52	142.0	65.8	9.6	5.2	25.8	11.2	11.5	8.2	291.4	21.2	12.4	5.2
CC102	353.2	32.3	19.8	3.0	110.9	36.3	20.4	3.0	234.7	37.1	10.2	2.8
CC108	7.7	47.0	11.5	2.6	246.3	25.9	12.6	10.3	138.9	31.6	12.0	3.4
CC133a	303.4	30.1	15.5	3.1	192.2	32.0	15.2	2.1	66.2	43.1	4.6	1.4
CC151	3.0	38.9	4.9	2.9	116.2	26.0	50.1	2.6	230.4	40.1	50.1	2.5
CC154	326.5	84.1	7.4	1.7	147.0	5.9	7.6	5.3	57.0	0.0	6.1	2.1
CC155	301.5	18.4	19.3	4.7	201.9	26.6	17.3	7.0	62.0	56.8	12.4	7.2
CC157	315.6	18.2	4.9	2.3	204.9	46.9	4.9	4.0	60.2	37.4	4.5	1.3
CC160a	241.2	16.7	5.1	1.5	333.0	6.0	5.2	1.3	82.0	72.2	1.8	1.4

AMS data, dikes, continued

<b>Name</b>	<b>L</b>	<b>F</b>	<b>P<sub>j</sub></b>	<b>T</b>
CC2	1.011	1.019	1.031	0.285
CC3b	1.011	1.021	1.033	0.299
CC5	1.008	1.012	1.020	0.183
CC7a	1.010	1.013	1.023	0.090
CC10a	1.022	1.030	1.053	0.133
CC12	1.005	1.017	1.024	0.555
CC14	1.014	1.037	1.054	0.510
CC49	1.004	1.016	1.021	0.556
CC50	1.004	1.017	1.023	0.619
CC91b	1.014	1.004	1.019	-0.544
CC94	1.010	1.012	1.023	0.071
CC15	1.026	1.023	1.050	-0.072
CC52	1.012	1.019	1.032	0.216
CC55	1.014	1.006	1.021	-0.394
CC57b	1.006	1.013	1.019	0.462
CC81a	1.009	1.008	1.018	-0.053
CC83	1.007	1.009	1.017	0.157
CC86	1.012	1.009	1.021	-0.145
CC87	1.018	1.024	1.042	0.150
CC88	1.022	1.026	1.048	0.075
CC61	1.009	1.008	1.017	-0.027
CC52	1.012	1.019	1.032	0.216
CC102	1.005	1.025	1.033	0.635
CC108	1.010	1.011	1.021	0.060
CC133a	1.007	1.004	1.012	-0.246
CC151	1.018	1.020	1.039	0.071
CC154	1.013	1.011	1.025	-0.092
CC155	1.008	1.009	1.017	0.022
CC157	1.016	1.019	1.036	0.083
CC160a	1.007	1.025	1.033	0.576
AVG	1.011	1.016	1.029	0.148

AMS data, sills

Sample	UTM E	UTM N	Num.	K <sub>m</sub> (SI)	K <sub>m</sub> 1 $\sigma$ (SI)	K1	K2	K3
	Zone 12N (NAD 83)							
CC3a	528052	4190362	6	0.014900	0.001900	1.012	0.999	0.989
CC7b	527960	4190589	6	0.005240	0.000224	1.023	1.002	0.975
CC9a	527791	4190670	7	0.016000	0.000215	1.011	1.003	0.987
CC9b	527791	4190670	6	0.018100	0.000438	1.009	1.002	0.989
CC36	529735	4190875	6	0.005630	0.000163	1.011	1.002	0.987
CC37	529645	4191169	6	0.010300	0.000843	1.011	1.001	0.987
CC41	529497	4191561	6	0.025100	0.000871	1.014	0.998	0.988
CC43	529734	4191456	6	0.033700	0.000833	1.008	0.999	0.994
CC45	529818	4191439	6	0.033400	0.001230	1.006	1.001	0.993
CC46a	529818	4191439	4	0.035900	0.013300	1.013	0.997	0.990
CC60	529976	4192451	6	0.003560	0.000148	1.010	1.001	0.988
CC65	525351	4190150	6	0.014300	0.000641	1.012	0.997	0.991
CC67	525680	4190093	6	0.008890	0.000494	1.007	1.001	0.992
CC70	525893	4189934	6	0.011300	0.000182	1.012	1.002	0.986
CC72	525966	4189846	6	0.017400	0.000281	1.016	0.996	0.988
CC76	525347	4190441	6	0.018400	0.000725	1.008	1.002	0.990
CC79	525421	4190672	6	0.016300	0.000350	1.013	1.000	0.987
CC81b	525382	4190782	6	0.012400	0.000948	1.008	1.000	0.992
CC85	525148	4190704	5	0.016500	0.000878	1.014	0.999	0.987
CC91a	525135	4191719	4	0.016700	0.000789	1.010	1.002	0.988
CC25	528965	4190498	6	0.014700	0.001149	1.018	1.001	0.981
CC29	529259	4190707	6	0.019400	0.000261	1.010	1.003	0.987
CC57a	530084	4192315	5	0.019600	0.001800	1.006	1.001	0.993

AMS data, sills, continued

Sample	UTM E	UTM N	Num.	K <sub>m</sub> (SI)	K <sub>m</sub> 1 $\sigma$ (SI)	K1	K2	K3
	Zone 12N (NAD 83)							
CC63	529926	4192200	6	0.046200	0.003250	1.019	1.000	0.982
CC16	529394	4190071	6	0.031800	0.001560	1.014	0.999	0.987
CC19	529172	4190342	6	0.025500	0.000966	1.014	0.995	0.992
CC23	528978	4190437	6	0.027300	0.000732	1.013	1.001	0.986
CC96	529358	4190108	5	0.032800	0.001130	1.011	0.997	0.991
CC98	529130	4189916	6	0.026100	0.000798	1.017	0.999	0.984
CC104	528693	4190454	6	0.014100	0.000673	1.018	1.001	0.981
CC105	528720	4190396	6	0.016300	0.000187	1.020	0.995	0.984
CC118	526944	4190612	6	0.007970	0.000362	1.006	0.998	0.996
CC120	526968	4190287	6	0.014900	0.000299	1.011	1.000	0.989
CC134	526239	4189815	6	0.011200	0.000187	1.018	1.001	0.982
CC135	526305	4189807	6	0.014800	0.000609	1.014	1.001	0.986
CC137	526397	4189807	6	0.012200	0.000477	1.014	1.004	0.981
CC139	526475	4189792	6	0.016200	0.000854	1.015	1.000	0.986
CC147	527475	4190406	6	0.020100	0.001110	1.013	0.997	0.990
CC160b	526255	4190485	6	0.021400	0.000557	1.015	0.999	0.986
CC163	525859	4190380	6	0.023900	0.000668	1.007	1.001	0.992
CC164	530146	4192118	5	0.019100	0.000652	1.007	1.000	0.993
CC167	529041	4192241	6	0.014600	0.000217	1.031	1.007	0.962
			AVG	0.018671				

AMS data, sills, continued

Sample	K1				K2				K3			
	decl.	incl.	$\alpha_{95}$ max	$\alpha_{95}$ min	decl.	incl.	$\alpha_{95}$ max	$\alpha_{95}$ min	decl.	incl.	$\alpha_{95}$ max	$\alpha_{95}$ min
CC3a	53.1	10.0	3.2	3.0	304.5	61.0	6.2	2.5	148.3	26.9	6.4	1.9
CC7b	287.5	27.2	3.3	1.6	182.9	26.3	3.5	2.7	56.0	50.5	3.1	1.6
CC9a	280.3	52.1	8.9	2.9	59.3	30.4	9.2	6.2	161.9	20.3	6.7	3.0
CC9b	284.0	25.0	10.7	3.9	25.0	22.2	10.5	3.4	151.3	55.5	5.1	2.7
CC36	91.2	2.1	9.1	3.7	350.0	79.3	8.9	4.1	181.6	10.5	5.5	2.1
CC37	286.5	52.1	7.3	3.0	68.2	31.4	7.6	1.6	170.3	19.0	5.2	1.7
CC41	254.2	8.7	3.8	2.1	359.2	59.7	9.4	2.1	159.3	28.8	9.8	1.3
CC43	284.1	65.0	7.2	2.6	26.3	5.6	9.0	6.1	118.8	24.3	8.9	4.3
CC45	10.5	21.3	12.8	9.2	115.5	33.6	12.9	6.7	254.4	48.5	11.2	2.5
CC46a	32.1	0.7	33.9	7.9	288.9	74.4	36.5	27.7	121.2	13.3	37.1	4.6
CC60	67.6	12.7	7.3	1.8	336.4	5.5	7.4	2.0	223.6	76.2	2.8	1.0
CC65	129.9	3.9	13.6	5.4	243.6	80.3	13.1	8.0	39.3	8.9	9.4	8.1
CC67	248.6	35.5	24.3	7.0	129.6	34.1	25.2	9.0	9.9	36.1	14.4	5.5
CC70	114.4	7.9	6.9	3.9	206.0	12.0	14.4	4.0	351.5	75.6	13.8	4.4
CC72	132.7	31.9	4.0	3.6	232.0	14.6	9.5	3.6	343.1	54.1	10.1	2.2
CC76	247.3	12.9	8.0	3.7	155.4	8.0	8.3	2.0	34.3	74.8	3.7	3.0
CC79	123.7	15.8	9.8	3.7	265.3	70.1	8.9	4.0	30.3	11.7	6.0	3.8
CC81b	119.4	19.8	10.8	6.5	347.1	61.9	12.4	4.7	216.6	19.1	8.7	5.5
CC85	263.4	4.3	10.7	1.0	356.6	36.6	10.4	2.7	167.6	53.1	3.3	2.0
CC91a	63.1	10.9	17.9	2.7	154.6	4.2	11.2	2.2	263.1	78.2	19.7	0.8
CC25	311.6	52.5	10.6	5.0	82.4	26.7	18.0	5.0	185.5	24.3	20.6	0.9
CC29	29.4	60.2	16.4	8.5	145.9	14.3	17.6	6.9	242.8	25.5	11.6	6.6
CC57a	266.7	0.0	8.3	3.9	176.7	17.0	8.7	6.2	356.7	73.0	6.9	4.0

AMS data, sills, continued

Sample	K1				K2				K3			
	decl.	incl.	$\alpha_{95}$ max	$\alpha_{95}$ min	decl.	incl.	$\alpha_{95}$ max	$\alpha_{95}$ min	decl.	incl.	$\alpha_{95}$ max	$\alpha_{95}$ min
CC63	174.0	30.9	9.2	3.8	278.1	22.1	7.9	4.4	37.5	50.5	7.9	3.2
CC16	254.0	45.2	7.0	2.9	32.8	36.8	11.3	5.3	140.2	21.8	10.9	4.6
CC19	351.7	40.1	5.7	2.2	260.0	2.1	32.8	2.9	167.5	49.8	32.8	5.2
CC23	148.7	3.6	7.6	3.1	47.9	71.3	6.8	4.9	239.9	18.3	6.0	3.4
CC96	10.9	34.0	11.7	6.6	257.3	30.7	17.3	10.9	136.4	40.8	17.4	4.9
CC98	329.6	67.7	3.1	2.3	102.9	15.7	8.0	1.8	197.3	15.4	7.9	3.0
CC104	111.5	19.3	3.7	2.2	209.5	21.5	2.5	1.0	343.4	60.4	3.5	1.0
CC105	53.9	28.9	6.1	1.8	289.6	45.6	11.2	2.0	162.9	30.4	12.2	3.4
CC118	323.0	37.1	11.2	6.8	84.2	34.4	45.1	7.1	202.0	34.3	45.4	6.7
CC120	51.2	24.7	6.5	2.8	255.9	63.2	6.6	4.3	145.7	9.9	5.1	1.5
CC134	90.7	60.7	6.7	2.2	275.2	29.3	9.9	2.0	184.1	1.9	10.8	2.1
CC135	134.9	40.0	19.0	3.3	31.2	15.8	18.8	5.8	284.4	45.7	6.8	4.9
CC137	240.9	14.3	13.5	3.7	142.3	30.3	13.5	6.1	352.9	55.8	6.7	2.9
CC139	14.9	7.0	8.0	3.2	280.6	31.6	8.5	5.1	116.0	57.4	8.5	6.4
CC147	266.1	10.3	7.4	4.6	1.6	28.0	26.6	4.6	157.8	59.9	27.1	3.1
CC160b	121.6	24.8	1.9	1.2	308.4	65.1	3.8	0.9	212.8	2.6	3.6	1.0
CC163	206.8	31.7	6.2	4.0	111.3	8.8	7.8	1.5	7.9	56.8	5.3	3.8
CC164	279.2	27.5	12.5	2.6	14.1	9.4	17.7	9.5	121.2	60.7	15.9	2.2
CC167	275.8	37.6	2.9	1.0	8.2	3.1	2.9	1.1	102.2	52.2	1.6	1.3

AMS data, sills, continued

Sample	L	F	P <sub>j</sub>	T
CC3a	1.013	1.011	1.024	-0.058
CC7b	1.021	1.029	1.050	0.161
CC9a	1.009	1.017	1.026	0.319
CC9b	1.007	1.013	1.020	0.291
CC36	1.009	1.015	1.025	0.253
CC37	1.010	1.014	1.025	0.176
CC41	1.016	1.011	1.027	-0.176
CC43	1.009	1.006	1.015	-0.195
CC45	1.005	1.008	1.014	0.185
CC46a	1.016	1.008	1.025	-0.367
CC60	1.009	1.013	1.023	0.245
CC65	1.017	1.007	1.024	-0.389
CC67	1.009	1.009	1.018	-0.040
CC70	1.009	1.017	1.027	0.283
CC72	1.020	1.009	1.030	-0.397
CC76	1.006	1.012	1.019	0.320
CC79	1.014	1.013	1.027	-0.002
CC81b	1.008	1.008	1.016	0.004
CC85	1.015	1.012	1.028	-0.148
CC91a	1.008	1.014	1.023	0.235
CC25	1.017	1.023	1.040	0.150
CC29	1.009	1.017	1.027	0.323
CC57a	1.006	1.007	1.013	0.124

AMS data, sills, continued

<b>Sample</b>	<b>L</b>	<b>F</b>	<b>P<sub>j</sub></b>	<b>T</b>
CC63	1.020	1.019	1.039	-0.016
CC16	1.015	1.014	1.029	-0.036
CC19	1.019	1.005	1.025	-0.572
CC23	1.013	1.016	1.029	0.089
CC96	1.015	1.007	1.023	-0.410
CC98	1.018	1.016	1.034	-0.072
CC104	1.017	1.020	1.038	0.086
CC105	1.025	1.012	1.039	-0.363
CC118	1.008	1.003	1.011	-0.437
CC120	1.011	1.011	1.023	0.009
CC134	1.017	1.020	1.038	0.097
CC135	1.015	1.015	1.030	-0.027
CC137	1.011	1.024	1.036	0.369
CC139	1.015	1.015	1.030	-0.032
CC147	1.015	1.009	1.025	-0.090
CC160b	1.016	1.013	1.029	-0.116
CC163	1.007	1.009	1.016	0.147
CC164	1.006	1.008	1.014	0.130
CC167	1.024	1.046	1.072	0.311
AVG	1.013	1.014	1.027	0.009